

Theranostic Gelatin Nanoparticles for Antigen Delivery and Combined Strategies for Transcutaneous Application

Dissertation
zur Erlangung des Grades
des Doktors der Naturwissenschaften
der Naturwissenschaftlich-Technischen Fakultät
der Universität des Saarlandes

Von
Nesma Elsayed Ahmed Ahmed Ibrahim

Saarbrücken
2020

Tag des Kolloquiums:	27.03.2020
Dekan:	Prof. Dr. Guido Kickelbick
Vorsitzender:	Prof. Dr. Andriy Luzhetskyy
Berichterstatter:	Prof. Dr. Marc Schneider Prof. Dr. Thorsten Lehr
Akad. Beisitzer:	Dr. Matthias Engel

Die vorliegende Dissertation entstand unter der Betreuung von

Prof. Dr. Marc Schneider

In der Fachrichtung Biopharmazie und
Pharmazeutische Technologie der Universität des
Saarlandes

*With All the Love, Dedicated to my
Family*

*Mom, Dad and my dear Brother
Mohamed*

Scientific contributions

This thesis encompasses the following publications:

- **N. El-Sayed**, V. Trouillet, A. Clasen, G. Jung, K. Hollemeyer and M. Schneider, "NIR-emitting gold nanoclusters-modified gelatin nanoparticles as a bioimaging agent in tissue", *Advanced Healthcare Materials*, *Advanced Healthcare Materials*, 8(24), 2019,1900993.
- **N. El-Sayed**, L. Vaut and M. Schneider "Customized fast-dissolving microneedles prepared with the aid of 3D printing for nanoparticles delivery", in due publication
- **N. El-Sayed**, E. Korotchenko, R. Weiss and M. Schneider "Functionalized theranostic nanovaccine for dendritic cells targeting and modulation of immune response", in due publication

Table of contents

Summary	5
 Chapter 1: Introduction	
1.1. Skin anatomy	8
1.2. Skin barrier	8
1.3. Skin immunology	10
1.4. Transcutaneous vaccination	11
1.4.1. Microneedles.....	12
1.4.2. Laser microporation.....	14
1.4.3. Electroporation.....	15
1.4.4. Sonophoresis.....	15
1.4.5. Jet injectors.....	16
1.4.6. Transdermal patches.....	16
1.5. Vaccine nanocarriers	16
1.5.1. Types of antigen nanocarriers.....	17
1.5.1.1. Liposomes.....	17
1.5.1.2. Polymeric nanoparticles	17
1.5.1.3. Inorganic nanoparticles.....	19
1.5.2. Advances in nanoparticles formulations for antigen delivery	19
1.5.2.1. Antigen encapsulation vs antigen display.....	19
1.5.2.2. Adjuvants delivery.....	20
1.5.2.3. Delivery to lymph nodes.....	20
1.5.2.4. Interaction with dendritic cells.....	21
1.6. Imaging of nanoparticles in skin	24
1.6.1. Different imaging agents for nanoparticles tracking using CLSM.....	25
1.6.1.1. Dyes.....	25
1.6.1.2. Quantum dots.....	25
1.6.1.3. Gold nanoclusters.....	26
1.7. Disclosure	28
1.8. References	28

Chapter 2: Research Objectives	37
---	----

Chapter 3: NIR-Emitting Gold Nanoclusters-Modified Gelatin Nanoparticles as a Bioimaging Agent in Tissue

3.1. Abstract	40
3.2. Introduction	41
3.3. Materials and methods	42
3.3.1. Materials.....	42
3.3.2. Synthesis of gelatin-stabilized AuNCs.	43
3.3.3. Synthesis of gelatin-stabilized AuNCs modified by glutathione.....	43
3.3.4. Gelatin structure integrity.....	43
3.3.5. Synthesis of Ag-modified AuNCs stabilized by gelatin and glutathione.....	44
3.3.6. Characterization of selected AuNCs formulations.....	44
3.3.7. XPS analysis	45
3.3.8. Preparation and characterization of AuNCs-modified GNPs.....	46
3.3.9. Cell culture.....	46
3.3.10. Bioimaging of GNPs with skin tissue.....	47
3.4. Results and Discussion	48
3.4.1. Synthesis of gelatin-stabilized AuNCs.....	48
3.4.2. Structure integrity of gelatin during AuNCs formation.....	51
3.4.3. Fluorescence enhancement.....	53
3.4.4. Structure - fluorescence stability relationship.....	55
3.4.5. Formation of protein nanoparticles using AuNCs-modified gelatin.....	60
3.4.6. Tissue bioimaging based on linear unmixing.....	62
3.5. Conclusion	65
3.6. References	66

Chapter 4. Customized Fast-Separable Microneedles Prepared with the Aid of 3D Printing for Nanoparticle Delivery

4.1. Abstract	72
4.2. Introduction	73
4.3. Materials and Methods	74
4.3.1. Materials.....	74
4.3.2. Design and fabrication of microneedles molds	75

4.3.2.1.	Design of positive microneedles mold master	75
4.3.2.2.	3D printing of positive microneedles mold master	75
4.3.2.3.	Molding of negative microneedles mold	76
4.3.3.	Preparation of nanoclusters loaded gelatin nanoparticles (NCs-GNPs)	76
4.3.4.	Molding of nanoparticles loaded-microneedles patches.....	76
4.3.5.	Characterization of NCs-GNPs-loaded MNs	77
4.3.5.1.	Fracture force.....	77
4.3.5.2.	Penetration force	77
4.3.5.3.	Confocal laser scanning microscopy (CLSM)	77
4.3.6.	Microneedles patch modification and skin penetration studies	78
4.4.	Results and Discussion.....	78
4.4.1.	Design and development of MNs molds.....	78
4.4.2.	Manufacturing of MNs by molding and NPs loading.....	80
4.4.3.	Mechanical properties of MNs.....	82
4.4.4.	Spectral imaging	84
4.4.5.	MNs modification and skin penetration studies.....	86
4.5.	Conclusion.....	88
4.6.	References.....	89

Chapter 5. Functionalized Theranostic Nanovaccine for Targeting Dendritic cells and Modulation of Immune Response

5.1.	Abstract.....	93
5.2.	Introduction.....	94
5.3.	Materials and Methods.....	95
5.3.1.	Materials.....	95
5.3.2.	Preparation of fluorescent ovalbumin loaded-gelatin nanoparticles.....	96
5.3.2.1.	Preparation of gold-silver nanoclusters-labelled gelatin.....	96
5.3.2.2.	Preparation of gelatin nanoparticles.....	96
5.3.2.3.	Ovalbumin surface loading.....	97
5.3.2.4.	Ovalbumin encapsulation and surface functionalization	97
5.3.3.	Nanoparticles characterization.....	97
5.3.4.	Entrapment efficiency	98
5.3.5.	Release studies.....	98
5.3.6.	Cellular interaction with bone marrow-derived dendritic cells (BMDCs)	98

5.3.6.1. Generation of BMDCs.....	98
5.3.6.2. Cell viability, nanoparticles uptake and cell activation	99
5.3.6.3. Confocal laser scanning microscopy (CLSM)	99
5.3.7. Co-culture with naïve T cells	100
5.3.8. Deposition studies in skin using P.L.E.A.S.E (Precise Lasers Epidermal System) device	101
5.4. Results and Discussion	101
5.4.1. Design, preparation and characterization of ovalbumin-loaded nanoparticles	101
5.4.2. Ovalbumin release.....	105
5.4.3. Interaction of nanoparticles with BMDCs.....	106
5.4.4. Effect of nanoparticles on naïve T cells proliferation.....	109
5.4.5. Transcutaneous delivery of nanoparticles using P.L.E.A.S.E technology.....	111
5.5. Conclusion	112
5.6. References	113
Chapter 6. Summary, Conclusion and Outlook	117
Annex	120
Curriculum Vitae	137
Acknowledgements	142

Summary

Transcutaneous application of vaccines is a promising strategy to enhance the effectiveness of vaccination using a reachable route of administration. Additionally, replacing the conventional needles with skin mechanical penetration techniques as microneedles or skin laser microporation will offer great advantages. These transcutaneous delivery techniques are pain-free and will help to avoid the hazards of needles. For the delivery of antigens, nanocarriers are so promising to enhance and modulate their immune response. The nanocarriers offer merits such as antigen protection from degradation, and controlling the release rate of the antigen. Additionally, due to the particulate nature of the nanocarriers, they can potentially display the antigen in a way that better mimics pathogens. For this aim, ovalbumin as a model antigen has been delivered using functionalized theranostic gelatin nanoparticles to bone marrow-derived dendritic cells (BMDCs). The nanoparticles were rendered fluorescent by using a novel imaging agent (gold and silver alloy nanoclusters) that emits near-infrared light. This was beneficial to study the nanoparticles uptake by BMDCs and also to image the nanoparticles within the skin tissue. Finally, the developed theranostic nanocarriers induced the maturation of the BMDCs and enhanced the proliferation of both helper T cells (CD4+) and cytotoxic T cells (CD8+). This indicates the potential efficacy of the delivery system for vaccination either against allergy or viruses and tumors.

Kurzzusammenfassung

Die transkutane Applikation von Impfstoffen ist eine vielversprechende Strategie, um die Wirksamkeit der Impfung auf einem gut erreichbaren Verabreichungsweg zu erhöhen. Zusätzlich bietet der Ersatz von konventionellen Nadeln durch mechanische Penetrationstechniken der Haut, wie Mikronadeln oder Hautlaser-Mikroporation, große Vorteile. Diese transkutane Verabreichungstechnik ist schmerzfrei und wird dazu beitragen, die Patientencompliance zu erhöhen. Für die Darreichung von Antigenen stellen Nanocarrier eine vielversprechende Arzneiform dar, da sie die Immunantwort verstärken und modulieren können. Die Nanocarrier bieten Vorzüge wie den Schutz des Antigens vor Abbau und die Kontrolle der Freisetzungsrates des Antigens. Darüber hinaus können die Nanocarrier aufgrund ihrer partikulären Beschaffenheit das Antigen potenziell so präsentieren, wie es Krankheitserreger tun. Zu diesem Zweck wurde Ovalbumin als Modellantigen unter Verwendung funktionalisierter theranostischer Gelatine-Nanopartikel in dendritische Zellen aus Mäuseknochenmark eingebracht. Die Nanopartikel können mit neuartigen Fluoreszenzsonden (Nanocluster aus Gold- mit Silber) markiert werden, die rotes Licht im nahen Infrarotbereich emittieren. Dies war vorteilhaft, um die Aufnahme der Nanopartikel durch die dendritischen Zellen zu untersuchen und auch um die Nanopartikel im Hautgewebe abzubilden. Schließlich induzierten die entwickelten theranostischen Nanocarrier die Reifung der dendritischen Knochenmarkszellen und verstärkten die Proliferation von T-Helferzellen als auch der zytotoxischen T-Zellen. Dies deutet auf die potenzielle Wirksamkeit der Formulierung für die Impfung entweder gegen Allergien oder Viren und Tumore hin.

Chapter 1. Introduction

1. Introduction

Transcutaneous delivery of drugs and macromolecules is an attractive route of administration, due to the accessibility of skin, being the largest organ (weighing 5-6 kg and covering an average area of 1.7 m²) (1) and the outermost layer of the body. Skin functions as a barrier to protect the body from exterior radiation or microorganisms and from internal water loss that can lead to dehydration. Besides being a mechanical barrier, skin has immunological function by acting as the first line defense when antigens or microorganisms invade the body through skin. It is rich in antigen presenting cells (APCs) in both the epidermis and dermis, which have a role in both innate and adaptive immunity. Making use of such function renders skin an attractive site for immunization (2).

1.2. Skin anatomy

Skin composes of three main layers (Figure 1): epidermis (the outer most layer), dermis, and subcutaneous fat tissue. The epidermis is the outer most layer of skin of 50 to 150 μm thickness. Stratum corneum represents the surface upper layer of the epidermis with 15–20 μm thickness. It is responsible for the barrier function of skin with a rigid bricks and mortar structure. They consist of keratinized epithelial cells (coenocytes, bricks) connected by desmosomes and embedded in intercellular lipids, mainly ceramides, cholesterol and saturated long chain fatty acids (3), of organized lamellar structure (mortar). Laying beneath is the viable epidermis, consisting of mainly keratinocytes and other cell classes as melanocytes, Merkel cells and Langerhans cells. Below the epidermis, locates the dermis that consist of fibroblasts, mast cells, and dermal dendritic cells. This skin layer contains blood vessels, lymph vessels and nerves. It is responsible then for exchanging fluids with blood and skin and skin sensation as well. Deeper in skin, lays the subcutaneous tissue that consists of adipocytes to act as a thermal barrier. Skin also has appendages such as sweat glands, pilosebaceous units, and hair follicles that originate from the dermis or the subcutaneous tissue toward skin surface (2).

1.3. Skin barrier

Stratum corneum shapes the skin barrier against materials absorption. It restricts the

diffusion of molecules of molecular weight higher than 500 kDa (5). Additionally, the material's hydrophobicity matters as partition coefficients ($\log P$) between 1 and 3 represent the optimal for skin absorption (6). Pathways for skin absorption are through skin SC; intercellular or intracellular pathway or through skin appendages (transfollicular pathway) (4). The intercellular pathway is the main pathway, where molecules diffuse through the spaces between crystalline lipid lamellae and their adjacent cells' outer membrane (7). On the other hand, the intercellular pathway is unlikely of importance for materials diffusion through the rigid corneocytes, which are dead cells filled with keratin and surrounded by an impermeable cornified envelop (2, 6). Transfollicular pathway has gained interest recently, for topical or transdermal delivery of nanoparticles. The hair movement is claimed to pump the nanoparticles into the hair follicle (8), which can act as a depot for nanoparticles to release the drug for the treatment of skin diseases. However, the efficiency of the follicular delivery is highly affected by the particle size. On the other hand, the follicular orifices represent only 0.1% of the human skin surface area (4, 6).

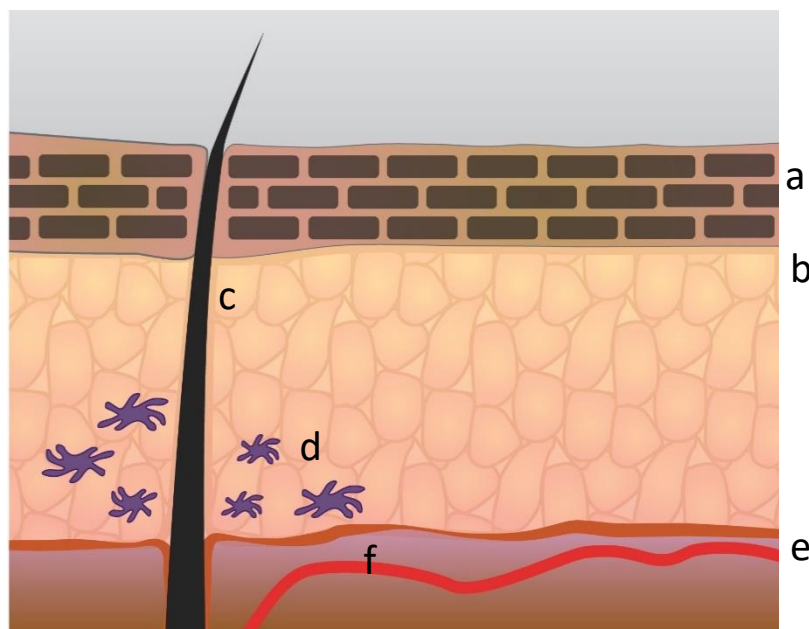


Figure 1. Skin structure showing different skin layers and their structures, a) stratum corneum (uppermost layer), b) epidermis which composes mainly of keratinocytes, c) hair follicle, d) Langerhans cells, e) dermis and f) blood vessel. The figure is adapted from El-Sayed *et al* (4).

1.4. Skin immunology

Skin plays an important role in both innate and adaptive immunity. Innate immunity, known as natural immunity, is naturally present at birth. It is the first line defence in form of an immediate non-specific immune response, when antigen is introduced to the body as a 'danger signal', using defensive tools such as fever, the complement system, phagocytic and natural killer cells, naturally occurring antibodies and antimicrobial peptides. Adaptive or acquired immunity is a learned, specific immune response to an antigen due prior-sensitization, with long term immunological memory (9). When skin barrier is disrupted and keratinocytes, which represents 90–95% of the total epidermis cells (10), find a danger signal, they start an innate immune response by releasing cytokines, chemokines and antimicrobial peptides (11). They also release cytokines, granulocyte-macrophage colony-stimulating factor (GM-CSF) and tumor necrosis factor- α (TNF- α), to induce the maturation and migration of dendritic cells (10).

Dendritic cells are sentinels of immunity and tolerance. They are antigen presenting cells (APC). They are responsible and capable of taking antigens from the periphery to lymphoid tissues (12). They also transfer the signals from innate to adaptive immune system by regulating T-cell differentiation. There are two types of dendritic cells present in skin: a) Langerhans cells which are located in the epidermis. They are much fewer than keratinocytes (only 2%), but they are large in size with many appendages that connect to form a network and b) dermal dendritic cells (interstitial DCs), which locate in dermis (13). Immature dendritic cells always scan the surroundings for foreign bodies (14) (Figure 2). They recognize pathogens and antigens through pattern recognition receptors (PRRs) which are classified into 2 groups (15): a) endocytic PRRs: they can phagocytose microorganisms and bind to carbohydrates. They include mannose receptor (MR), glucan receptor and scavenger receptor, b) signaling PRRs: they include membrane bound toll-like receptors (TLR) (including receptor kinases and C-type lectin receptors) and cytoplasmic NOD-like receptors. The recognized antigen cause maturation of dendritic cells and their migration to lymph nodes. The DCs process the phago- or endocytosed antigens into small fragments during their maturation to display them on their surfaces by major histocompatibility (MHC) molecules to present them to T cells (Figure 2). Additionally, they upregulate surface

receptors that help for activating T-cells as CD80, CD86 and CD40. They present the antigens to helper T-cells (CD4+) or cytotoxic T-cells (CD8+) to activate them to start a cascade of immune responses (16).

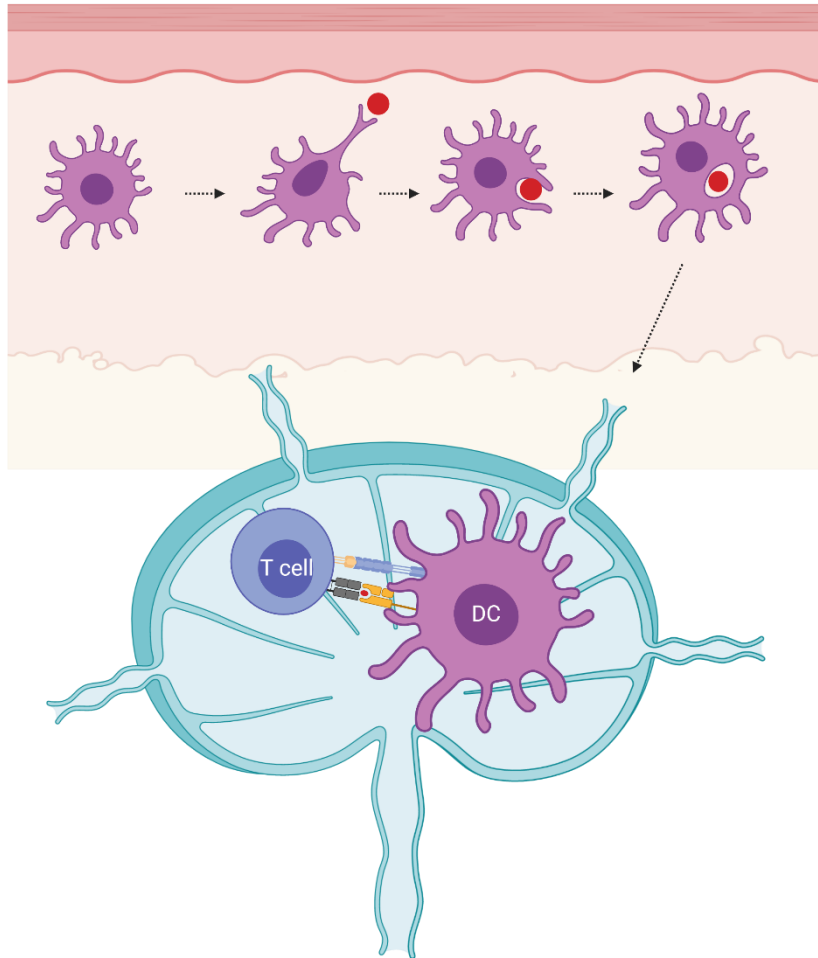


Figure 2. Uptake and processing of nanoparticles by dendritic cells in skin dermis and dendritic cells migration to lymph nodes to present the processed antigen to T-lymphocytes.

1.5. Transcutaneous vaccination

Vaccination is developing an immunological memory of the adaptive immune system against a specific disease. There are different types of vaccines (17): a) live-attenuated: contains attenuated live viruses that cannot cause disease, b) inactivated or killed: contains inactivated pathogens, c) toxoid: contains weakened toxins taken from pathogens, d) subunit: contains part of pathogen's antigen, e) conjugated: contains polysaccharides from the bacterial outer membrane, f) peptide: contains

synthetic peptide and g) DNA: contains genetic material from the pathogen. Conventional vaccines are administered usually by injection. However, this method is painful and needles and syringes can cause many problems including the possibility for injury or disease transmittance. They also need trained personnel and special storage and transport. Consequently, the development of needle-free painless methods is a prerequisite. The transcutaneous route is gaining high interest due to the richness of skin in immune cells and easy accessibility to skin. However, methods for skin penetration and overcoming the SC barriers are essentially required (18) (Figure 3).

1.5.1. Microneedles

Microneedle technologies are gaining high interest for transcutaneous delivery of medical cargos as pain-free and easy-to use products that may waive the use of needles in the future. They are designed as patches with arrays of micron-sized projections (50–900 μm long) ‘microneedles’ which can be inserted into skin to overcome the SC barrier and reach the viable tissue. Microneedles are required to be with minimum length and sufficient mechanical strength to be able to overcome the elastic deformation of skin and pierce it (19). There are different types of microneedles: solid, hollow, dissolvable and swellable.

a) Solid microneedles: Among the materials that were first investigated for manufacturing solid microneedles were silicon, titanium, and stainless steel. They are either in form of patch, punch or roller such as the dermaroller, which is commonly used for cosmetics purposes (19). They rely on ‘poke and patch’ approach, where the microneedles poke the skin to create micro-channels followed by application of drug loaded-patch to allow for drug diffusion into skin (20). Another approach is soaking the microneedles in drug solution prior to insertion into skin (19). Modification of the solid microneedles manufacturing has been introduced by coating their surface with a layer containing the drug to be known as ‘coated microneedles’ (21). Regarding the safety, microneedles made of silicone are not preferable due to the probability of breaking of the microneedles’ tips in skin that may cause problems (22). On the other hand, it is important for the micro-channels

formed in skin to close shortly after removal of the microneedles to avoid the permeation of undesirable materials or pathogens (23).

- b) Hollow microneedles: They are fabricated with hollow channels inside to allow drug transfer (up to 200 μ l) into skin from a reservoir. In other words, they resemble in design the hypodermic needles. The fabrication of the hollow interior of the microneedles, makes the process more complex. Additionally, the absence of the internal support compared to solid microneedles, can result in their fracture if not inserted properly, especially for the microneedles with high aspect ratio (19). They are used for the delivery of biomacromolecules including proteins and oligonucleotides (24). They can deliver drugs with large doses, but the flow rate needs to be adjusted to keep the flow to avoid accumulation of drugs in the space inside the microneedles. Also the flow rate can be accelerated if a rapid bolus injection is necessary (25). On the other hand, the microneedles with such hollow designs were applied for interstitial fluid sampling for monitoring or diagnosis (26).
- c) Dissolving microneedles: This type of microneedles is gaining growing interest (27-34). They are prepared out of biodegradable polymers matrices which encapsulate the drug to fulfill the strategy of “poke and release”. After the insertion in skin, the microneedles stay in skin to dissolve to release the drug. So, it is a single step application, which enhance patient compliance (24). Microneedles patches can be applied by patients themselves, either manual, by thumb pressing, or by using an applicator. Another important advantage is that this type of microneedles don't leave environmental waste behind, which is a significant problem when it comes to the disposal of hypodermic needles (35). Micromolding is the main fabrication method adopted in different labs. The microneedles are formed by pouring the polymer/drug mixture into a mold which is usually made out of polydimethylsiloxane (PDMS). The drying of the microneedles is usually done under ambient conditions, which is important for delivery of thermolabile biomacromolecules as protein and peptides (24).
- d) Hydrogel-forming (swellable) microneedles: They compose out of super-swelling polymers that absorb large amounts of interstitial fluid when inserted into skin, so they expand and become porous allowing for drug release (36). Additionally, they can be used for biological fluids sampling (37).

1.5.2. Laser microporation

Skin microporation using laser or fractional laser ablation is a recently-introduced approach for transcutaneous delivery of antigens. A pulsed infra-red laser is used for controlled ablation of skin. The water content of tissue highly absorbs the energy of the near infra-red light and evaporates rapidly. This generates pressure that disrupts the tissue and results in expelling of the cellular content from the site of laser application (38). Increasing the energy of applied laser light (fluence), pulse duration and frequency would result in higher ablation efficiency. However, long pulses and high repetition rate would result in heat generation and thermal injury. This can be avoided by using high energy pulses with short duration (lower than the water relaxation time), so transfer of heat to surrounding tissue can be neglected (39).

Different lasers have been utilized for skin microporation such as Nd:YAG lasers [48] and CO₂ lasers. Nd:YAG laser has a wavelength of 2940 nm, which coincide with the absorption peak of water. It can induce 'cold ablation' i.e. with negligible heat transfer to the surroundings when compared to CO₂ lasers (40). Novel devices are in the market now, in which the laser beam splits into an array of smaller microbeams that disrupt the upper layer of skin and induce pore-formation only at the site of exposure to the laser light leaving the tissue in between intact. This results in an array of pores in skin where the density of pores per unit area can be controlled. This is an advantage for decreasing the ablated area of skin and allowing for faster healing (40). Fractional laser ablation is an attractive method for transcutaneous vaccination. The applied laser can enhance the immune response against the applied antigen. The laser creates pores in upper layer of skin (epidermis or epidermis-dermis junction). Additionally, it creates a pro-inflammatory environment, where immune cells in skin including dendritic cells get triggered, uptake the applied antigen and become activated to transfer the antigen to secondary lymphoid organs, to activate T-cells and induce immune response. In contrast, intradermal immunization delivers antigens deep in skin, where they can be drained passively to secondary lymphoid organs as soluble antigens (41).

1.5.3. Electroporation

Electroporation method involves the application of electric pulses of short duration and high voltage (75–100 V) to skin surface. The applied current creates transient pores in the lipid bilayer membrane of cells, so can enhance the permeability of molecules (42, 43). The technology has been reported for successful delivery of antigens (44) and DNA vaccines (45). Additionally, the electric pulses themselves have an adjuvant effect on the immune system by recruiting and triggering the immune cells in skin (45, 46). Although the technique was developed for use in medical institutions, as a power supply equipment is required, new series of hand-held cordless electroporation device became available (47).

1.5.4. Sonophoresis

In sonophoresis, low-frequency ultrasound (20 to 100 kHz) (48) is applied to skin surface. The ultrasound cause cavitation, which results in formation of gas bubbles in the tissue. This loosens the integrity of the SC and thus enhance the permeability. Two types of cavitation can be generated; either transient cavitation, which is a rapid enlargement and collapse of the bubbles, or stable cavitation, which is slow oscillatory motion of the bubbles (49). Additional physical adjuvant effect of the ultrasound on recruiting the immune system in skin was also reported (50).

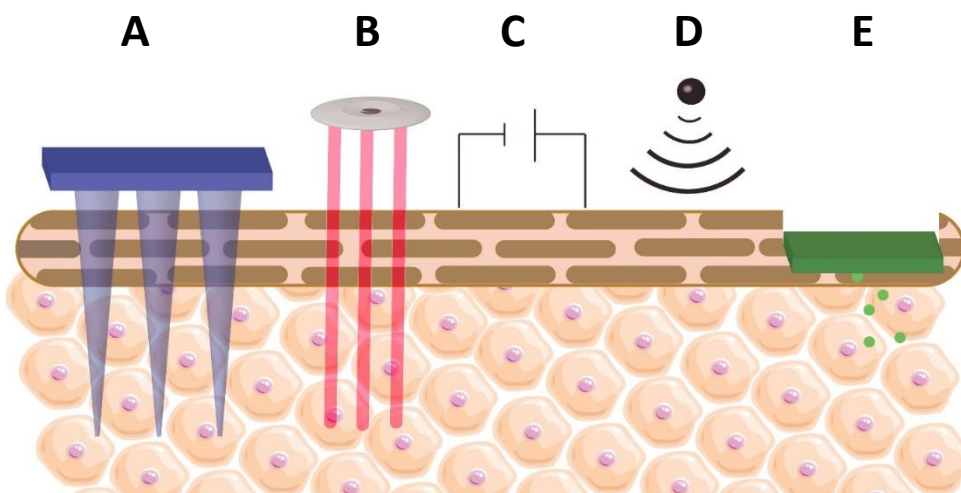


Figure 4. Different methods for transcutaneous delivery of macromolecules and nanoparticles, A) microneedles, B) skin microporation using pulsed infrared laser, C) electroporation, D) sonophoresis and E) transdermal patch and tape-stripping.

1.5.5. Jet injectors

Jet injectors are needle-free devices that use high-velocity jets (100 to 200 m/s) to deliver materials into skin or even to the muscles. They consist of a power source which is compressed gas or a spring, a piston, a compartment filled with the drug solution and a small nozzle that is 150-300 μm in size (51). By actuation, the device releases the drug solution through an orifice with high velocity to hit the skin creating a hole to deliver the drug through skin. The whole process of skin penetration takes just microseconds. The devices can be in form of multi- or single-use jet injectors depending on the number of injections the device contains (47).

1.5.6. Transdermal patches

Conventional transdermal patches have been well-known for their occlusive effect to transfer drugs into skin. SC hydration decreases its barrier integrity and increases the permeability of foreign materials into skin (52). Transdermal patches have been used for delivery of molecules such as nicotine, estrogen and lidocaine, which are all known for their hydrophobicity (53). Additionally, chemical enhancers can be used in the formulation of the patches, which can increase skin permeability to small molecules, however with limited improvement when it comes to biomacromolecules (52). So, combination of patches with other physical penetration methods is a prerequisite for transcutaneous delivery of antigens such as ultrasound or electric pulses (53). Tape-stripping prior to patch application showed to be effective for antigen delivery and triggering the immune system as shown by Etchart *et al* (54).

1.6. Vaccine nanocarriers

Using nanoparticles for vaccine delivery offers different advantages over the administration of soluble antigens. The particles have the ability to induce strong humoral and cellular immune response to antigens due to their particulate nature. Additionally, they are safer if compared to live attenuated viral vaccines for example. Modulation of the nanoparticles physicochemical properties, size, shape and the way of antigen encapsulation alongside with the exclusive property to control the rate on antigen release can make a big difference to the immune response toward antigens.

Different types of nanoparticles have been tested for antigen delivery as will be discussed.

1.6.1. Types of antigen nanocarriers

1.6.1.1. Liposomes

Liposomes are spherical vesicles formed of a lipid bilayer that self-assembles around an inner aqueous core. They are composed of biodegradable non-toxic phospholipids and cholesterol. They have either unilamellar or multilamellar structure with several concentric lipid shells around the aqueous core, where the antigens can be loaded within (55). The liposomes deliver antigens to cells by fusion with the cellular membrane (56). They resemble enveloped viruses that are surrounded by parts of the cellular membrane of the infected cells. They can perform as adjuvants that stimulate the innate immunity (57). Additionally, liposomes may contain viral envelope glycoproteins to form virosomes (58).

1.6.1.2. Polymeric nanoparticles

Polymeric nanoparticles have been widely applied for antigen delivery due to different reasons including the biodegradability, biocompatibility, ease of preparation and possibility to manipulate their surface properties. The applied polymers are either synthetic (e.g. poly (lactic-co-glycolic acid), PLGA) or natural such as polysaccharides (e.g. chitosan and alginate) and polypeptides/proteins (e.g. gelatin). PLGA nanoparticles have been designed for the delivery of different antigens including hepatitis B virus antigen (59), tetanus toxoid (60) and ovalbumin (61) and oligonucleotide delivery as well (60). PLGA is a well-tolerated biodegradable polymer. It degrades slowly by bulk erosion mechanism which is helpful for controlling the release rate of antigen. The degradation rate is faster with higher degree of the polymer hydrophilicity, which is controlled by the ratio of the glycolic and lactic acid (62).

On the other hand, among the natural polymers that have been gained interest for antigen delivery is gelatin. Gelatin is biocompatible and of low immunogenicity. It is an attractive polymer for antigen delivery due to its hydrophilic nature (63). It is a denatured protein that results from partial alkaline or acidic hydrolysis of collagen. This

results in two different types of gelatin: type A and B, respectively. They have different isoelectric points (IEP): 7-9 for type A and 4-5 for type B. The latter show better potential for drug and DNA delivery (64). Due to its protein nature, gelatin possesses many functional groups which give the opportunity for nanoparticles surface modification by ligands for example for targeted antigen delivery (63). The preparation and loading of the antigens can be done under non-harsh conditions which is necessary for preserving the conformation and the activity of antigens. They can be loaded by adding the antigens before the preparation of the nanoparticles or even after the preparation by soaking the nanoparticles in the antigen solution or by chemical interaction of the antigen to the nanoparticles surface (64). This different techniques can offer different functions such as controlling the release rate, antigens protection and antigen display mimicking the natural presentation by pathogens. Gelatin nanoparticles have been investigated for the delivery of antigens such as tetanus toxoid (65) and ovalbumin (66) and DNA as hepatitis C virus recombinant NS2 gene (67).

The prepared nanoparticles are required to be cross-linked to keep the nanoparticles structure and prevent their solubility in water. Among the most commonly used cross-linking agents is glutaraldehyde which is a non-zero length cross-linker that links both the amine and carboxylic groups of the amino acids (68). However, glutaraldehyde is reported for its cytotoxicity (69). On the other hand, carbodiimide cross-linkers seem to be promising alternatives to avoid the cytotoxicity of glutaraldehyde as they are zero-length cross linkers, such as 1-ethyl-3-(3-dimethylaminopropyl) carbodiimide (EDC) (70) and N,N'-Diisopropylcarbodiimide (DIC) (71). Different simple techniques have been adapted for gelatin nanoparticles' preparation such as:

- a) Nanoprecipitation: In this technique, aqueous solution of gelatin and the drug is added to an antisolvent (which is miscible with water such as acetone or ethanol) containing a stabilizer (such as poloxamer). Solvent displacement results in nanoparticles formation that will be further cross-linked (72).
- b) Two-step desolvation: The technique depends on the introduction of gelatin solution to an antisolvent for gelatin precipitation. This is done over two steps: the first precipitation is to precipitate the high molecular weight gelatin peptides and to

get rid of the low molecular weight gelatin chains that can cause further irreversible aggregation of the nanoparticles. The high molecular gelatin is then dissolved and the drug is added to be further precipitated as nanoparticles. The procedure results in formation of nanoparticles with homogenous particle size (70).

- c) Simple coacervation: This can be achieved by adding salt or alcohol to charged macromolecules that results into liquid-liquid phase separation. Two immiscible phases, which are in equilibrium, are formed then: a dense coacervate phase and a diluted one (73).
- d) Microemulsion: W/O microemulsion is formed when gelatin aqueous solution is added to an organic solvent (immiscible with water) containing surfactant, using high homogenization speed, followed by nanoparticles cross-linking and solvent evaporation (74).

1.6.1.3. Inorganic nanoparticles

Some biocompatible inorganic nanoparticles have been investigated for antigen delivery. These include gold nanoparticles, mesoporous silica and carbon nanotubes. They can be synthesized with a precisely controlled size and shape and their surface can be easily modified (55). For example, antigens have been coupled to the surface of gold nanoparticles to induce an immune response (75). Gold nanoparticles with different shapes can induce different immune responses. In an immunological study done by Niikura *et al.*, gold nanospheres and nanocubes induced tumor necrosis factor- α (TNF- α), IL-6, IL-12 and granulocyte macrophage colony-stimulating factor (GM-CSF), while gold nanorods induced interleukin-1 β and IL-18 through an inflammasome-dependent mechanism (76).

1.6.2. Advances in nanoparticles formulations for antigen delivery

1.6.2.1. Antigen encapsulation vs antigen display

Antigen delivery using nanoparticles has proven to be more effective than the administration of soluble antigen. Nanoparticles can act as a delivery system for antigens either by delivery of the antigen and being co-digested inside the cell or being a transient delivery system by protecting the antigen to release it at the target location (77). Different methods for loading the nanoparticles with antigens have been studied

to provide certain advantages to the delivery system (Figure 4A). Encapsulation of the antigen within the nanoparticles' matrix allows for antigen protection. On the other hand, association of the antigen on the surface of the nanoparticles allows for multiple antigen display which mimic the natural display of antigens on the pathogen and can enhance the immune response. Surface loading can be achieved by: a) chemical conjugation to functional groups on the surface of the nanoparticles, b) electrostatic interaction between oppositely charged antigens and the nanoparticles and c) physical adsorption as in case of inorganic nanoparticles where antigens attach to the surface of gold nanoparticles, by weak interaction forces forming a protein corona, preventing the aggregation of the nanoparticles (57).

1.6.2.2. Adjuvants delivery

In addition to using the nanoparticles for the delivery of antigens, they have been used for adjuvants delivery for enhanced immune response. Different strategies have been followed for delivering adjuvants by nanoparticles. Co-delivery of both the antigen and the adjuvant has been studied by association to the surface of the nanoparticles, so both of them are exposed to the immune cells (Figure 4A). Liu *et al* have functionalized PLGA nanoparticles with both hepatitis B surface antigen and TLR9 agonist unmethylated cytosine-guanine (CpG) adjuvant (78). Another method for adjuvant co-delivery with antigens is loading them separately using the same or different types of nanocarriers. Hanson *et al* have co-delivered low immunogenic HIV antigen liposomal formulation, with cdGMP adjuvant loaded in PEGylated lipid nanoparticles (79) (Figure 4A).

1.6.2.3. Delivery to lymph nodes

Particle size of the nanoparticles is a determinant for their cellular interaction and their distribution after administration. Nanoparticles strongly help to target the antigens to lymph nodes in comparison to soluble antigens. Particles with size 10-100 nm are drained directly to lymph nodes where they can be taken up by resident immune cells as macrophage and dendritic cells (80, 81) (Figure 4B). On the other hand, particles larger than 100 nm stay at the administration site to be taken up and processed by local antigen presenting cells (APCs) (e.g. dendritic cells) that migrate to lymph nodes

to present the processed antigen fragment to T cells (81, 82) (Figure 4B).

1.6.2.4. Interaction with dendritic cells

Different properties of nanoparticles modify their interaction with cells including size, shape and charge. Nanoparticles with comparable size to pathogens can be recognized by APCs easily. Particles of size 20-200 nm which mimic the viruses' size are preferably taken up by dendritic cells, while larger particles of 0.5-5 μm are taken up by macrophages (83). Particles' shape is important for detecting how they interact with cells. For example, spherical particles showed higher phagocytosis by macrophage compared to the negligible uptake of worm-like particles with aspect ratio > 20 (84). Considering the surface charge, positively charged particles have higher ability to be taken up by APC due to their interaction with the negatively charged cell membrane (85) (Figure 4C).

On the other hand, targeting dendritic cells is a promising strategy for activating the dendritic cells and increasing the efficiency of vaccination (Figure 4C). Dendritic cells can recognize antigens through different types of receptors as C-type lectin receptors (CLRs) and Toll-like receptors (TLRs) (86). Functionalization of nanoparticles by suitable ligands to target a specific receptor can enhance antigen capture by dendritic cells through receptor-mediated endocytosis. For example, DCs have a specific intercellular adhesion molecule-3-grabbing non-integrin (DC-SIGN) which is a type of DCs lectin that recognizes mannose clusters exposed by many pathogens. This approach has been utilized for targeting functionalized gold nanoparticles to dendritic cells through carbohydrate-lectin interactions, so the particles can be internalized to the cytosol (87).

After DCs recognize and capture the antigen, they process it into small fragments and transfer them to MHC molecules to be exposed on the cellular surface and presented to T cells (Figure 5). Exogenous antigens are loaded into MHC II molecules to be presented to CD4+ cells that become activated and differentiate into T helper cells (Th1, Th2, Th1) and Tregs that release cytokines to activate other immune cells such as B cells. On the other hand, endogenous antigens from virus-infected cells or cancer

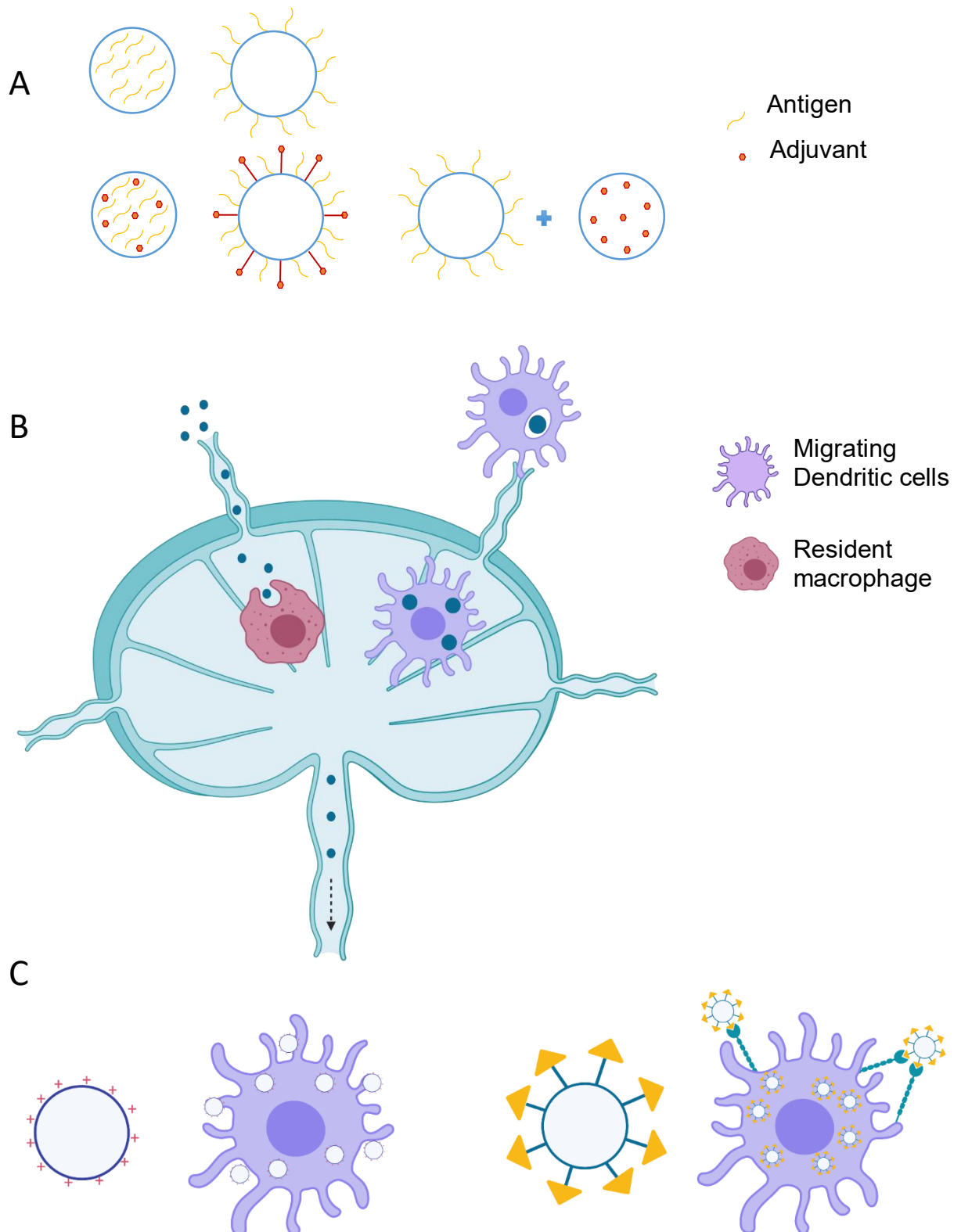


Figure 4. Advances in nanoparticles formulations for antigen delivery and effective vaccination, a) different ways for antigen delivery by encapsulation or surface display of the antigen alone or in combination with an adjuvant, b) delivery of the antigen to lymph nodes

either by size targeting (> 100 nm) to be taken up by resident macrophages or by migratory dendritic cells for nanoparticles < 100 nm and c) targeting of nanoparticles to dendritic cells either by having a positive surface charge or being functionalized by a targeting moiety.

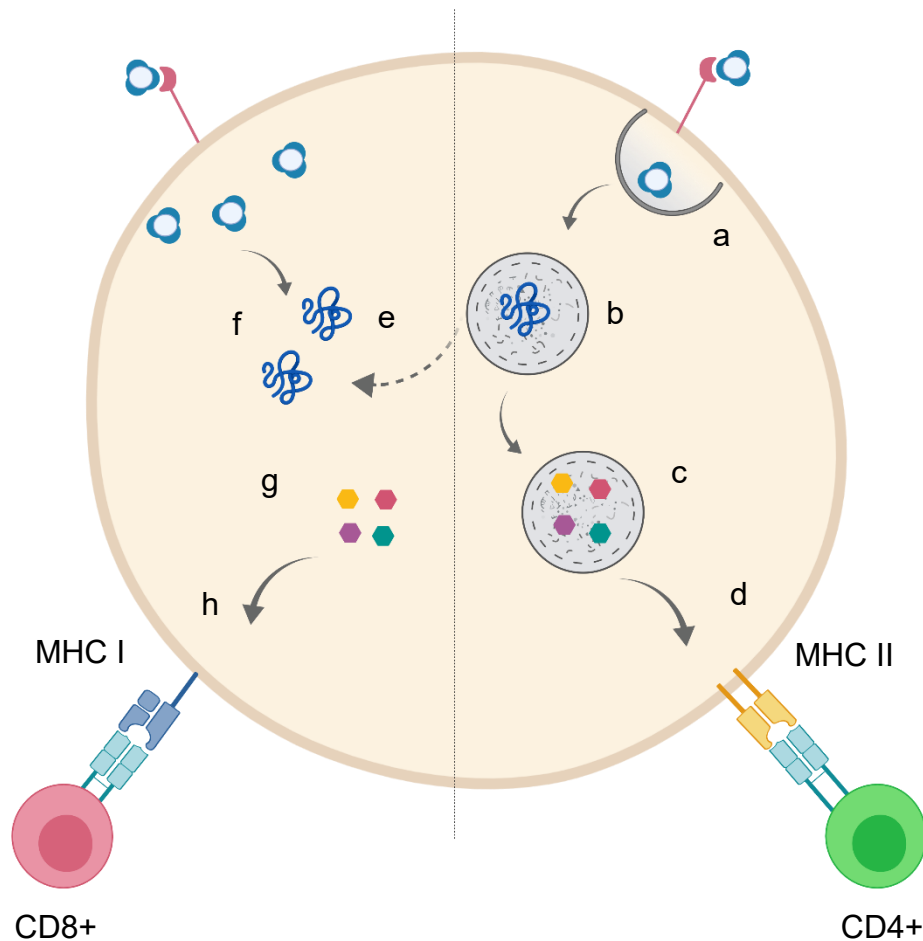


Figure 5. Antigen processing and presentation by dendritic cells through two different pathways: 1) For exogenous antigens: a) endocytosis, b) endosome formation, c) enzymatic fragmentation of the antigen and d) presentation by MHC II to CD4+. e) cross-presentation in case of endosomal escape of the antigen to the cytosol to be processed as an endogenous antigen. 2) For endogenous antigens, f) cytosolic antigens, g) antigen processing by proteasomes and h) antigen presentation by MHC I to CD8+.

cells are loaded into MHC I to be presented to CD8+ cells that differentiate into cytotoxic T cells (CTLs) that kill infected or tumor cells (86). Cross presentation is the ability of APCs to present exogenous antigens to MHC I to activate CD8+ cells (Figure 5). This is important for vaccination against viruses and tumors. This can be achieved either by antigen uptake to the cytosol or antigen escape from the lysosome to cytosol to be degraded by proteasomes. Nanoparticles could show the ability to enhance antigen cross presentation as a potential strategy for developing effective cancer or anti-virus vaccines. Experiments indicated that different particles showed the ability to induce antigen cross presentation in DCs such as γ -PGA NPs (88), PLGA NPs (89), polyethyleneimine NPs (90). The antigen cross presentation can be fortified by controlling the particle size and surface chemistry of the nanoparticles (91, 92).

1.7. Imaging of nanoparticles in skin

Imaging and tracking nanoparticles in skin is a prerequisite to assure the effectiveness of therapy or to study nanoparticles fate and cytotoxicity. This can be applied to track nanoparticles passive penetration or with using a penetration enhancement method as microneedles (93). It can also reveal the interaction of nanoparticles with biological tissue and cellular uptake. However, imaging in skin is a challenging task. Among the techniques commonly used for nanoparticles imaging in skin is confocal laser scanning microscopy (CLSM). It is known for its availability and ease of use for detection of fluorescent probes. It is a sensitive, selective and versatile method for fluorescence measurements. It can provide high resolution imaging with non-invasive optical sectioning and three-dimensional reconstructions of samples (94). Additionally, minimum or no sample preparation is required which is advantageous to avoid perturbation or damage to the tissue (95). However, on the other hand, CLSM is not the most superior technique when it comes to penetration depth and contrast when compared to multiphoton microscopy for example (96).

Skin is a challenging tissue for fluorescence imaging due to its density that reflects and scatters incident light, in addition to skin's endogenous chromophores that attenuate visible light. Skin is autofluorescent over a wide range of wavelengths due to the endogenous fluorophores such as melanin, NADH, NADPH, keratin, elastin, porphyrin,

etc (97), which can interfere with the detection of many fluorescent probes. For this reason, the process of selecting an ideal fluorophore for imaging in skin is not an easy task. It is necessary to select fluorophores with distinct emission spectra from that of skin (95). On the other hand, to minimize the interference from skin autofluorescence, the imaging setup can be optimized to offset the skin fluorescence before imaging the fluorescent probe (98, 99) which is only possible for strong fluorescent signals. This renders the simultaneous imaging of skin and exogenous fluorophores challenging. One method can be the pre-staining of skin with another fluorophore with minimum cross-talk to the fluorophore under test, so both of them can be imaged simultaneously (100). However, simpler and time-saving methods are required. In this regard, we introduce through this research work a method for simultaneous imaging of skin and fluorophores using spectral analysis and linear unmixing. The method depends on recording the emission spectrum of the sample and efficiently separate it into the individual components using the pre-recorded emission spectra of the components (fingerprints) as references based on a mathematical algorithm (101).

1.7.1. Different imaging agents for nanoparticles tracking using CLSM

1.7.1.1. Dyes

Dyes represent the most common fluorophores for nanoparticles imaging. They are either covalently bound to the nanocarriers or physically loaded and distributed within the particles. Usually, the imaging probe is selected to have similar physicochemical properties to the drug under investigation. Derivatives of rhodamine and fluorescein are well known dyes for imaging of nanoparticles in skin. Rhodamine is a lipophilic dye that can be used for labelling of lipid-based nanoparticles (99). On the other hand, fluorescein can be used for conjugation with polymeric delivery systems such as dendrimers (102).

1.7.1.2. Quantum dots

Quantum dots are fluorescent semiconductor inorganic nanocrystals (2-10 nm) that show material- and size-dependent emission (103). They usually have high quantum yield and are resistant to photobleaching. Generally, they compose of a cadmium selenide (CdSe) core with a zinc sulfide (ZnS) or a cadmium sulfide (CdS) shell.

However, Cd can be released from the core to the medium and cause cytotoxicity. Consequently, surface modifications as coating (e.g. with poly ethylene glycol) or charge modification are required to control their toxicity (104). Quantum dots were used themselves as a fluorescent model for nanoparticles to test their ability to penetrate skin (104, 105) or have been loaded in nanocarriers (e.g. ethosomes) as an imaging probe (106).

1.7.1.3. Gold nanoclusters

Gold nanoclusters are ultra-small (< 2nm) particles that compose of several to hundreds of gold atoms that are stabilized by ligands of different functional groups mainly proteins and peptides (107). Their ultra-small size is comparable to the Fermi wavelength of electrons. In this size range, the strong quantum confinement of the free electrons results in discrete electronic states and consequently gold nanoclusters show molecule-like properties (108). They are different from larger gold nanoparticles, as they do not exhibit Plasmon resonance. Instead, they absorb and emit light in the visible or near infra-red range (109). They show superior photochemical stability compared to organic fluorophores. The tunable emission wavelength of the nanoclusters offers wide variability in applications, including bioimaging and biosensing (108). These nanoclusters have been widely used for cell and *in vivo* imaging (108). For example, functionalization of gold nanoclusters with molecules such as folic acid will dedicate them for cancer cells recognition (110). In addition, they showed success in live cell imaging to monitor the real-time cellular changes (111). On the other hand, gold nanoclusters have been used for *in vivo* imaging in animal models (mice) when injected intravenously to monitor their body distribution (112, 113).

Different methods have been studied for gold nanoclusters preparation:

- a) Gold salt reduction: Gold ions Au (III) are partially reduced in the presence of thiols into Au (I) thiolate oligomers. Addition of a strong reducing agent as NaBH₄ results in the complete reduction of gold ions into Au (0). Aggregation of Au atoms is controlled by the excess thiols to form nanoclusters of uniform size (114).
- b) Templated synthesis using macromolecules: Proteins, DNA, dendrimers and other macromolecules can be utilized as a template for stabilization of the nanoclusters (114). Protein-stabilized gold nanoclusters offer many advantages such as water-

dispersability, biocompatibility, ease of conjugation, large Stokes shift and long lifetime, which make them a good choice for bioimaging (115). Additionally, proteins are biologically active moieties that can fulfill a desired function (114).

- c) Chemical Etching: Gold nanoclusters can be prepared from larger gold nanoparticles by ligands acting as etching agent, which etch gold atoms from the surface of gold nanoparticles, then stabilize the atoms to form stable gold nanoclusters (116).

Different factors control the fluorescence properties of gold nanoclusters including their size, structure, oxidation states, interaction with the ligand and environmental conditions such as temperature, pH and ionic strength (115).

- a) Size: The fluorescence mechanism of gold nanoclusters is not completely understood, but different factors have been studied to understand more about their structure-properties relationship. Gold nanoclusters have a general structure of metal core-shell that is stabilized by ligands forming staple-like motifs on the surface (117). The number of gold atoms in the core controls the fluorescence properties of the nanoclusters. It has been reported that changing the core size from Au₁₂ to Au₆ resulted in increase in the quantum yield from 0.57 to 3.15% (118).
- b) Oxidation state: The oxidation state of Au is affecting the final fluorescence properties of the nanocluster. For thiolated-nanoclusters, the fluorescence depends on the electron transfer from S to Au. The oxidation state of the gold core is highly affecting the charge transfer efficiency and thus the fluorescence (115).
- c) Ligand effect: Ligands play an important role in controlling the properties of gold nanoclusters, due to the charge transfer from ligand to the metal core (119). For thiolated gold nanoclusters, increasing the electron donation efficiency of S or the ligand density on the nanoclusters surface can enhance the fluorescence (115).

Gold nanoclusters have been encapsulated in several drugs nanocarriers to function as an imaging probe such as chitosan (120) and bovine serum albumin (121). Through

our current research, we contribute toward the application of gold nanoclusters by loading them in gelatin nanoparticles for imaging in a dense challenging tissue as human skin. Furthermore, we tried to elicit the organisation of additional silver atoms and the resulting structures.

1.8. Disclosure

Figures of the introduction were created with the aid of BioRender and Servier medical art.

1.9. References

1. Donnelly RF, Singh TRR, Morrow DIJ, Woolfson AD. Transdermal delivery applications. *Microneedle-Mediated Transdermal and Intradermal Drug Delivery*: Wiley-Blackwell; 2012. p. 216.
2. Bal SM, Ding Z, van Riet E, Jiskoot W, Bouwstra JA. Advances in transcutaneous vaccine delivery: Do all ways lead to Rome? *J Control Release*. 2010;148(3):266-82.
3. Banerjee R. Overcoming the stratum corneum barrier: a nano approach. *Drug Deliv Transl Res*. 2013;3(3):205-8.
4. El-Sayed N, El-Khourdagui L, Schneider M. Insights into interactions of gold nanoparticles with the skin and potential dermatological applications. In: Hamblin MR, Avci P, Prow TW, editors. *Nanoscience in Dermatology*. Boston: Academic Press; 2016. p. 99-113.
5. Bos JD, Meinardi MMHM. The 500 Dalton rule for the skin penetration of chemical compounds and drugs. *Exp Dermatol*. 2000;9(3):165-9.
6. Schneider M, Stracke F, Hansen S, Schaefer UF. Nanoparticles and their interactions with the dermal barrier. *Dermato-Endocrinology*. 2009;1(4):197-206.
7. Uchechi O, Ogbonna JDN, Attama AA. Nanoparticles for dermal and transdermal drug delivery. In: Sezer AD, editor. *Application of Nanotechnology in Drug Delivery*: IntechOpen; 2014.
8. Lademann J, Patzelt A, Richter H, Antoniou C, Sterry W, Knorr F. Determination of the cuticula thickness of human and porcine hairs and their potential influence on the penetration of nanoparticles into the hair follicles. *J Biomed Opt*. 2009;14(2):021014.
9. Marshall JS, Warrington R, Watson W, Kim HL. An introduction to immunology and immunopathology. *Allergy Asthma Clin Immunol*. 2018;14(2):49.
10. Partidos CD, Muller S. Decision-making at the surface of the intact or barrier disrupted skin: potential applications for vaccination or therapy. *Cell Mol Life Sci*. 2005;62(13):1418-24.
11. Matzinger P. The danger model: A renewed sense of self. *Science*. 2002;296(5566):301.
12. Kubach J, Becker C, Schmitt E, Steinbrink K, Huter E, Tuettenberg A, et al. Dendritic cells: sentinels of immunity and tolerance. *Int J Hematol*. 2005;81(3):197-203.
13. Nicolas J-F, Guy B. Intradermal, epidermal and transcutaneous vaccination: from immunology to clinical practice. *Expert Rev Vaccines*. 2008;7(8):1201-14.

14. Mbongue J, Nicholas D, Firek A, Langridge W. The role of dendritic cells in tissue-specific autoimmunity. *J Immunol Res*. 2014;2014:17.
15. Apostolopoulos V, Thalhammer T, Tzakos AG, Stojanovska L. Targeting antigens to dendritic cell receptors for vaccine development. *J Drug Deliv*. 2013;2013:22.
16. Iijima N, Yanagawa Y, Iwabuchi K, Onoé K. Selective regulation of CD40 expression in murine dendritic cells by thiol antioxidants. *Immunology*. 2003;110(2):197-205.
17. Kwon KM, Lim S-M, Choi S, Kim D-H, Jin H-E, Jee G, et al. Microneedles: quick and easy delivery methods of vaccines. *Clin Exp Vaccine Res*. 2017;6(2):156-9.
18. Matsuo K, Hirobe S, Okada N, Nakagawa S. Frontiers of transcutaneous vaccination systems: Novel technologies and devices for vaccine delivery. *Vaccine*. 2013;31(19):2403-15.
19. McConville A, Hegarty C, Davis J. Mini-review: Assessing the potential impact of microneedle technologies on home healthcare applications. *Medicines (Basel)*. 2018;5(2):50.
20. Kalluri H, Kolli C, Banga A. Characterization of microchannels created by metal microneedles: formation and closure. *AAPS J*. 2011;13(3):473-81.
21. Chen J, Qiu Y, Zhang S, Yang G, Gao Y. Controllable coating of microneedles for transdermal drug delivery. *Drug Dev Ind Pharm*. 2015;41(3):415-22.
22. Larrañeta E, Lutton REM, Woolfson AD, Donnelly RF. Microneedle arrays as transdermal and intradermal drug delivery systems: Materials science, manufacture and commercial development. *Mat Sci Eng R*. 2016;104:1-32.
23. Gupta J, Gill HS, Andrews SN, Prausnitz MR. Kinetics of skin resealing after insertion of microneedles in human subjects. *J Control Release*. 2011;154(2):148-55.
24. Ita K. Transdermal delivery of drugs with microneedles—Potential and challenges. *Pharmaceutics*. 2015;7(3):90-105.
25. Cheung K, Han T, Das DB. Effect of force of microneedle insertion on the permeability of insulin in skin. *J Diabetes Sci Technol*. 2014;8(3):444-52.
26. Miller PR, Taylor RM, Tran BQ, Boyd G, Glaros T, Chavez VH, et al. Extraction and biomolecular analysis of dermal interstitial fluid collected with hollow microneedles. *Commun Biol*. 2018;1(1):173.
27. Balmert SC, Carey CD, Falo GD, Sethi SK, Erdos G, Korkmaz E, et al. Dissolving undercut microneedle arrays for multicomponent cutaneous vaccination. *J Control Release*. 2019;317:336-46.
28. Donadei A, Kraan H, Ophorst O, Flynn O, O'Mahony C, Soema PC, et al. Skin delivery of trivalent Sabin inactivated poliovirus vaccine using dissolvable microneedle patches induces neutralizing antibodies. *J Control Release*. 2019;311-312:96-103.
29. Zhao X, Li X, Zhang P, Du J, Wang Y. Tip-loaded fast-dissolving microneedle patches for photodynamic therapy of subcutaneous tumor. *J Control Release*. 2018;286:201-9.
30. Yan Q, Cheng Z, Liu H, Shan W, Cheng Z, Dai X, et al. Enhancement of Ag85B DNA vaccine immunogenicity against tuberculosis by dissolving microneedles in mice. *Vaccine*. 2018;36(30):4471-6.
31. Dillon C, Hughes H, O'Reilly NJ, Allender CJ, Barrow DA, McLoughlin P. Dissolving microneedle based transdermal delivery of therapeutic peptide analogues. *Int J Pharm*. 2019;565:9-19.
32. Yao W, Tao C, Zou J, Zheng H, Zhu J, Zhu Z, et al. Flexible two-layer dissolving and safing microneedle transdermal of neurotoxin: A biocomfortable attempt to treat rheumatoid arthritis. *Int J Pharm*. 2019;563:91-100.

33. Guo T, Cheng N, Zhao J, Hou X, Zhang Y, Feng N. Novel nanostructured lipid carriers-loaded dissolving microneedles for controlled local administration of aconitine. *Int J Pharm.* 2019;572:118741.
34. Bhatnagar S, Bankar NG, Kulkarni MV, Venuganti VVK. Dissolvable microneedle patch containing doxorubicin and docetaxel is effective in 4T1 xenografted breast cancer mouse model. *Int J Pharm.* 2019;556:263-75.
35. Rodgers AM, McCrudden MTC, Vincente-Perez EM, Dubois AV, Ingram RJ, Larrañeta E, et al. Design and characterisation of a dissolving microneedle patch for intradermal vaccination with heat-inactivated bacteria: A proof of concept study. *Int J Pharm.* 2018;549(1):87-95.
36. Waghule T, Singhvi G, Dubey SK, Pandey MM, Gupta G, Singh M, et al. Microneedles: A smart approach and increasing potential for transdermal drug delivery system. *Biomed Pharmacother.* 2019;109:1249-58.
37. Samant PP, Prausnitz MR. Mechanisms of sampling interstitial fluid from skin using a microneedle patch. *Proc Natl Acad Sci.* 2018;115(18):4583-8.
38. Cummings JP, Walsh JT. Tissue tearing caused by pulsed laser-induced ablation pressure. *Appl Optics.* 1993;32(4):494-503.
39. Walsh Jr. JT, Flotte TJ, Deutsch TF. Er:YAG laser ablation of tissue: Effect of pulse duration and tissue type on thermal damage. *Laser Surg Med.* 1989;9(4):314-26.
40. Scheibelhofer S, Thalhamer J, Weiss R. Laser microporation of the skin: prospects for painless application of protective and therapeutic vaccines. *Expert Opin Drug Deliv.* 2013;10(6):761-73.
41. Machado Y, Duinkerken S, Hoepflinger V, Mayr M, Korotchenko E, Kurtaj A, et al. Synergistic effects of dendritic cell targeting and laser-microporation on enhancing epicutaneous skin vaccination efficacy. *J Control Release.* 2017;266:87-99.
42. Prausnitz MR, Bose VG, Langer R, Weaver JC. Electroporation of mammalian skin: a mechanism to enhance transdermal drug delivery. *Proc Natl Acad Sci.* 1993;90(22):10504-8.
43. Chiarella P, Fazio VM, Signori E. Application of electroporation in DNA vaccination protocols. *Curr Gene Ther.* 2010;10(10):281-6.
44. Chen W, Carbone FR, McCluskey J. Electroporation and commercial liposomes efficiently deliver soluble protein into the MHC class I presentation pathway: Priming in vitro and in vivo for class I-restricted recognition of soluble antigen. *J Immunol Methods.* 1993;160(1):49-57.
45. Bernelin-Cottet C, Urien C, McCaffrey J, Collins D, Donadei A, McDaid D, et al. Electroporation of a nanoparticle-associated DNA vaccine induces higher inflammation and immunity compared to its delivery with microneedle patches in pigs. *J Control Release.* 2019;308:14-28.
46. Chiarella P, Massi E, De Robertis M, Sibilio A, Parrella P, Fazio VM, et al. Electroporation of skeletal muscle induces danger signal release and antigen-presenting cell recruitment independently of DNA vaccine administration. *Expert Opin Biol Ther.* 2008;8(11):1645-57.
47. Namjoshi S, Benson HAE. Transdermal delivery of vaccines. In: Hefferon KL, editor. *Novel Approaches to Vaccine Research* 2011.
48. Ogura M, Paliwal S, Mitragotri S. Low-frequency sonophoresis: Current status and future prospects. *Adv Drug Deliver Rev.* 2008;60(10):1218-23.

49. Polat BE, Blankschtein D, Langer R. Low-frequency sonophoresis: application to the transdermal delivery of macromolecules and hydrophilic drugs. *Expert Opin Drug Deliv.* 2010;7(12):1415-32.
50. Tezel A, Paliwal S, Shen Z, Mitragotri S. Low-frequency ultrasound as a transcutaneous immunization adjuvant. *Vaccine.* 2005;23(29):3800-7.
51. Mitragotri S. Current status and future prospects of needle-free liquid jet injectors. *Nat Rev Drug Discov.* 2006;5(7):543-8.
52. Paudel KS, Milewski M, Swadley CL, Brogden NK, Ghosh P, Stinchcomb AL. Challenges and opportunities in dermal/transdermal delivery. *Ther Deliv.* 2010;1(1):109-31.
53. Chen X, Shah D, Kosiratna G, Manstein D, Anderson RR, Wu MX. Facilitation of transcutaneous drug delivery and vaccine immunization by a safe laser technology. *J Control Release.* 2012;159(1):43-51.
54. Etchart N, Hennino A, Friede M, Dahel K, Dupouy M, Goujon-Henry C, et al. Safety and efficacy of transcutaneous vaccination using a patch with the live-attenuated measles vaccine in humans. *Vaccine.* 2007;25(39):6891-9.
55. Pati R, Shevtsov M, Sonawane A. Nanoparticle vaccines against infectious diseases. *Front Immunol.* 2018;9(2224).
56. Tyagi RK, Garg NK, Sahu T. Vaccination strategies against malaria: Novel carrier(s) more than a tour de force. *J Control Release.* 2012;162(1):242-54.
57. Chattopadhyay S, Chen J-Y, Chen H-W, Hu C-MJ. Nanoparticle vaccines adopting virus-like features for enhanced immune potentiation. *Nanotheranostics.* 2017;1(3):244-60.
58. Sharma S, Mukkur TKS, Benson HAE, Chen Y. Pharmaceutical aspects of intranasal delivery of vaccines using particulate systems. *J Pharm Sci.* 2009;98(3):812-43.
59. Gupta PN, Khatri K, Goyal AK, Mishra N, Vyas SP. M-cell targeted biodegradable PLGA nanoparticles for oral immunization against hepatitis B. *J Drug Target.* 2007;15(10):701-13.
60. Diwan M, Tafaghodi M, Samuel J. Enhancement of immune responses by co-delivery of a CpG oligodeoxynucleotide and tetanus toxoid in biodegradable nanospheres. *J Control Release.* 2002;85(1):247-62.
61. Jung H-H, Kim S-H, Moon J-H, Jeong S-U, Jang S, Park C-S, et al. Polymeric nanoparticles containing both antigen and vitamin D3 induce antigen-specific immune suppression. *Immune Netw.* 2019;19(3).
62. Akhilesh Kumar S, Harishkumar M. Polymeric nanoparticles for vaccine delivery. Integrating biologically-inspired nanotechnology into medical practice. Hershey, PA, USA: IGI Global; 2017. p. 32-49.
63. Elzoghby AO. Gelatin-based nanoparticles as drug and gene delivery systems: Reviewing three decades of research. *J Control Release.* 2013;172(3):1075-91.
64. Yasmin R, Shah M, Khan Saeed A, Ali R. Gelatin nanoparticles: a potential candidate for medical applications. *Nanotechnol Rev.* 2017. p. 191.
65. Sudheesh MS, Vyas SP, Kohli DV. Nanoparticle-based immunopotentiality via tetanus toxoid-loaded gelatin and aminated gelatin nanoparticles. *Drug Deliv.* 2011;18(5):320-30.
66. Lin S-F, Jiang P-L, Tsai J-S, Huang Y-Y, Lin S-Y, Lin J-H, et al. Surface assembly of poly(I:C) on polyethyleneimine-modified gelatin nanoparticles as immunostimulatory carriers for mucosal antigen delivery. *J Biomed Mater Res B.* 2019;107(4):1228-37.

67. Sabet S, George MA, El-Shorbagy HM, Bassiony H, Farroh KY, Youssef T, et al. Gelatin nanoparticles enhance delivery of hepatitis C virus recombinant NS2 gene. *PLOS ONE*. 2017;12(7):e0181723.
68. Leo E, Angela Vandelli M, Cameroni R, Forni F. Doxorubicin-loaded gelatin nanoparticles stabilized by glutaraldehyde: Involvement of the drug in the cross-linking process. *Int J Pharm*. 1997;155(1):75-82.
69. Gough JE, Scotchford CA, Downes S. Cytotoxicity of glutaraldehyde crosslinked collagen/poly(vinyl alcohol) films is by the mechanism of apoptosis. *J Biomed Mater Res*. 2002;61(1):121-30.
70. El-Sayed N, Trouillet V, Clasen A, Jung G, Hollemeyer K, Schneider M. NIR-emitting gold nanoclusters–modified gelatin nanoparticles as a bioimaging agent in tissue. *Adv Healthcare Mater*. 2019;8(24):1900993.
71. Baseer A, Koenneke A, Zapp J, Khan SA, Schneider M. Design and characterization of surface-crosslinked gelatin nanoparticles for the delivery of hydrophilic macromolecular drugs. *Macromol Chem Phys*. 2019;220(18):1900260.
72. Khan SA, Schneider M. Improvement of nanoprecipitation technique for preparation of gelatin nanoparticles and potential macromolecular drug loading. *Macromol Biosci*. 2013;13(4):455-63.
73. Salaün F. Microencapsulation technology for smart textile coatings. In: Hu J, editor. *Active Coatings for Smart Textiles*: Woodhead Publishing; 2016. p. 179-220.
74. Gupta AK, Gupta M, Yarwood SJ, Curtis ASG. Effect of cellular uptake of gelatin nanoparticles on adhesion, morphology and cytoskeleton organisation of human fibroblasts. *J Control Release*. 2004;95(2):197-207.
75. Alexandra S, Carabineiro C. Applications of gold nanoparticles in nanomedicine: Recent advances in vaccines. *Molecules*. 2017;22(5):857.
76. Niikura K, Matsunaga T, Suzuki T, Kobayashi S, Yamaguchi H, Orba Y, et al. Gold Nanoparticles as a Vaccine Platform: Influence of Size and Shape on Immunological Responses in Vitro and in Vivo. *ACS Nano*. 2013;7(5):3926-38.
77. Mody KT, Popat A, Mahony D, Cavallaro AS, Yu C, Mitter N. Mesoporous silica nanoparticles as antigen carriers and adjuvants for vaccine delivery. *Nanoscale*. 2013;5(12):5167-79.
78. Liu Q, Jia J, Yang T, Fan Q, Wang L, Ma G. Pathogen-mimicking polymeric nanoparticles based on dopamine polymerization as vaccines adjuvants induce robust humoral and cellular immune responses. *Small*. 2016;12(13):1744-57.
79. Hanson MC, Crespo MP, Abraham W, Moynihan KD, Szeto GL, Chen SH, et al. Nanoparticulate STING agonists are potent lymph node–targeted vaccine adjuvants. *J Clin Invest* 2015;125(6):2532-46.
80. Swartz MA. The physiology of the lymphatic system. *Adv Drug Deliver Rev*. 2001;50(1):3-20.
81. Dane KY, Nembrini C, Tomei AA, Eby JK, O'Neil CP, Velluto D, et al. Nano-sized drug-loaded micelles deliver payload to lymph node immune cells and prolong allograft survival. *J Control Release*. 2011;156(2):154-60.
82. De Temmerman M-L, Rejman J, Demeester J, Irvine DJ, Gander B, De Smedt SC. Particulate vaccines: on the quest for optimal delivery and immune response. *Drug Discov Today*. 2011;16(13):569-82.

83. Xiang SD, Scholzen A, Minigo G, David C, Apostolopoulos V, Mottram PL, et al. Pathogen recognition and development of particulate vaccines: Does size matter? *Methods*. 2006;40(1):1-9.
84. Champion JA, Mitragotri S. Shape induced inhibition of phagocytosis of polymer particles. *Pharm Res*. 2009;26(1):244-9.
85. Foged C, Brodin B, Frokjaer S, Sundblad A. Particle size and surface charge affect particle uptake by human dendritic cells in an in vitro model. *Int J Pharm*. 2005;298(2):315-22.
86. Ahmad S, Zamry AA, Tan H-TT, Wong KK, Lim J, Mohamud R. Targeting dendritic cells through gold nanoparticles: A review on the cellular uptake and subsequent immunological properties. *Mol Immunol*. 2017;91:123-33.
87. Cruz LJ, Tacke PJ, Zeelenberg IS, Srinivas M, Bonetto F, Weigelin B, et al. Tracking targeted bimodal nanovaccines: Immune responses and routing in cells, tissue, and whole organism. *Mol Pharm*. 2014;11(12):4299-313.
88. Yoshikawa T, Okada N, Oda A, Matsuo K, Matsuo K, Kayamuro H, et al. Nanoparticles built by self-assembly of amphiphilic γ -PGA can deliver antigens to antigen-presenting cells with high efficiency: A new tumor-vaccine carrier for eliciting effector T cells. *Vaccine*. 2008;26(10):1303-13.
89. Song C, Noh Y, Lim Y. Polymer nanoparticles for cross-presentation of exogenous antigens and enhanced cytotoxic T-lymphocyte immune response. *Int J Nanomedicine*. 2016;11:3753-64.
90. Chen J, Li Z, Huang H, Yang Y, Ding Q, Mai J, et al. Improved antigen cross-presentation by polyethyleneimine-based nanoparticles. *Int J Nanomedicine*. 2011;6:77–84.
91. Yang Y-W, Hsu PY-J. The effect of poly(D,L-lactide-co-glycolide) microparticles with polyelectrolyte self-assembled multilayer surfaces on the cross-presentation of exogenous antigens. *Biomaterials*. 2008;29(16):2516-26.
92. Han R, Zhu J, Yang X, Xu H. Surface modification of poly(D,L-lactic-co-glycolic acid) nanoparticles with protamine enhanced cross-presentation of encapsulated ovalbumin by bone marrow-derived dendritic cells. *J Biomed Mater Res A*. 2011;96A(1):142-9.
93. Zhang W, Gao J, Zhu Q, Zhang M, Ding X, Wang X, et al. Penetration and distribution of PLGA nanoparticles in the human skin treated with microneedles. *Int J Pharm*. 2010;402(1):205-12.
94. Pygall SR, Whetstone J, Timmins P, Melia CD. Pharmaceutical applications of confocal laser scanning microscopy: The physical characterisation of pharmaceutical systems. *Adv Drug Deliver Rev*. 2007;59(14):1434-52.
95. Rossetti FbC, Depieri LvV, Bentley MVrLB. Confocal laser scanning microscopy as a tool for the investigation of skin drug delivery systems and diagnosis of skin disorders, confocal laser microscopy. In: Neil Lagali, editor. *Principles and Applications in Medicine, Biology, and the Food Sciences*: IntechOpen; 2013.
96. Kaur N, Aditya RN, Singh A, Kuo T-R. Biomedical applications for gold nanoclusters: Recent developments and future perspectives. *Nanoscale Res Lett*. 2018;13(1):302.
97. Alvarez-Román R, Naik A, Kalia YN, Fessi H, Guy RH. Visualization of skin penetration using confocal laser scanning microscopy. *Eur J Pharm Biopharm*. 2004;58(2):301-16.
98. Lanke SSS, Kolli CS, Strom JG, Banga AK. Enhanced transdermal delivery of low molecular weight heparin by barrier perturbation. *Int J Pharm*. 2009;365:26-33.

-
99. Angelo T, El-Sayed N, Jurisic M, Koenneke A, Gelfuso GM, Cunha-Filho M, et al. Effect of physical stimuli on hair follicle deposition of clobetasol-loaded lipid nanocarriers. *Sci Rep*. 2020;10(1):176.
100. Rastogi R, Anand S, Koul V. Flexible polymerosomes—An alternative vehicle for topical delivery. *Colloids Surf B Biointerfaces*. 2009;72(1):161-6.
101. Zimmermann T. Spectral imaging and linear unmixing in light microscopy. In: Rietdorf J, editor. *Microscopy Techniques*. Berlin, Heidelberg: Springer Berlin Heidelberg; 2005. p. 245-65.
102. Borowska K, Wołowiec S, Rubaj A, Głowniak K, Sieniawska E, Radej S. Effect of polyamidoamine dendrimer G3 and G4 on skin permeation of 8-methoxypsoralene—In vivo study. *Int J Pharm*. 2012;426(1):280-3.
103. Pawar RS, Upadhya PG, Patravale VB. Quantum dots: Novel realm in biomedical and pharmaceutical industry. In: Mustansar Hussain C, editor. *Handbook of Nanomaterials for Industrial Applications*: Elsevier; 2018. p. 621-37.
104. Zhang LW, Yu WW, Colvin VL, Monteiro-Riviere NA. Biological interactions of quantum dot nanoparticles in skin and in human epidermal keratinocytes. *Toxicol Appl Pharm*. 2008;228(2):200-11.
105. Gratieri T, Schaefer U, Jing L, Gao M, Kostka K-H, Lopez RFV, et al. Penetration of quantum dot particles through human skin. *J Biomed Nanotechnol*. 2010;6:586–95.
106. He R, Cui D-x, Gao F. Preparation of fluorescence ethosomes based on quantum dots and their skin scar penetration properties. *Mater Lett*. 2009;63(20):1662-4.
107. Li H, Zhu W, Wan A, Liu L. The mechanism and application of the protein-stabilized gold nanocluster sensing system. *Analyst*. 2017;142(4):567-81.
108. Chen L-Y, Wang C-W, Yuan Z, Chang H-T. Fluorescent gold nanoclusters: Recent advances in sensing and imaging. *Anal Chem*. 2015;87(1):216-29.
109. Zheng J, Zhou C, Yu M, Liu J. Different sized luminescent gold nanoparticles. *Nanoscale*. 2012;4(14):4073-83.
110. Retnakumari A, Setua S, Menon D, Ravindran P, Muhammed H, Pradeep T, et al. Molecular-receptor-specific, non-toxic, near-infrared-emitting Au cluster-protein nanoconjugates for targeted cancer imaging. *Nanotechnology*. 2009;21(5):055103.
111. Zhuang M, Ding C, Zhu A, Tian Y. Ratiometric fluorescence probe for monitoring hydroxyl radical in live cells based on gold nanoclusters. *Anal Chem*. 2014;86(3):1829-36.
112. Zhang P, Yang XX, Wang Y, Zhao NW, Xiong ZH, Huang CZ. Rapid synthesis of highly luminescent and stable Au₂₀ nanoclusters for active tumor-targeted imaging in vitro and in vivo. *Nanoscale*. 2014;6(4):2261-9.
113. Chen Y, Montana DM, Wei H, Cordero JM, Schneider M, Le Guével X, et al. Shortwave infrared in vivo imaging with gold nanoclusters. *Nano Lett*. 2017;17(10):6330-4.
114. Cantelli A, Battistelli G, Guidetti G, Manzi J, Di Giosia M, Montalti M. Luminescent gold nanoclusters as biocompatible probes for optical imaging and theranostics. *Dyes Pigm*. 2016;135:64-79.
115. Chen L-Y, Wang C-W, Yuan Z, Chang H-T. Fluorescent Gold Nanoclusters: Recent advances in sensing and imaging. *Anal Chem*. 2015;87:216-29.
116. Duan H, Nie S. Etching colloidal gold nanocrystals with hyperbranched and multivalent polymers: A new route to fluorescent and water-soluble atomic clusters. *J Am Chem Soc*. 2007;129(9):2412-3.

117. Zhang P. X-Ray Spectroscopy of Gold–Thiolate Nanoclusters. *J Phys Chem C*. 2014;118:25291-9.
118. Bain D, Maity S, Paramanik B, Patra A. Core-size dependent fluorescent gold nanoclusters and ultrasensitive detection of Pb²⁺ Ion. *ACS Sustain Chem Eng*. 2018;6:2334-43.
119. Wu Z, Jin R. On the ligand's role in the fluorescence of gold nanoclusters. *Nano Lett*. 2010;10:2568-73.
120. Sahoo AK, Banerjee S, Ghosh SS, Chattopadhyay A. Simultaneous RGB emitting Au nanoclusters in chitosan nanoparticles for anticancer gene theranostics. *Acs Appl Mater Inter*. 2014;6(1):712-24.
121. Khandelia R, Bhandari S, Pan UN, Ghosh SS, Chattopadhyay A. Gold nanocluster embedded albumin nanoparticles for two-photon imaging of cancer cells accompanying drug delivery. *Small*. 2015;11(33):4075-81.

Chapter 2. Research Objectives

2. Research Objectives

Nanoparticles have gained the interest for vaccine delivery due to their ability to provide interesting functionalities such as antigen protection against degradation, controlling the release rate of the antigen, presenting the antigen to dendritic cells in a way that mimics pathogens. In turn, enhancement and modulation of the immune response can be achieved. Transcutaneous administration of nanoparticles is an attractive route of vaccination due to the richness of skin in immune cells. For this purpose, nanoparticles have to be combined with skin penetration methods such as microneedles or skin laser microporation. These techniques allow the nanoparticles to bypass the stratum corneum, which is the main barrier of skin, to the viable skin (epidermis or dermis) where Langerhans cells and dermal dendritic cells locate. For better understanding of the nanoparticles interactions with dendritic cells and for nanoparticle tracking in skin, development of theranostic nanoparticles is required. However, imaging together with or in a dense and autofluorescent tissue such as skin is challenging. Consequently, an optimal biocompatible imaging agent that emits near infrared light, which is the optical window of tissue, is required.

Accordingly, the current thesis aims to fulfill the following objectives:

Chapter 3: Development of gold nanoclusters as a novel imaging agent that emits light in the near infrared region. This can be achieved by:

- Synthesis of gold nanoclusters using gelatin and further formulation of gelatin nanoparticles.
- Optimization and enhancement of the fluorescence properties of gold nanoclusters and deeper insights into of their structure-properties relationship.
- Imaging of the fluorescent gold nanoclusters-modified gelatin nanoparticles in human skin.
-

Chapter 4: Development and customization of dissolving microneedles loaded with the nanoparticles for transcutaneous delivery. This can be achieved by:

- Using 3D printing as an accessible and cost-effective method for developing master molds of variable designs to further use it for microneedles preparation.

- Preparation of microneedles with special 'tanto blade' design and modification of the microneedles patches to fasten the microneedles separation from the patch into skin to decrease the application time.
- Loading of the fluorescent gold nanoclusters-modified gelatin nanoparticles into the microneedles and imaging them *in vitro* and *ex vivo* in human skin.

Chapter 5: Delivery of ovalbumin to dendritic cells using the developed theranostic gelatin nanoparticles and modulation of the immune response. This can be achieved by:

- Introducing two designs of the nanoparticles by either loading ovalbumin to the surface of the nanoparticles or encapsulating it within the matrix of the nanoparticles.
- Surface functionalization of the nanoparticles to enhance the interaction and uptake by dendritic cells
- Studying the effect of the nanoparticles formulations on the activation of dendritic cells and proliferation of naïve T cells.

Chapter 3. NIR-Emitting Gold Nanoclusters-Modified Gelatin Nanoparticles as a Bioimaging Agent in Tissue

Nesma El-Sayed, Vanessa Trouillet, Anne Clasen, Gregor Jung, Klaus Hollemeyer and Marc Schneider

** This chapter has been published as a research article in in **Advanced Healthcare Materials**, 2019*

3. NIR-Emitting Gold Nanoclusters-Modified Gelatin Nanoparticles as a Bioimaging Agent in Tissue

3.1. Abstract

Gold nanoclusters (AuNCs) synthesis using gelatin which is a well-distinguished polymer for nanoparticle-mediated drug delivery, will open the door for developing efficient theranostics based on pharmaceutically accepted materials. Gelatin-stabilized AuNCs have been synthesized and for tuning the emission spectra, they were further modified using glutathione. Moreover, the addition of silver ions to the preparation enhanced the fluorescence to reach a high quantum yield of 26.7%. We have developed a hypothetical model describing the nanoclusters' properties-structure relationship based on X-ray photoelectron spectroscopy data and synthesis sequence. Additionally, these modifications have improved the fluorescence stability toward pH changes and enzymatic degradation. The effect of nanoclusters formation on the integrity of gelatin structure has been explored using FT-IR and MALDI-TOF MS, being important to further formulate gelatin nanoparticles (GNPs). The prepared 218 nm-sized NPs showed no cytotoxicity up to 600 µg/mL against keratinocytes and have been imaged in skin, which is a challenging autofluorescent tissue using confocal laser scanning microscopy (CLSM). The nanoparticles were delivered into skin using dissolving microneedles. Linear unmixing technique allowed for simultaneous imaging of both AuNCs-GNPs and skin autofluorescence with accurate signal separation. This underlines the great potential of applying the developed system for better understanding of the behavior and fate of nanomaterials in tissue. Additionally, it represents a potential carrier for biomedical cargos to further serve as a theranostic system.

Keywords: protein-stabilized gold nanoclusters, nanotechnology, drug delivery, theranostics, fluorescent enhancement

3.2. Introduction

Gold nanoclusters (AuNCs) have gained growing interest recently. This is attributed to their unique properties and their various potential applications including bioimaging, (1-4) biolabelling (5), sensing (3, 4, 6, 7), and therapy (8). Gold nanoclusters are composed of several up to tens of gold atoms giving rise to ultra-small sized structures of less than 2 nm (9). Due to their small size, they demonstrate molecule-like properties having discrete valence electronic states drawing near the molecular orbitals (10, 11). They do not exhibit plasmon resonance compared to larger gold nanoparticles but rather they show fluorescence in the visible or the near-infrared light region (12). Among their unique properties, having long lifetime NIR fluorescence, high two-photon excitation and photostability alongside with biocompatibility (13) allow them to be attractive for imaging in tissue and *in vivo* (2).

In addition to the quantum confinement effect, ligands play an important role in controlling the chemical and physical properties of AuNCs (14). They generally have a metal core-shell structure, stabilized by ligands forming staple-like motifs on the surface (10). Controlling the core size during synthesis of the nanoclusters allows to tune the emission wavelength and intensity (15). On the other hand, charge transfer or electron donation from the ligands active groups to the metal core greatly contributes in regulating the fluorescence properties (16, 17). Besides, ligands can stabilize the fluorescence of AuNCs against environmental conditions such as change of pH and temperature, etc (18).

Proteins and peptides are attractive stabilizing, capping and templating agents for the synthesis of AuNCs. They offer essential attributes for the fabrication of metal nanoclusters such as the mild reaction environment, water solubility and biocompatibility (19), in addition to their biological, medicinal and pharmaceutical applications. Glutathione has been widely utilized for AuNCs synthesis (4, 20-24) due to the strong affinity of the thiol group to form Au-S bond (23, 25). Cysteine-containing proteins such as bovine serum albumin (BSA) (26-31), insulin (32, 33), trypsin (34, 35) and lysozyme (36, 37) have been also investigated for the same purpose. Other studies have also shown that basic amino acids together with tyrosine and tryptophan can contribute to the reduction of gold ions into atoms (38). In addition, the protein

organizational structure can control the NCs' properties, where amyloid fibril (cross- β -sheet structures) formation can lead to red-shift in fluorescence (39).

However, the mechanism of nanoclusters formation is still not fully understood. Careful selection of the suitable ligand is a prerequisite for optimizing and stabilizing the optical properties of the nanoclusters. On the other hand, establishing a correlation between the physicochemical properties of AuNCs to their structure is very crucial. This represents a step towards better understanding of the nanoclusters' behaviour and easier properties' manipulation to fulfill different applications. X-Ray Photoelectron Spectroscopy (XPS) can serve as a useful tool for investigating the effect of ligands on the atomic structure of AuNCs by studying the oxidation state of the elements forming the nanoclusters and the bonding properties as well (10, 27).

Synthesis of AuNCs labelled-pharmaceutical proteins and polymers will pave the way and allow to obtain multifunctional nanoparticles (NPs) for simultaneous drug delivery and bioimaging and/or biosensing. Gelatin is a versatile carrier commonly used for the delivery of biomacromolecules and hydrophilic drugs (40) due to its hydrophilic nature, biodegradability and biocompatibility. The biocompatibility of the multifunctional NPs is essential; where AuNCs are easily excreted from the body, due to their small size less than the renal clearance cut-off, and gelatin NPs are degraded and solubilized. To our knowledge, gelatin has not been investigated yet for synthesis of fluorescent AuNCs, despite its widespread use in preparation of gold nanoparticles. We envisage that the gelatin-mediated synthesis of AuNCs could open the door for different pharmaceutical or biomedical applications. In this respect, we succeeded in using gelatin to synthesize NIR-emitting AuNCs. We have managed to control the fluorescence properties of the nanoclusters by varying the conditions of the reaction. AuNCs-modified gelatine has proven capable of forming nanocarriers (GNPs) with the ultimate goal of imaging in tissue. Such system can be of high potential for theranostics for simultaneous bioimaging and delivery of macromolecules as antigens.

3.3. Materials and methods

3.3.1. Materials

Hydrogen tetrachloroaurate (III) trihydrate ($\text{HAuCl}_4 \cdot 3\text{H}_2\text{O}$), gelatin type B (from bovine skin, gel strength ~ 75 g Bloom), silver nitrate, N-(3-dimethylaminopropyl)-N'-ethylcarbodiimide hydrochloride (EDC), N-Hydroxysuccinimide (NHS), D-(+)-trehalose dihydrate, methanol, dimethyl sulfoxide were all purchased from Sigma Aldrich, Steinheim Germany. Ninhydrin (2,2-dihydroxyindane-1,3-dione) was purchased from Merck, Darmstadt, Germany. Trypsin from bovine pancreas (activity: 3273.4 U/mg) was obtained from PanReac AppliChem, Darmstadt, Germany. All chemicals were utilized without further purification. Milli-Q ultrapure water has been used for all experiments.

3.3.2. Synthesis of gelatin-stabilized AuNCs

Gold nanoclusters stabilized by gelatin have been prepared by adding HAuCl_4 to gelatin solution followed by adjusting the pH using 1N sodium hydroxide. The reaction has been carried out for 24h under vigorous mixing in a thermomixer (MHR, Hettich Benelux, Geldermalsen, The Netherlands) at 60 °C. Different HAuCl_4 concentrations (1-20 mM) and different pH values (7-12) have been tested for AuNCs formation evaluated by fluorescence evolution. The optimized nanoclusters (AuG) have been utilized for further investigations.

3.3.3. Synthesis of gelatin-stabilized AuNCs modified by glutathione

In one-pot reaction, glutathione (GSH) with different concentrations (5-25 mM) was added to 4% w/v gelatin, followed by addition of 10 mM HAuCl_4 . All other settings were adjusted as shown before and the reaction proceeded for 24h. The optimized formulation (AuS) has been applied for further modifications as will be shown later.

3.3.4. Gelatin structure integrity

Selected formulations showing the highest fluorescence were repeated following the previously mentioned procedure while varying the reaction time (1 - 24h). The fluorescence at the maximum wavelength was plotted against time and further the samples were examined for gel formation after cooling to 4 °C. The free amine groups in gelatin were quantified by ninhydrin test over different time intervals of interaction with gold. Briefly, pH of AuNCs-modified gelatin was adjusted to 7 by 1N HCl and mixed

vigorously (1000 rpm) with 3% ninhydrin solution in 90 % DMSO at 80 °C for 5 minutes. Then, the mixture was cooled down to room temperature for 30 min and absorbance was measured at 575 nm. Calibration curve was constructed using glycine as a standard (41) following the same procedure. Fourier transform infrared spectrometry (FT-IR) and matrix-assisted laser desorption/ionization time of flight mass spectroscopy (MALDI-TOF MS) were performed. Freeze-dried samples of selected AuNCs-modified gelatin have been scanned for their FT-IR spectrum between 4000 and 400 cm^{-1} (Spectrum 400, FT-IR/FT-NIR Spectrometer, PerkinElmer, Rodgau, Germany). For MALDI-TOF MS, samples were analysed in positive mode with a matrix of sinapinic acid using Applied Biosystems 4800 MALDI TOF/TOF analyzer (Applied Biosystems, Warrington, Cheshire, United Kingdom).

3.3.5. Synthesis of Ag-modified AuNCs stabilized by gelatin and glutathione

The GSH-modified gelatin stabilized AuNCs synthesized after optimized conditions (AuS) have been further modified using silver ions following two different protocols: (I) To form alloy metal NCs, AgNO_3 has been added during the formation of the nanoclusters. Effect of different Ag/Au ratio, reaction time, pH and temperature has been tested. (II) To modify the surface of AuNCs, AgNO_3 has been added after the synthesis of AuNCs. For screening, fluorescence spectra have been recorded for all tested formulations (550 - 850 nm) upon excitation at 368 nm using Microplate reader (Infinite M200, Tecan group Ltd, Männedorf, Switzerland).

3.3.6. Characterization of selected AuNCs formulations

Optical properties: 3D-Fluorescence spectra have been recorded using Jasco spectrofluorometer FP-6500 (JASCO) in 1 cm cuvette with excitation wavelengths 380-650 nm and emission range 450-750 nm. Time-correlated single photon counting (TCSPC) measurements have been performed with a home-built setup. Excitation was done with a pulsed laser diode (PicoQuant, LDH-P-C-470, $\lambda=470$ nm; pulse width < 100 ps) which was controlled by a diode laser driver unit (PDL 808 MC SEPIA, PicoQuant). After filtering through a band pass filter (685/70, AHF Analysentechnik), a single-photon avalanche detector (PDM 100ct SPAD, Micro Photon Devices) in combination with a photon counting device (PicoHarp 300, PicoQuant) was used for

detection. To record the instrumental response function (IRF), a diluted colloidal silica solution (LUDOX TM-50, Sigma Aldrich) was used and the overall instrumental response function was 300 ps (FWHM). All fluorescence lifetimes were measured under magic angle conditions. The collected data was analysed using exponential fit functions (SymPhoTime, (PicoQuant) software). The fluorescence quantum yield was measured on an Absolute PL Quantum Yield Spectrometer C11347 (Hamamatsu) using an Ulbricht sphere in scan mode (emission range from 196 nm to 958 nm), using blanks prepared the same as the nanoclusters without Au or Ag addition as references. Fluorescence imaging has been carried out by confocal microscope (LSM 710, Zeiss, Jena, Germany) using excitation laser of 405 nm and emission was detected between 600 - 740 nm.

Transmission electron microscopy (TEM): Drop of AuNCs-modified GNPs has been loaded on a carbon-coated copper TEM grid. The drop was left to deposit on the grid for 45 s and then the excess was carefully removed with Kimtech® tissue. After drying, 2% uranyl acetate solution was used to stain the sample for 45 s and again the excess liquid has been removed. Finally, the grid was let to dry for 2 min and subsequently washed using a drop of water for few seconds and then was let to dry completely. The samples were analyzed using JEOL JEM 2100 transmission electron microscope, operating at a maximum accelerating voltage of 250 kV.

Robustness of AuNCs fluorescence against changes in environmental conditions (pH and enzymatic activity) has been tested. The emission at maximum wavelength was recorded upon excitation at 368 nm for the as prepared AuNCs and after pH change. On the other hand, AuNCs in PBS (pH 7.4, 5 mg/mL) were mixed with different concentrations of trypsin solutions at 500 rpm and 37° C for 15h. Fluorescence was recorded before and after reaction with trypsin.

3.3.7. XPS analysis

Samples' pH was adjusted to 7, freeze dried and then analysed using a KAlpha+ spectrometer (ThermoFisher Scientific, East Grinstead, United Kingdom) equipped with a microfocused, monochromated Al K α X-ray source (400 μ m spot size). The charge compensation system was applied using electrons of 8 eV energy and low-energy argon ions to prevent any localized charge build-up. The electrons' kinetic

energy was measured by a 180° hemispherical energy analyzer in the constant analyzer energy mode (CAE) at 50 eV pass energy. Data acquisition and processing using the Thermo Advantage software is described elsewhere (42). The Scofield sensitivity factors were applied for quantification (43). All spectra were referenced to the C 1s peak at 285.0 eV binding energy (C–C, C–H).

3.3.8. Preparation and characterization of AuNCs-modified GNPs

They were fabricated using two step desolvation method and crosslinking. For the first precipitation, methanol was added to the AuNCs-modified gelatin and shaken to precipitate the high molecular weight fractions and the turbid supernatant was discarded. The gel-like mass of gelatin has been freeze-dried, weighed and dissolved in water at 50 °C giving rise to 2% w/v solution. The pH of gelatin solution was adjusted to 8 using 1N NaOH and methanol was added dropwise while stirring until the first turbidity was observed indicating the formation of NPs. They were further crosslinked using a mixture of EDC/NHS that was added dropwise. The NPs dispersion was kept under stirring at 600 rpm for 18h. They were purified by centrifugation (Thermo Fisher Scientific, Osterode am Harz, Germany) at 20,000 g for 1h at 20 °C followed by washing that was repeated 3 times. Following, the NPs dispersion was freeze-dried using 3% w/v trehalose as a cryoprotectant to be further used for other experiments. Dynamic light scattering (DLS) measurements: Size and zeta potential of the as-prepared nanoparticles were detected by Zetasizer (Nano ZS, Malvern Instruments Ltd, Malvern, UK) after appropriate dilution.

3.3.9. Cell culture

Human keratinocytes cell line (HaCaT) has been cultured in Dulbecco's Modified Eagle's Medium (DMEM) (Gibco®, Thermo Fischer Scientific, Paisley, United Kingdom) supplemented with 10% fetal calf serum and 100 U/ml penicillin–streptomycin. The cells were incubated at 37 °C under 5% CO₂. Cytotoxicity of the selected Ag-Au alloy NCs (AuAgS)-modified GNPs has been tested using MTT assay for cell viability. Cytotoxicity test. HaCat cells were cultured in Dulbecco's modified Eagle's medium supplemented with penicillin and streptomycin (100 U/mL) and 10 % v/v fetal bovine serum. They were seeded in a 96-well microplate (10,000 cells/well)

and maintained in 5 % CO₂ humidified incubator at 37 °C for 3 days. Then the medium was replaced with fresh medium containing AuAgS-GNPs (200 µL, 25-800 µg/ml). They were incubated with careful shaking for 24 h at 37 °C. MTT assay was carried out for the samples against negative control (treated with medium) and positive control (treated with 2% triton-X). Media have been removed and the cells were washed with Hank's Balanced Salt Solution buffer (HBSS) and incubated with 3-(4,5-Dimethyl-2-thiazolyl)-2,5-diphenyl-2H-tetrazolium bromide (MTT reagent) for 4 h, followed by DMSO treatment. The absorbance of the formed formazan solution (OD) was measured at 550 nm using microplate reader and the cell viability % has been calculated.

$$\text{Cell viability \%} = \frac{(\text{Sample OD} - \text{positive control OD})}{(\text{negative control OD} - \text{positive control OD})} \times 100$$

3.3.10. Bioimaging of GNPs with skin tissue

Excised human skin was obtained from abdominal plastic surgeries after the approval of the Research Ethic Committee of Saarland, Germany (Ärztchamber des Saarlandes, Dec. 2008) and permission of the volunteers. For skin preparation, the subcutaneous fatty tissue was removed and the skin surface has been cleaned by water. Skin samples were kept in aluminum foils and stored in -20°C to be used within no more than 6 months. For the imaging experiment, skin punches of 12 mm diameter have been cut and thawed and the surface was cleaned with water.

Untreated human skin samples and AuAgS-modified GNPs were separately scanned for their emission spectrum in the range 600 - 740 nm by confocal microscopy using lambda mode upon excitation at 405 nm. The treated skin samples have been tested applying the same parameters. Two groups of skin samples were treated with AuAgS-modified GNPs; a) by addition of NPs to skin surface and b) by insertion of AuAgS-modified GNPs-loaded microneedles into skin. For the surface treatment, 20 µL of AuAgS-modified GNPs (3 mg/mL) was pipetted over the surface of the skin punch. For the microneedles (MNs) treatment, dissolving polyvinyl alcohol (PVA)/sucrose microneedles patch (1x1 cm) loaded with NPs was applied to skin and the lodged MNs were imaged within skin. The skin was kept moistened by placing it over a wet filter paper in a circular chamber to prevent skin drying during examination and avoid

pressure application over the skin surface as described earlier by Stracke *et al* (44). The skin punch has been fixed on a microscopic slide with the skin surface facing upward that was covered by a cover slip to be examined by CLSM. A scheme of the experimental setup is shown in Figure S1 (Annex section).

Using the linear unmixing algorithm available in the Zen Black© software, the fluorescence signal of the NPs were separated from that of skin. For depth profiling, objectives (LCI Plan-Neofluar 25x/0.8 Imm Korr DIC M27 and EC Plan-Neofluar 10x/0.3 M27) have been used and z-stacks have been recorded with 5 and 10 μm steps for the surface and microneedles applications, respectively, and 3D images have been constructed.

3.4. Results and Discussion

3.4.1. Synthesis of gelatin-stabilized AuNCs

Gelatin is a natural polymer, which consists of a mixture of proteins and polypeptides resulting from the hydrolysis of collagen. We used gelatin type B to sequester and reduce Au (III) to Au (0), which combine together to form AuNCs emitting fluorescence at λ_{max} 640 nm. Different gold concentrations and pH values were tested to optimize the synthesis process. The fluorescence intensity increased with Au concentration up to 5 mM, while further increase in concentration resulted in gradual loss of fluorescence (Figure 1A, Figure S2 (Annex section)). The latter can be attributed to the formation of quenching larger gold nanoparticles, which affect the fluorescence negatively (45). At a concentration of 30 mM gold chloride, only gold nanoparticles have been produced as observed by TEM (Figure S3A (Annex section)). On the other hand, pH adjustment was essential to initiate the reaction between gold and gelatin. At pH range (7-12), the fluorescence increased with pH to be maximized at pH 12 (Figure 1B). Among the amino acids composing gelatin, the basic amino acids; arginine (8%) (46) and lysine (4%) (46), have the ability to reduce Au (III) ions to Au (0) by electron transfer from the side chain amines. According to Xu *et al*, arginine and lysine can form complexes with Au (III) that can be further reduced by tyrosine under alkaline conditions (38), but tyrosine represents only <0.5% of gelatin weight (46). On the other hand, glutamic acid (10%) (46) may contribute to the thermal reduction of gold ions (47). All these mechanisms can variably contribute to the formation of AuNCs.

3. NIR-emitting gold nanoclusters-modified gelatin nanoparticles as a bioimaging agent in tissue

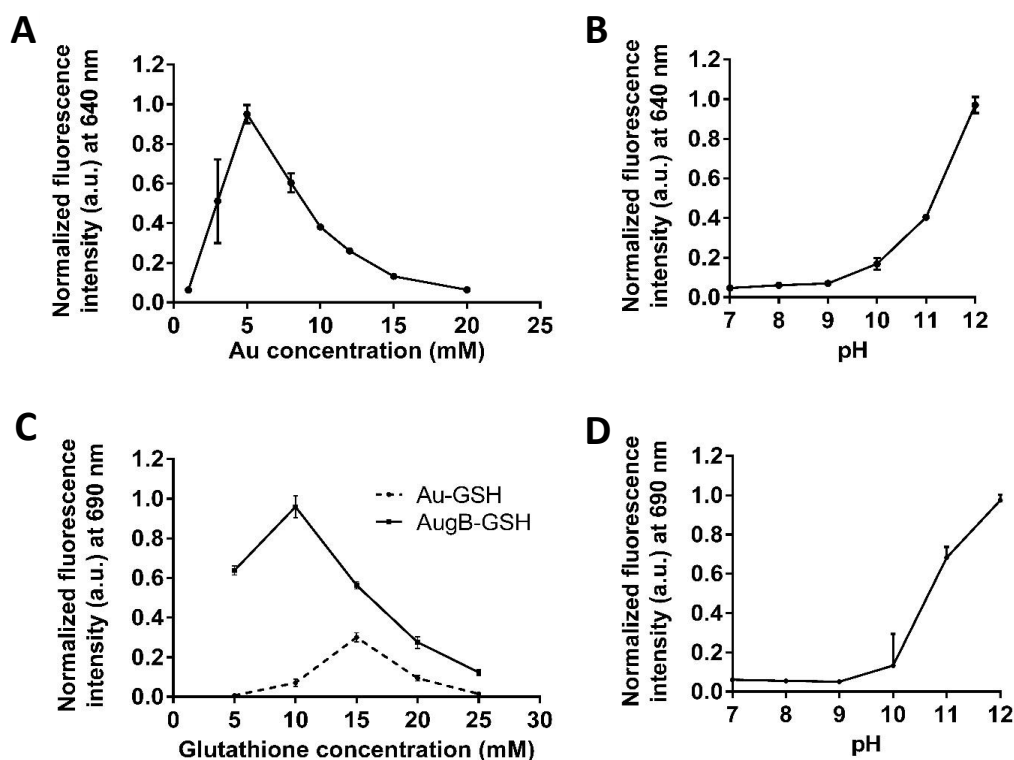


Figure 1. Gold nanoclusters stabilized by gelatin only; A) Effect of gold molar concentration and B) Effect of pH on the maximum emission fluorescence at 640 nm. Gold nanoclusters stabilized by gelatin and glutathione (GSH); C) Effect of GSH concentration on the fluorescence of AuNCs at 690 nm, when used alone (Au-GSH) and in combination with gelatin (AugB-GSH) and D) Effect of pH on the maximum emission of the gelatin-GSH-stabilized AuNC fluorescence at 690 nm. AugB-GSH describes nanoclusters stabilized using gelatin and different concentrations of glutathione. Au-GSH is the clusters stabilized with different concentrations of glutathione only without using gelatin. For all experiments; mean \pm SD, $n=3$.

The polymer backbone structure and viscosity play a role in controlling the growth rate and the stabilization of AuNCs. Compared to gelatin A, gelatin B showed better efficiency in forming fluorescent AuNCs (Figure S4A (Annex section)). This can be due to the content of glutamic acid in gelatin B, which results by the alkaline hydrolysis of collagen (48). In addition, gelatin B is expected to have more free amines due to the lower isoelectric point (4-6) compared with 7-9 in gelatin A (49). On the other hand, higher bloom of gelatin B (225 g) resulted in less fluorescence compared to bloom 75 g (Figure S4B (Annex section)), which might be due to the higher flexibility of short polymer chains to interact with gold ions. Although the viscosity contributes to the

stability of AuNCs, the excessively increased viscosity may reduce the electron transfer to Au ions, resulting in lower rate of reduction (50). For up-scaling the AuNCs production, multiples of gelatin concentrations have been tested while multiplying the Au concentration to keep the ratio unchanged (Figure S5 (Annex section)).

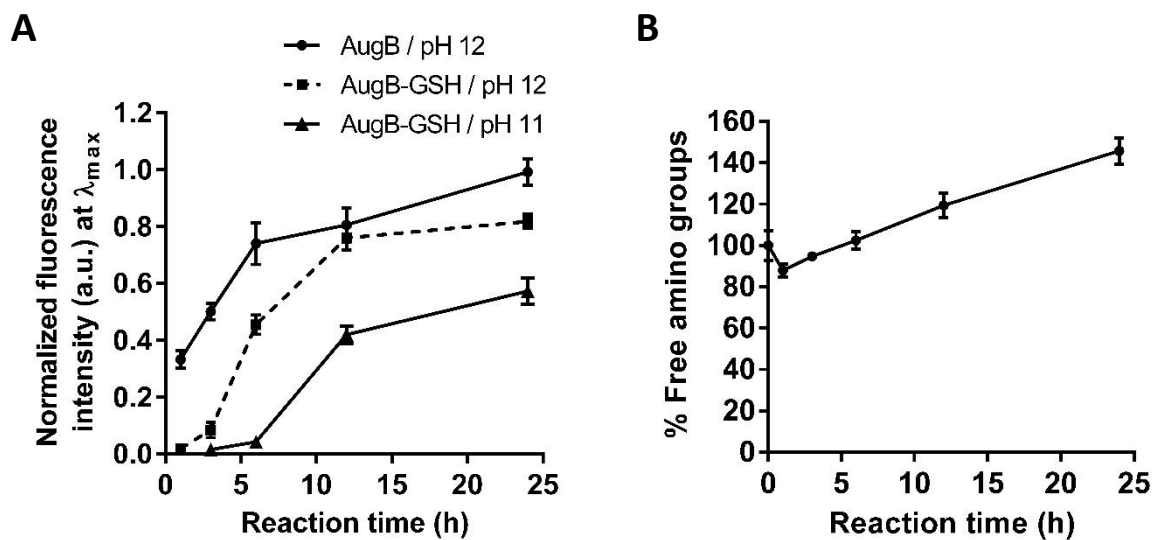


Figure 2. A) Effect of GSH addition and the change of pH on the reaction rate for the formation of gelatin-stabilized AuNCs, represented by fluorescence intensity (mean \pm SD, n=3). The different reaction conditions; 4% w/v gelatin at pH 12 (AugB / pH 12), 4% w/v gelatin and 10 mM GSH at pH 12 (AugB-GSH / pH 12) and 4% w/v gelatin and 10 mM GSH at pH 11 (AugB-GSH / pH 11), B) Quantification of the free amine groups of gelatin after different reaction times with gold chloride at pH 12 (AugB / pH 12) using ninhydrin test (mean \pm SD, n=3). AugB represents nanoclusters stabilized by gelatine at different pH and reaction time.

Glutathione (GSH) is an effective reducing agent commonly used to prepare AuNCs due to the presence of thiol group. One-pot synthesis of AuNCs using gelatin and various glutathione concentrations allowed to tune the emission spectrum of the nanoclusters (Figure S6 (Annex section)). The selected 10 mM GSH concentration resulted in 50 nm red-shift in the AuNCs fluorescence ($\lambda_{em} = 690$ nm). Interestingly, under the tested reaction conditions, GSH alone, with the same concentration, was not capable of forming fluorescent AuNCs. Only GSH of 15 mM concentration resulted in

detectable fluorescence when reacted with gold chloride, which was even enhanced by the addition of gelatin (Figure 1C). This proves that gelatin and GSH have a synergistic contribution to the formation of AuNCs. Ligand modification and thus the introduction of more electron-rich functional groups, can manipulate the electron transfer to the metal core, and consequently influence the fluorescent properties of AuNCs (16). Furthermore, increasing the pH from 7 to 12 resulted in gradual increase in fluorescence (Figure 1D).

3.4.2. Structure integrity of gelatin during AuNCs formation

To further use the gelatin for pharmaceutical applications, a compromise between the AuNCs formation and maintaining the polymer integrity is necessary. Controlling the pH has the ability to manipulate the reaction rate (Figure 2A). At the same time, it affects the gelatin structure particularly at high temperatures. At pH 12 and after 6h of the reaction with gold ions, gelatin has lost its gelling properties upon cooling to 4 °C. Conversely, pH 11 preserves the polymer's gelation capabilities till reaction is completed after 24h (Figure S7 (Annex section)). In order to further investigate the gelatin structure, ninhydrin test was performed to quantify the free amine groups at different time intervals of the interaction with gold. After 1h of reaction at pH 12, the free amino groups were reduced to 87% and this can be attributed to the coordination established between $-NH_2$ and Au. The percentage increased to 94 after 3h, continuing gradually to hit 145% after 24h of the reaction, suggesting gelatin degradation and hence the rise of free amine groups of the polypeptide (Figure 2B).

Two AuNCs formulations have been selected, so far, for further studies: AuNCs synthesized by gelatin at pH 12 and 3h of reaction and the other formulation was prepared by gelatin and GSH at pH 11 for 24h (AuS) (Table S1). These formulations showed well detectable fluorescence by confocal microscopy upon excitation at 405 nm (Figure S8B (Annex section)). They have been examined as well by FT-IR and MALDI-TOF MS to show differences in gelatin structure as opposed to untreated polymer. MALDI-TOF MS is a common tool for studying the core size of AuNCs and composition of ligand. Nonetheless, calculating the AuNCs core size by detecting the number of gold atoms in such a case was not an accessible option due to the

3. NIR-emitting gold nanoclusters-modified gelatin nanoparticles as a bioimaging agent in tissue

heterogeneous mass of the gelatin polypeptides mixture, in addition to the potential fragmentation of the nanoclusters during ionization (27, 51). In parallel, the examination of the change in the mass spectrum of gelatin could be determined. Figure 3A shows the mass spectra of gelatin and both formulations of the nanocluster: Aug and AuS. Peaks of lower molecular weight ($m/z \approx 3100$) appear in both Aug and AuS. The two spectra display different regions of approximately the same m/z ratio as the untreated gelatin, with variable peak intensities. Using the stated conditions for Aug and AuS synthesis, controlled gelatin degradation while retaining the gelling properties was confirmed as has been observed earlier (Figure S7 (Annex section)).

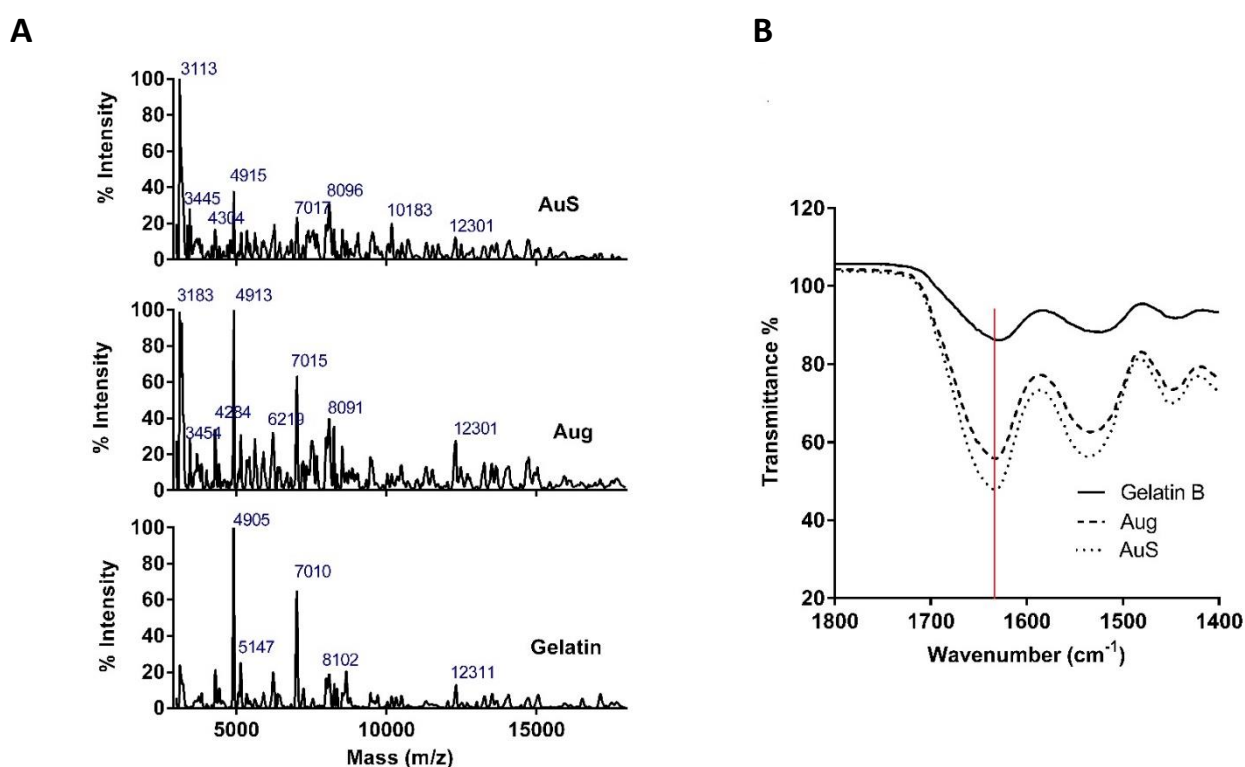


Figure 3. Investigating the effect of AuNCs on the gelatin structure by comparing AuS and Aug to untreated gelatin A) MALDI-TOF MS spectra recorded in the positive modes show areas of similar mass (m/z), B) FT-IR spectra showed a negligible shift in amide I from 1629 cm^{-1} for gelatin to 1632 cm^{-1} in both Aug and AuS indicating β -sheets secondary structure ($1623 - 1641\text{ cm}^{-1}$) for all of them. Aug is the optimized formulation of gelatin-stabilized nanoclusters with reaction time of 3h / pH 12. AuS represents the optimized formulation using gelatin and glutathione with reaction time of 24h / pH 11.

On the other hand, FT-IR is commonly used to investigate the conformational changes of proteins and peptides, particularly in the secondary structure. Amide I (1600 – 1700 cm^{-1} , mainly due to CO stretching vibration) and amide II ($\approx 1550 \text{ cm}^{-1}$, NH bending and CN stretching vibration) are characteristic bands for the secondary structure. However, it is less straightforward to correlate the secondary structure to amide II than amide I (52). Untreated gelatin showed amide I band at 1629 cm^{-1} (Figure 3B) revealing β -sheets secondary structure (indicated by amide I in the range 1623 – 1641 cm^{-1}) (52). A very small shift to 1632 cm^{-1} after the reaction with gold (in Aug and AuS) indicates no or minimal changes in the secondary structure. By controlling the pH and the reaction time, we managed to preserve the structural and conformational integrity of gelatin, to be further used for NPs fabrication.

3.4.3. Fluorescence enhancement

Enhancing the fluorescence will be crucial for different bioimaging purposes, particularly in tissues. One strategy to enhance the fluorescence intensity is the formation of alloy nanoclusters, by doping another noble metal during the nanoclusters growth. Silver and gold have been considered as a common combination for fabrication of alloy nanoclusters (53, 54). Modification of gold nanoclusters by silver has been reported to enhance the emission (53, 55). It was important to optimize the Ag : Au molar ratio (0.4) to obtain the highest possible fluorescence intensity, while using gelatin and GSH as ligands (Figure S9 (Annex section)). Surprisingly, doping of Ag ions after 6 h from the start of the reaction resulted in 2.5 fold increase in fluorescence rather than addition at the start of the reaction (Figure S9 (Annex section)). This might indicate the significance of the different arrangements of noble atoms in the core to control the fluorescence properties of the alloy nanoclusters. In another strategy, we investigated the addition of Ag ions after the reaction of AuS formulation was completed. Adjustments of the Ag: Au molar ratio, pH and reaction time were considered to maximize the intensity of the fluorescence (Figure S10 (Annex section)). Eventually, two Ag-modified formulations; alloy AuNCs (AuAgS) and post-synthesis Ag-modified AuS (AuS+Ag) as shown in table S1 were selected for further characterization in comparison to Aug and AuS. TEM images and measured size

3. NIR-emitting gold nanoclusters-modified gelatin nanoparticles as a bioimaging agent in tissue

distributions are shown in Figures S11 and S8 (Annex section) of silver-modified and pure gold nanoclusters, respectively.

Figure 4A shows the 3D emission spectra of the four selected formulations. All samples showed broad emission spectra. Red-shift in the fluorescence maximum wavelength was observed due to the co-stabilization with GSH and enhancement of fluorescence was achieved upon the modification of nanoclusters using Ag.

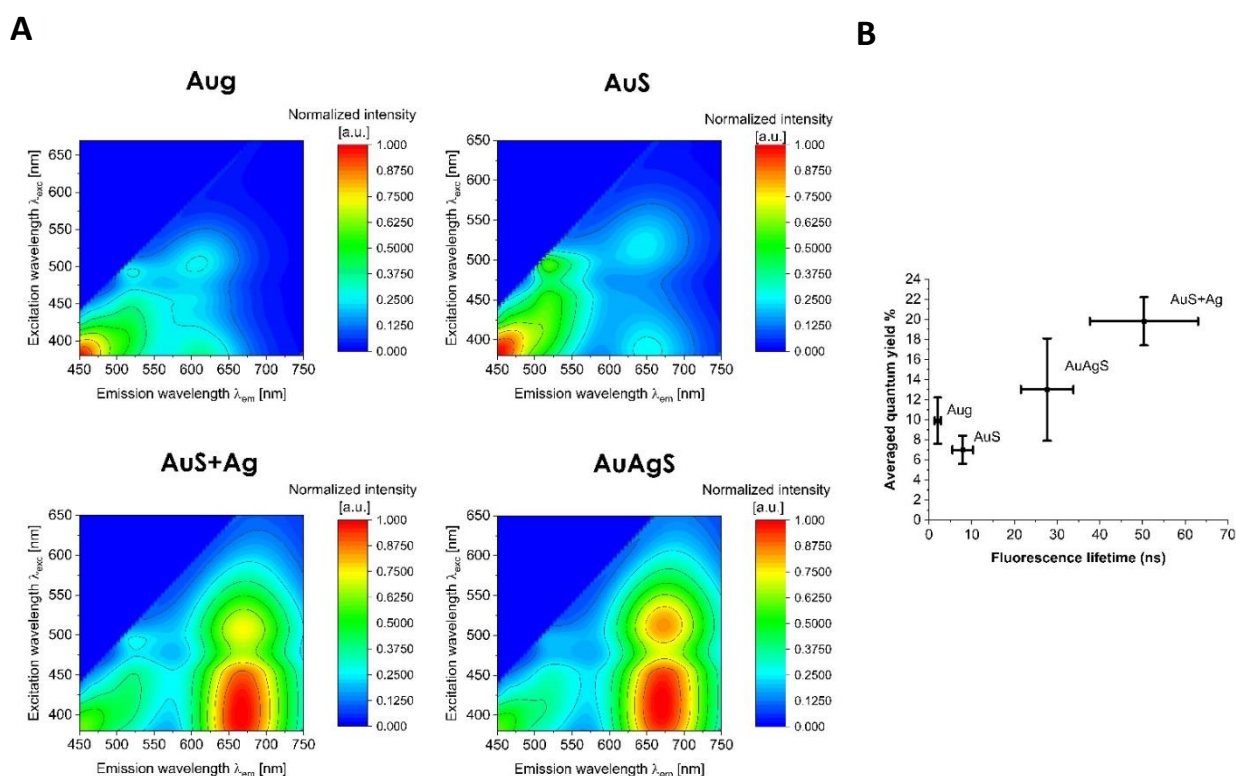


Figure 4. Optical properties of different AuNCs; Aug, AuS, AuAgS and AuS+Ag, A) 3D emission spectra at excitation wavelength range 380-650 nm and the emission was recorded from 450 to 750 nm, B) Averaged lifetime (measured upon excitation at 470 nm) correlation to averaged absolute quantum yield % (measured upon excitation at 400-550 nm with 5 nm steps). The fluorescence around 450-550 nm is due to the gelatin autofluorescence.

Both alloy nanoclusters formation and post-synthesis modification by Ag resulted in enhanced broad red emission bands upon excitation at 380-550 nm. This offers a variety for the nanoclusters application for bioimaging over a wide range of fluorescence imaging settings. Absolute quantum yields (QY) were measured using

integrating sphere setup at different excitation wavelengths (400-550 nm) and were corrected for the blue fluorescence of gelatin (Figure S12A (Annex section)). Modification with Ag resulted in an approximate 3-fold increase in the QY upon excitation at 400 nm compared to AuS. The measurements revealed that Ag-modified AuNCs have an excitation wavelength-dependent QY and this behavior is more pronounced in AuAgS. They showed maximum QY at 400 nm (24 %) that declined to reach the value of AuS (~ 9%) at 500–550 nm (Figure S12 (Annex section)). Nevertheless, modification by Ag resulted in lower rate of fluorescence decay when excited at 470 nm (Figure S12B (Annex section)). Interestingly, it turns out that the enhancement of QY after the addition of Ag is correlated with an extended fluorescence lifetime, as summarized in figure 4B.

3.4.4. Structure - fluorescence stability relationship

Examination of the different AuNCs by XPS provided valuable insight on the oxidation state of the metal elements providing information about the core-shell structure of the nanoclusters. This opens the venue for a better understanding of the nanoclusters formation and further correlation to their optical properties and photostability. Starting with Aug, Au 4f doublet can be deconvoluted into 3 distinct components with Au 4f_{7/2} at 84.3, 85.3 and 87.6 eV referring to Au (0), Au (I) and Au (III), respectively (56) (Figure 5). So, after 3h of reaction with gelatin at 60 °C under alkaline conditions, Au (III) has been reduced partially to Au (I) and Au (0) to form AuNCs. However, Au (III)-protein complex has been assigned recently by Dixon and Egusa to also contribute to the fluorescence (57). By virtue to the electron-donating groups in gelatin, Au (I) as an intermediate reduced state of gold has been produced, with a further reduction to Au (0). The aggregation of Au (0) results in the formation of a metal core with Au (I) on the surface as the nanoclusters' shell as a typical structure defined in literature (11, 27, 58). After 24h of reaction, all Au (III) has been totally reduced to Au (I) and Au (0) (Figure 5A). On the other hand, co-reduction with GSH resulted in complete reduction to Au (0) forming two populations of AuNCs of different core sizes with Au 4f_{7/2} peaks of Au (0) at 83.9 and 84.6 eV (Figure 5B). As reported earlier, the higher binding energy of Au (0) indicates an increase in the core size (27). Addition of Ag ions after the formation of AuS resulted in no change in the Au oxidation state with Au (0) peaks at

84.2 and 84.9 eV. Possibly, Ag ions are further reduced by the ligands and incorporated in or replaced some of the Au atoms at the surface of the nanoclusters. Another technique such as X-ray powder diffraction (XRD) (55) is required to confirm the atoms arrangement within the clusters, but this was not possible due to the very minute amount of Ag and Au compared to the gelatin in the current formulations matrix. Similarly, complete reduction of Au was observed with the formation of alloy NCs (AuAgS), but interestingly with homogenous-sized population of AuNCs (Au 4f7/2 showed one peak at 84.5 eV) (Figure 5B). However, we cannot provide any evidence of Ag reduction particularly with the difficulty to distinguish between Ag 3d5/2 corresponding to Ag (0) and Ag (I) without Auger lines analysis, which was hampered by the very low concentration of Ag (Figure S13 (Annex section)); almost the detection limit. Co-reduction with GSH showed S 2p doublet with S 2p3/2 at 161.8 eV (S-Au; S-Ag if present) (59), 163.8 eV (S-H), 166.2 eV (oxidized sulfur: S (IV)) and 168.6 eV (oxidized sulfur: S (VI) (60) (Figure 5C) with very weak concentrations of 0.02, 0.03, 0.09 and 0.05 at % in AuAgS, respectively. A potential Au-S bond may be formed; however data must be taken with caution due to the very low concentration of these elements compared to the bulk of the sample which constitutes out of gelatin, and the detection limit of the method. But on the other hand, the concentrations of Au and Ag were found within the same range with values of 0.02 and 0.01 atomic % respectively, which supports the assumption of formed Au-S and eventually Ag-S bonds.

The structure of AuNCs together with the ligand plays the major role in controlling their optical properties due to the transfer of electrons between the ligand and the metal surface and within the metal core. On the other hand, ligands as capping agents control the fluorescence stability of AuNCs in response to the different environmental conditions. In comparison to the original synthesis environment, testing the robustness of AuNCs fluorescence over a pH range (1.5 - 7), showed different degrees of stability arranged in the following order $\text{AuG} < \text{AuS} < \text{AuAgS} < \text{AuS+Ag}$ (Figure 6A). However, all AuNCs showed considerable fluorescence stability at physiological pH; modifications with GSH and Ag have widened the pH stability range down to acidic conditions. Possessing the capability to manipulate the pH-response of AuNCs provides the opportunity for various applications. For instance, the pH-responsiveness

3. NIR-emitting gold nanoclusters-modified gelatin nanoparticles as a bioimaging agent in tissue

showed by Aug could be applied as a bioprobe to monitor pH changes in cancer cells (61).

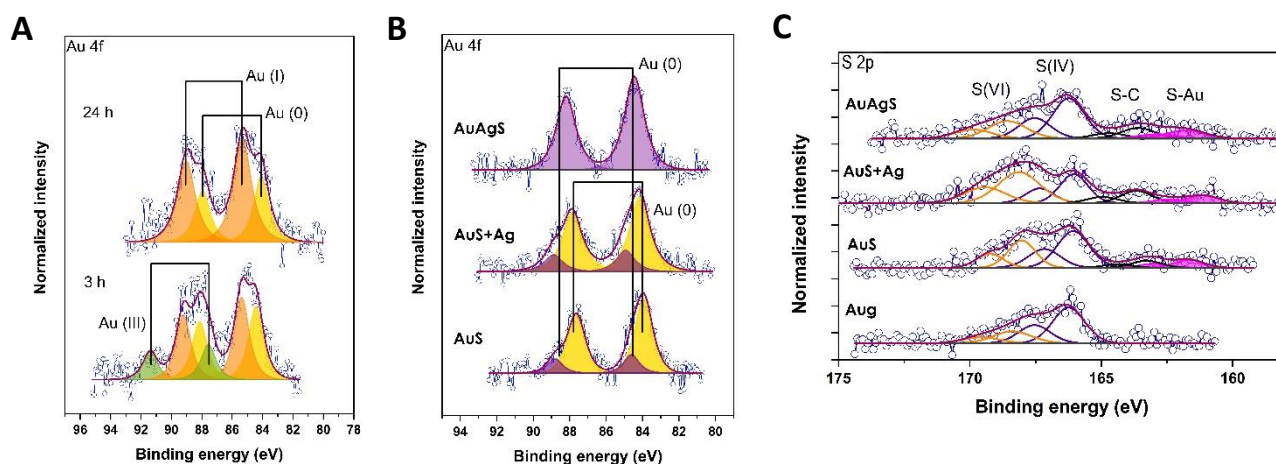


Figure 5. XPS spectra: A) Au 4f of AuNCs stabilized by gelatin at different reaction times (3 and 24h), B) Au 4f of AuNCs stabilized by gelatin and glutathione (AuS, AuS+Ag and AuAgS from lower to upper panel). Yellow curve: Au (0) at 84.1 ± 0.2 eV, Purple curve: Au (0) at 84.7 ± 0.2 eV, Orange: Au (I) at 85.5 ± 0.2 eV, Green: Au (III), C) S $2p_{3/2}$ of different AuNCs (Aug, AuS, AuS+Ag and AuAgS from lower to upper panel). Magenta-filled: 161.8 eV (S-Au; S-Ag if present), Black: 163.8 eV (S-H), Violet: 166.3 eV (oxidized sulfur: S (IV)), Orange: 168.6 eV (oxidized sulfur: S (VI)).

To investigate the contribution of gelatin and GSH in stabilizing AuNCs, a trypsin experiment has been performed. Trypsin specifically works by hydrolyzing the peptide bonds on the carboxylic terminal of lysines and arginines. The degree of hydrolysis varies depending on the trypsin concentration and the amino acid sequence of the protein (62). In case of Aug, gelatin is the main reducing and capping agent of AuNCs. Gelatin fragmentation by trypsin resulted in decrease of the fluorescence that was trypsin-concentration dependent as shown in figure 6C. When the polypeptide loses the integrity of its structure, which was responsible for holding the gold atoms and ions together, they dissociate and the fluorescence diminishes as observed at trypsin activity of 3.2×10^3 U/mg of gelatin. Interestingly, AuS fluorescence showed much higher stability to trypsin digestion. It can be envisaged that even after gelatin digestion, the AuNCs structure is still preserved by binding to the thiolate groups of GSH and fractions of degraded gelatin. This provides valuable information regarding the role of

both gelatin and GSH in AuNCs protection. When AuAgS showed intermediate stability to gelatin, AuS+Ag demonstrated ultimate stability (Figure 6B). The latter even showed a slight increase in the fluorescence, probably due to the adsorption of trypsin to the AuNCs (63-65). This formulation will be interesting for long-term imaging of AuNCs in tissues due to their stability independent of the integrity of gelatin as a capping agent. On the other hand, AuAgS would be beneficial for mechanistic studies, especially when formulated as GNPs. Their bright fluorescence together with their intermediate sensitivity to polymer degradation will be a beneficial option to smartly track the NPs and follow their fate in tissues. In conclude, NCs can offer stimuli-responsive fluorescence i.e. smart probes (different response to pH, enzymatic degradation, etc), which can be controlled by manipulating the composition of NCs and ligands. This is an advantage of such imaging probes over regular dyes, where different stimuli-responsiveness require careful selection of more than one dye to perform the same functions.

From the knowledge gained throughout the characterization of the different AuNCs' optical properties and XPS studies implemented in this research work, together with literature knowledge on the general structure of gold nanoclusters (11, 13, 58), simplified models for the nanoclusters were proposed as shown in figure 6C. Aug, where nanoclusters are produced only using gelatin, is considered to be the parent formulation, which is further modified into other formulations with different properties. These clusters exhibited a typical core-shell structure composed of Au (0) and Au (I) protected by gelatin as the only ligand. Further, the introduction of GSH resulted in complete reduction of Au (III) to Au (0) and nanoclusters formation of two different sizes. In addition, stabilization by GSH offered greater protection of the nanoclusters fluorescence against pH change and enzymatic degradation. Addition of Ag ions after or during the synthesis of AuS resulted in increased fluorescence intensity, QY, lifetime, and stability. Addition of Ag after the synthesis of AuS (AuS+Ag) led to no changes in the oxidation state of Au and some incorporation of Ag into the nanoclusters surface. On the other hand, addition of Ag ions during the synthesis process of AuS appears to lead to the formation of smaller alloy nanoclusters (AuAgS) but of homogenous size.

3. NIR-emitting gold nanoclusters-modified gelatin nanoparticles as a bioimaging agent in tissue

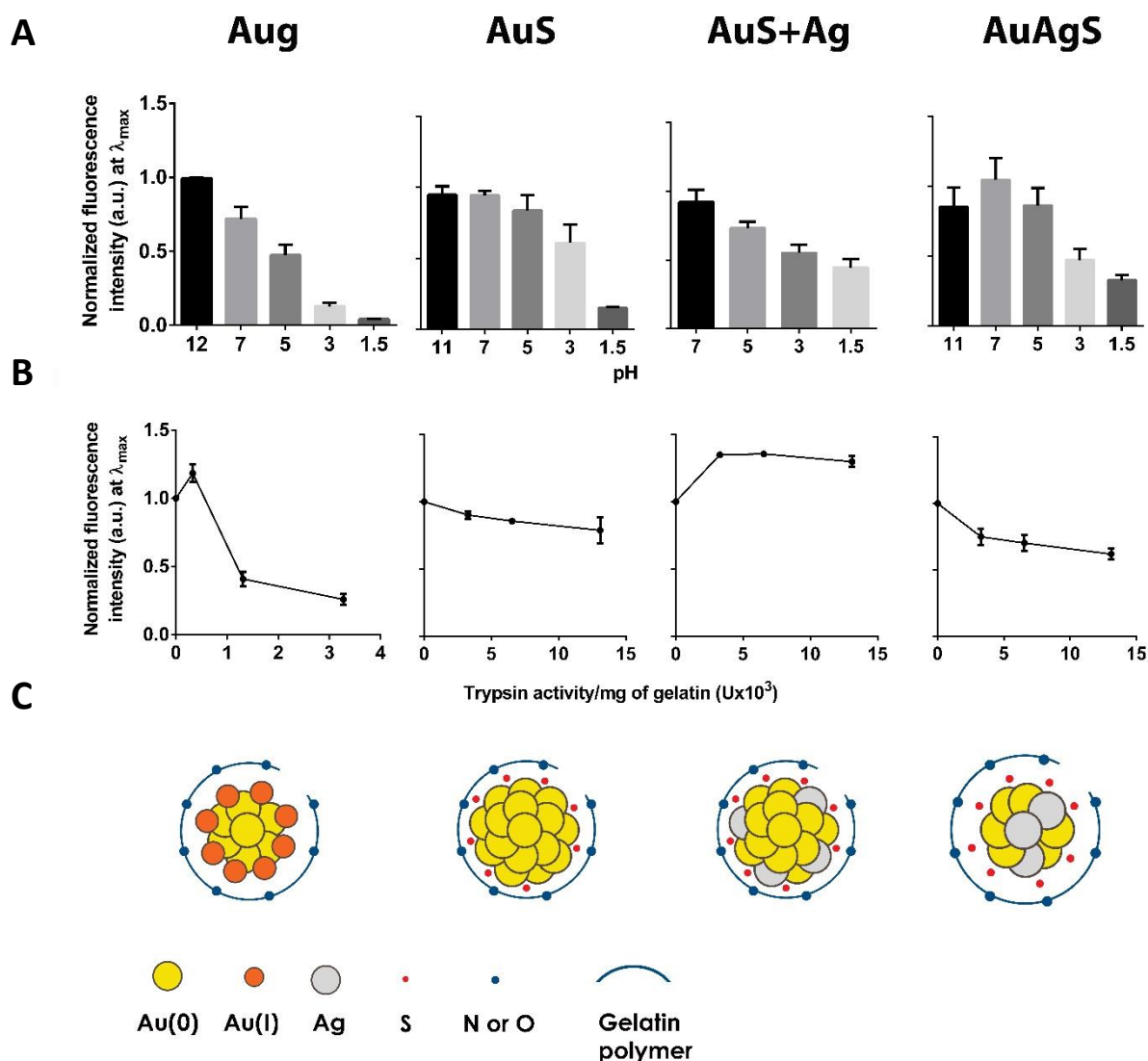


Figure 6. Fluorescence stability of different AuNCs to; A) pH changes by changing the pH from that of synthesis to lower pH values (1.5 -7) (mean \pm SD, n=3), B) gelatin digestion using different concentrations of trypsin at pH 7.4, 37 °C for 15h. Fluorescence intensity was recorded at λ_{max} for the different AuNCs (640 nm for Aug, 690 nm for AuS and 700 nm for both AuS+Ag and AuAgS) (mean \pm SD, n=3). This shows the effect of GSH and Ag ion addition on enhancing the AuNCs fluorescence stability against pH changes and trypsinisation C) Simplified proposed models for AuNCs structure based on XPS data. Aug: showed a typical core-shell structure of Au (0) and Au (I) respectively. For all others GSH-modified AuNCs, Au (0) was the only oxidation state with Au-S bonding. The AuNCs have different core size (the biggest; AuS and the smallest AuAgS) referring to the Au (0) binding energy of 83.9 and 84.5 eV, respectively.

3.4.5. Formation of protein nanoparticles using AuNCs-modified gelatin

Such NPs were prepared from AuNCs-modified gelatin, using two-step desolvation method. Desolvation is the dehydration of gelatin by adding an antisolvent, which results in coiling of the polypeptide chains. The first desolvation step was to separate the gelatin fractions of high molecular weight (HMW). Discarding the low molecular weight fractions (LMW) of gelatin will improve the homogeneity of the NPs size and prevent irreversible aggregation (66). The redissolved HMW gelatin was again desolved to form NPs that were further cross-linked to preserve their conformation in aqueous environment. Various parameters have been optimized such as the antisolvent, the pH of gelatin solution and the crosslinking agent.

NPs formation is a complex phenomenon controlled by the polymer-antisolvent-solvent system. The antisolvent's diffusion and affinity to solvent and the polymer-solvent interactions influence the particle size (67). Of the various organic solvents (acetone, acetonitrile, isopropanol, ethanol) only methanol was suitable for the formation of AuNCs-modified GNPs. At the first desolvation step, the pH of gelatin solution was adjusted to 7 to balance between preserving the fluorescence of AuAgS and reducing the gelatin charge to induce precipitation, while at the second desolvation, the pH was adjusted to 8 to prevent aggregation of the NPs. For crosslinking, glutaraldehyde, which is a common crosslinker for GNPs, resulted in complete loss of the Aug-modified GNPs fluorescence, which comes in agreement with a previous report by Khandelia *et al.* (68). This can be attributed to the crosslinking mechanism of glutaraldehyde which is a non-zero length crosslinker that connects the alpha-amino groups of lysine residues (69). As a result, another crosslinker has been applied to preserve the fluorescence. This was a mixture of N-(3-Dimethylaminopropyl)-N'-ethylcarbodiimide hydrochloride (EDC) and N-Hydroxysuccinimide (NHS); a zero-length crosslinking agent that couples carboxylic to primary amine groups (70).

Nanoparticles of narrow particle size distribution have been produced using Aug, AuS (Figure S14 (Annex section)) and AuAgS-modified gelatin (Figure 7A). TEM showed that the NPs are spherical in shape and non-aggregated and revealed the internal distribution of the AuNCs. Among them, AuAgS-GNPs were of interest for further

3. NIR-emitting gold nanoclusters-modified gelatin nanoparticles as a bioimaging agent in tissue

studies with Z-average size of 218.8 ± 1.7 nm and a size distribution represented by the polydispersity index (PDI) of 0.073 ± 0.016 . They showed high colloidal stability and further freeze drying with trehalose had no effect on the particle size following redispersion. The NPs formation retained the fluorescence emission spectrum of AuAgS (Figure 7B). Absolute QY was measured ($\lambda_{\text{max}} = 400 - 550$ nm) and corrected for the NPs scattering using a reference of similar plain GNPs. They showed an average QY of 14.8 ± 0.8 % which was independent of the excitation wavelength, in contrast to the free nanoclusters. However, the formation of NPs have not changed the fluorescence lifetime behaviour, as AuAgS-GNPs showed higher fluorescence lifetime compared to AuAg and AuS-GNPs (Figure S16 (Annex section)).

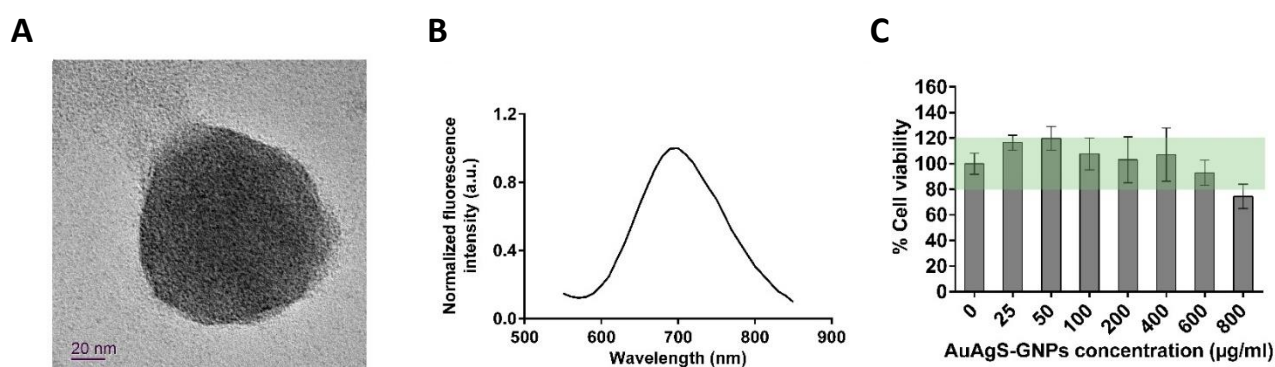


Figure 7. A) TEM image of AuAgS-GNPs with accelerating voltage 100 kV, B) Emission spectrum of the nanoparticles by excitation at 368 nm, C) Cytotoxicity testing of AuAgS-GNPs against human keratinocytes (HaCat cells) using different concentrations (25 - 800 µg/mL) by MTT assay (mean \pm SD, n=6). Green-shaded box indicates the range where no toxicity is concluded.

The cytotoxicity of AuAgS-GNPs has been tested against human keratinocytes (HaCat cell line) after 24h of incubation, using MTT assay, which assesses the cell metabolic activity. The NPs showed no cytotoxicity (≈ 100 % viability) at concentrations as high as 600 µg/mL (Figure 7C). This can be attributed to the biocompatibility of the materials used in the preparation including the non-toxic crosslinking agent (EDC). Concerns

over the reported toxicity of silver ions have been considered. Nevertheless, due to the very minute amount used in the formulation, and the possible complete reduction of Ag ions during the nanoclusters preparation, the formulation was biocompatible. Finally, the produced fluorescent GNPs are safe biomaterials that pave the way for various biological applications including drug delivery.

3.4.6. Tissue bioimaging based on linear unmixing

Imaging and tracking of NPs in tissue using confocal microscopy is a complex, even though beneficial process, which provides deeper knowledge about the efficiency and fate of nano-pharmaceuticals. In this regard, we have selected human skin to test the ability of our developed AuAgS-labelled GNPs to be imaged with tissue. Skin is regarded as a challenging tissue for imaging due to its density and auto-fluorescence that limits the process of suitable dyes selection. The capability of imaging nanoparticles with skin opens the avenue for better understanding of NPs behaviour in skin. This will be helpful for therapeutic purposes through transdermal drug delivery which gains a lot of attention recently to take over the invasive methods of drug delivery. On the other hand, occupational skin exposure to nanomaterials can be hazardous for human health, especially over a long term. Overall, the developed fluorescent GNPs can be further applied to different biological applications that can even extend from skin to other tissues.

There are many endogenous auto-fluorescent substances in skin that may interfere with the analysis of various fluorophores. This makes the choice of an appropriate fluorophore, with a distinct fluorescence from that of skin, not an easy option, especially with the broad emission spectrum of skin. Even with suitable dyes, offsetting the skin's fluorescence was the solution used by variant research groups for imaging of NPs in skin (71-74). However, the ability to image NPs together with skin structure will give visual evidence about the NPs penetration within the tissue. In this regard, others resort to either dual-channel imaging followed by subsequent images overlapping (75), or staining of skin prior to NPs examination (76). AuAgS-GNPs showed well-detected fluorescence in the red region of the spectrum (Figure 8A). This can be considered as the optimum properties of a fluorophore for imaging with skin. However, imaging of

both NPs and skin simultaneously will be a more descriptive and time-saving method of analysis.

Linear unmixing is a technique used to distinguish the signals of fluorophores of overlapping spectra. An algorithm is used to analyse each pixel and isolate the mixed fluorescence signals arising from multiple fluorophores into individual components accrediting to spectral reference fingerprints (77). AuAgS-GNPs showed a distinct fluorescence signal from that of skin (Figure 8A). Instead of canceling the skin fluorescence, linear unmixing was used to separate NPs from skin signal. To test the accuracy of the method, NPs have been added to the skin surface and imaged directly. Figure 8B shows ~ 200 μm depth profiling (z-stacks steps of 5 μm) of the NPs and skin, while 3D-constructed images are shown in Figure 8C. The images showed the NPs filling the furrows of the skin between the keratinocytes isles in a similar pattern to findings reported earlier by Stracke *et al.* (44). This indicates the applicability of the approach for accurately separating the signals, so penetration studies within the tissue can be further analysed.

Microneedles have been commonly used as a minimally invasive mechanical penetration method to deliver biotherapeutics through skin (78). The nanocarriers labelled with NCs were loaded in dissolving microneedles consisting of PVA/sucrose. After microneedles insertion in skin, linear unmixing showed the NPs distribution within the skin tissue with a depth profile of 760 μm (Figure 8D). So, spectral imaging with linear unmixing provide a time-saving, non-invasive and depth-revealing technique for simultaneous examination of the NPs and skin, which helps to avoid the artifacts produced during skin sectioning and staining. Finally, the developed AuNCs-modified GNPs showed to be an effective fluorescent probe for bioimaging with biological tissue such as skin. The developed nanoparticulate system with assistance of a minimally invasive technique such as microneedles application, will be further investigated for delivering antigen through skin for transcutaneous vaccination with the ability of simultaneous biomaging and particles tracking.

3. NIR-emitting gold nanoclusters-modified gelatin nanoparticles as a bioimaging agent in tissue

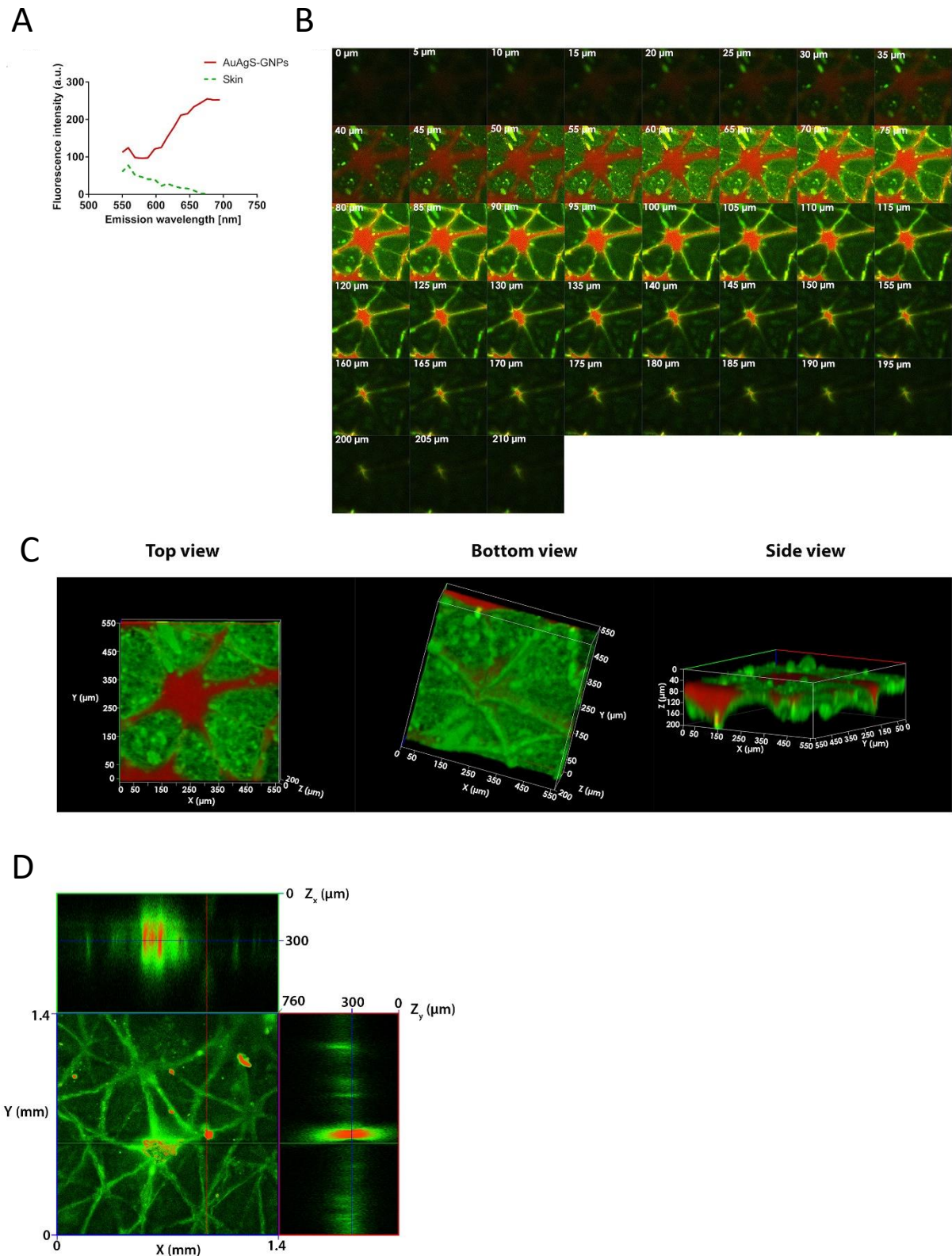


Figure 8. A) Emission spectra of skin and AuAgS-GNPs recorded by confocal microscopy at $\lambda_{\text{ex}} 405 \text{ nm}$, B), C) 3D confocal imaging of NPs applied to the skin surface; B) z-stacks starting from skin surface to 210 μm depth in tissue with 5 μm steps. This shows the NPs (red) filling

the furrows between the keratinocytes isles (green). The fluorescence channels were separated from the crude fluorescence using linear unmixing algorithm with reference to the fluorescence spectra of skin and NPs, C) 3D- images constructed from the z-stacks showing upper, lower and side view (from left to right) of the scanned area, D) 3D confocal imaging of NPs-loaded microneedles applied into skin, constructed from z-stacks recorded over 760 μm depth with 10 μm steps, showing the NPs (red) penetration depth (Z_x and Z_y) into skin tissue (green). The XY-plane shows a horizontal cut in skin at 300 μm depth showing the nanoparticles distribution.

3.5. Conclusion

We proved the effectiveness of gelatin to produce fluorescent AuNCs, introducing different methods for tuning the emission wavelength alongside with the fluorescence intensity. Gold ions reduction-assisted by GSH, in one-pot synthesis, induced 50 nm-red shift in the nanoclusters emission alongside with stabilization against pH changes and enzymatic degradation. Modification by Ag ions either by doping during or post the nanoclusters formation resulted in enhancement of the QY and fluorescence lifetime. Finally as a result, four different AuNCs have been produced, showing variant stability in response to pH and enzymatic degradation, so they can be acclaimed for various biological applications. The optical properties-structure relationship has been established with the aid of XPS analysis. Model-structures for the different 4 formulated AuNCs have been constructed, summarizing the effect of different modifications. On the other hand, optimization of the synthesis process resulted in preserving the gelatin structure integrity, to be further efficiently used for the preparation of GNPs. The NPs of size 218 nm showed distinct inner distribution of the AuNCs when examined by TEM. They preserved the fluorescence properties of the nanoclusters, thanks to the careful selection of the crosslinking agent (EDC/NHS). They showed biocompatibility toward human keratinocytes cell line up to 600 $\mu\text{g}/\text{mL}$, which acclaims them for further applications in drug delivery. They have been imaged simultaneously with skin fluorescence using non-invasive time-saving method by combining CLSM and linear unmixing achieving a depth profile of 760 μm . Finally, our study can be considered as a platform for putting insights into the design, optimization and better understanding of the AuNCs formation and properties. The development of AuNCs-modified GNPs represents a very promising approach for imaging in a challenging tissue as skin that

can extend to various theranostic and pharmaceutical applications, preferably antigen delivery for transcutaneous vaccination.

3.6. References

1. Xia F, Hou W, Zhang C, Zhi X, Cheng J, de la Fuente JM, et al. pH-responsive gold nanoclusters-based nanoprobe for lung cancer targeted near-infrared fluorescence imaging and chemo-photodynamic Therapy. *Acta Biomater.* 2018;68:308-19.
2. Chen Y, Montana DM, Wei H, Cordero JM, Schneider M, Le Guével X, et al. Shortwave infrared in vivo imaging with gold nanoclusters. *Nano Lett.* 2017;17(10):6330-4.
3. Wang Y, Hu L, Li L, Zhu J-J. Fluorescent gold nanoclusters: Promising fluorescent probes for sensors and bioimaging. *J Anal Test* 2017;1:13.
4. Sun Y, Wu J, Wang C, Zhao Y, Lin Q. Tunable near-infrared fluorescent gold nanoclusters: temperature sensor and targeted bioimaging. *New J Chem.* 2017;41:5412-9.
5. Pan Y, Li Q, Zhou Q, Zhang W, Yue P, Xu C, et al. Cancer cell specific fluorescent methionine protected gold nanoclusters for in-vitro cell imaging studies. *Talanta.* 2018;188:259-65.
6. Biswas A, Banerjee S, Gart EV, Nagaraja AT, McShane MJ. Gold nanocluster containing polymeric microcapsules for intracellular ratiometric fluorescence biosensing. *ACS Omega.* 2017;2(6):2499-506.
7. Lakkakula JR, Divakaran D, Thakur M, Kumawat MK, Srivastava R. Cyclodextrin-stabilized gold nanoclusters for bioimaging and selective label-free intracellular sensing of Co^{2+} ions. *Sens Actuators B Chem.* 2018;262:270-81.
8. Zheng K, Setyawati MI, Leong DT, Xie J. Antimicrobial gold nanoclusters. *ACS Nano.* 2017;11(7):6904-10.
9. Yahia-Ammar A, Sierra D, Mérola F, Hildebrandt N, Le Guével X. Self-assembled gold nanoclusters for bright fluorescence imaging and enhanced drug delivery. *ACS Nano.* 2016;10:2591-9.
10. Zhang P. X-ray spectroscopy of gold-thiolate nanoclusters. *J Phys Chem C.* 2014;118:25291-9.
11. Chevrier D, M, Yang R, Chatt A, Zhang P. Bonding properties of thiolate-protected gold nanoclusters and structural analogs from x-ray absorption spectroscopy. *Nanotechnol Rev.* 2015. p. 193.
12. Palmal S, Jana Nikhil R. Gold nanoclusters with enhanced tunable fluorescence as bioimaging probes. *Wiley Interdiscip Rev Nanomed Nanobiotechnol.* 2013;6:102-10.
13. Li D, Chen Z, Mei X. Fluorescence enhancement for noble metal nanoclusters. *Adv Colloid Interface Sci.* 2017;250:25-39.
14. Cantelli A, Battistelli G, Guidetti G, Manzi J, Di Giosia M, Montalti M. Luminescent gold nanoclusters as biocompatible probes for optical imaging and theranostics. *Dyes and Pigments.* 2016;135:64-79.
15. Bain D, Maity S, Paramanik B, Patra A. Core-size dependent fluorescent gold nanoclusters and ultrasensitive detection of Pb^{2+} ion. *ACS Sustainable Chem Eng.* 2018;6:2334-43.
16. Wu Z, Jin R. On the ligand's role in the fluorescence of gold nanoclusters. *Nano Lett.* 2010;10:2568-73.

17. Pramanik G, Humpolickova J, Valenta J, Kundu P, Bals S, Bour P, et al. Gold nanoclusters with bright near-infrared photoluminescence. *Nanoscale*. 2018;10(8):3792-8.
18. Warner MG, Reed SM, Hutchison JE. Small, Water-soluble, ligand-stabilized gold nanoparticles synthesized by interfacial ligand exchange reactions. *Chem Mater*. 2000;12:3316-20.
19. Xu Y, Sherwood J, Qin Y, Crowley D, Bonizzoni M, Bao Y. The role of protein characteristics in the formation and fluorescence of Au nanoclusters. *Nanoscale*. 2014;6:1515-24.
20. Bai Y, Zhou Y, Liu H, Fang L, Liang J, Xiao S. Glutathione-stabilized fluorescent gold nanoclusters vary in their influences on the proliferation of pseudorabies virus and porcine reproductive and respiratory syndrome virus. *ACS Appl Nano Mater*. 2018;1:969-76.
21. Kong L, Chu X, Ling X, Ma G, Yao Y, Meng Y, et al. Biocompatible glutathione-capped gold nanoclusters for dual fluorescent sensing and imaging of copper(II) and temperature in human cells and bacterial cells. *Microchim Acta*. 2016;183:2185-95.
22. Polavarapu L, Manna M, Xu Q-H. biocompatible glutathione capped gold clusters as one- and two-photon excitation fluorescence contrast agents for live cells imaging. *Nanoscale*. 2011;3:429-34.
23. Wu B-Y, Wang C-W, Chen P-C, Chang H-T. Glutathione assisted preparation of gold nanoclusters using minimum amount of protein. *Sensor Actuat B-Chem*. 2017;238:1258-65.
24. Zhang C, Zhou Z, Qian Q, Gao G, Li C, Feng L, et al. Glutathione-capped fluorescent gold nanoclusters for dual-modal fluorescence/x-ray computed tomography imaging. *J Mater Chem B*. 2013;1:5045-53.
25. Chen L-Y, Wang C-W, Yuan Z, Chang H-T. Fluorescent gold nanoclusters: Recent advances in sensing and imaging. *Anal Chem*. 2015;87:216-29.
26. Chuang K-T, Lin Y-W. Microwave-assisted formation of gold nanoclusters capped in bovine serum albumin and exhibiting red or blue emission. *J Phys Chem C*. 2017;121:26997-7003.
27. Le Guével X, Hötzer B, Jung G, Hollemeyer K, Trouillet V, Schneider M. Formation of fluorescent metal (Au, Ag) nanoclusters capped in bovine serum albumin followed by fluorescence and spectroscopy. *J Phys Chem C*. 2011;115:10955-63.
28. Russell BA, Jachimska B, Kralka I, Mulheran PA, Chen Y. Human serum albumin encapsulated gold nanoclusters: Effects of cluster synthesis on natural protein characteristics. *J Mater Chem B*. 2016;4:6876-82.
29. Yang S, Jiang Z, Chen Z, Tong L, Lu J, Wang J. Bovine serum albumin-stabilized gold nanoclusters as a fluorescent probe for determination of ferrous ion in cerebrospinal fluids via the fenton reaction. *Microchim Acta*. 2015;182:1911-6.
30. Yue Q, Sun L, Shen T, Gu X, Zhang S, Liu J. Synthesis of fluorescent gold nanoclusters directed by bovine serum albumin and application for nitrite detection. *J Fluoresc*. 2013;23:1313-8.
31. Zhao T, Xuan ZQ, Wan A, Gui R. Bovine serum albumin template synthesis of fluorescent gold nanoclusters for nitric oxide detection in vitro. *Mater Technol*. 2016;31:342-7.
32. Liu C-L, Wu H-T, Hsiao Y-H, Lai C-W, Shih C-W, Peng Y-K, et al. Insulin-directed synthesis of fluorescent gold nanoclusters: preservation of insulin bioactivity and versatility in cell imaging. *Angew Chem Int Ed*. 2011;50:7056-60.

33. Chen P-F, Liu C-L, Lin W-K, Chen K-C, Chou P-T, Chu S-W. Fluorescence depletion properties of insulin–gold nanoclusters. *Biomed Opt Express*. 2015;6:3066-73.
34. Kawasaki H, Yoshimura K, Hamaguchi K, Arakawa R. Trypsin-stabilized fluorescent gold nanocluster for sensitive and selective Hg²⁺ detection. *Anal Sci*. 2011;27:591-.
35. Liu J-M, Chen J-T, Yan X-P. Near infrared fluorescent trypsin stabilized gold nanoclusters as surface plasmon enhanced energy transfer biosensor and in vivo cancer imaging bioprobe. *Anal Chem*. 2013;85:3238-45.
36. Lu D, Liu L, Li F, Shuang S, Li Y, Choi MMF, et al. Lysozyme-stabilized gold nanoclusters as a novel fluorescence probe for cyanide recognition. *Spectrochim Acta A Mol Biomol Spectrosc*. 2014;121:77-80.
37. Russell BA, Jachimska B, Komorek P, Mulheran PA, Chen Y. Lysozyme encapsulated gold nanoclusters: effects of cluster synthesis on natural protein characteristics. *Phys Chem Chem Phys*. 2017;19:7228-35.
38. Xu Y, Palchoudhury S, Qin Y, Macher T, Bao Y. Make Conjugation Simple: A facile approach to integrated nanostructures. *Langmuir*. 2012;28:8767-72.
39. Nandi I, Chall S, Chowdhury S, Mitra T, Roy SS, Chattopadhyay K. Protein fibril-templated biomimetic synthesis of highly fluorescent gold nanoclusters and their applications in cysteine sensing. *ACS Omega*. 2018;3(7):7703-14.
40. Sahoo N, Sahoo RK, Biswas N, Guha A, Kuotsu K. Recent advancement of gelatin nanoparticles in drug and vaccine delivery. *Int J Biol Macromol*. 2015;81:317-31.
41. Lai J-Y, Li Y-T, Cho C-H, Yu T-C. Nanoscale modification of porous gelatin scaffolds with chondroitin sulfate for corneal stromal tissue engineering. *Int J Nanomedicine*. 2012;7:1101–14.
42. Parry KL, Shard AG, Short RD, White RG, Whittle JD, Wright A. ARXPS characterisation of plasma polymerised surface chemical gradients. *Surf Interface Anal*. 2006;38:1497-504.
43. Scofield JH. Hartree-Slater subshell photoionization cross-sections at 1254 and 1487 eV. *J Electron Spectr Relat Phen*. 1976;8:129-37.
44. Stracke F, Weiss B, Lehr C-M, König K, Schaefer UF, Schneider M. Multiphoton microscopy for the investigation of dermal penetration of nanoparticle-borne drugs. *J Invest Dermatol*. 2006;126:2224-33.
45. Samanta A, Zhou Y, Zou S, Yan H, Liu Y. Fluorescence quenching of quantum dots by gold nanoparticles: a potential long range spectroscopic ruler. *Nano Lett*. 2014;14:5052-7.
46. Liu Y, Liu X, Wang X. Biomimetic synthesis of gelatin polypeptide-assisted noble-metal nanoparticles and their interaction study. *Nanoscale Res Lett*. 2010;6:22.
47. Wangoo N, Bhasin KK, Mehta SK, Suri CR. Synthesis and capping of water-dispersed gold nanoparticles by an amino acid: bioconjugation and binding studies. *J Colloid Interface Sci*. 2008;323:247-54.
48. Van Vlierbergh S, Graulus GJ, Keshari Samal S, Van Nieuwenhove I, Dubruel P. Porous hydrogel biomedical foam scaffolds for tissue repair. In: Netti PA, editor. *Biomedical Foams for Tissue Engineering Applications*: Woodhead Publishing; 2014. p. 335-90.
49. Lee BH, Lum N, Seow LY, Lim PQ, Tan LP. synthesis and characterization of types A and B gelatin methacryloyl for bioink applications. *Materials (Basel)*. 2016;9.

50. Suarasan S, Focsan M, Soritau O, Maniu D, Astilean S. One-pot, green synthesis of gold nanoparticles by gelatin and investigation of their biological effects on osteoblast cells. *Colloids Surf B Biointerfaces*. 2015;132:122-31.
51. Harkness KM, Cliffel DE, McLean JA. Characterization of thiolate-protected gold nanoparticles by mass spectrometry. *Analyst*. 2010;135:868-74.
52. Barth A. Infrared spectroscopy of proteins. *Biochim Biophys Acta, Bioenerg*. 2007;1767:1073-101.
53. Le Guével X, Trouillet V, Spies C, Li K, Laaksonen T, Auerbach D, et al. High photostability and enhanced fluorescence of gold nanoclusters by silver doping. *Nanoscale*. 2012;4:7624-31.
54. Zhang J, Yuan Y, Wang Y, Sun F, Liang G, Jiang Z, et al. Microwave-assisted synthesis of photoluminescent glutathione-capped Au/Ag nanoclusters: A unique sensor-on-a-nanoparticle for metal ions, anions, and small molecules. *Nano Res*. 2015;8:2329-39.
55. Wang S, Meng X, Das A, Li T, Song Y, Cao T, et al. A 200-fold quantum yield boost in the photoluminescence of silver-doped Ag_xAu_{25-x} nanoclusters: The 13th silver atom matters. *Angew Chem Int Ed Engl*. 2014;53(9):2376-80.
56. Casaletto MP, Longo A, Martorana A, Prestianni A, Venezia AM. XPS study of supported gold catalysts: The role of Au⁰ and Au^{+δ} species as active sites. *Surf Interface Anal*. 2006;38:215-8.
57. Dixon JM, Egusa S. Conformational change-induced fluorescence of bovine serum albumin-gold complexes. *J Am Chem Soc*. 2018;140:2265-71.
58. Chevrier DM, Chatt A, Zhang P. Properties and applications of protein-stabilized fluorescent gold nanoclusters: short review. *J Nanophoton*. 2012;6(1):064504.
59. Bourg M-C, Badia A, Lennox RB. Gold-sulfur bonding in 2D and 3D self-assembled monolayers: XPS characterization. *J Phys Chem B*. 2000;104:6562-7.
60. Descostes M, Mercier F, Thromat N, Beaucaire C, Gautier-Soyer M. Use of XPS in the determination of chemical environment and oxidation state of iron and sulfur samples: constitution of a data basis in binding energies for Fe and S reference compounds and applications to the evidence of surface species of an oxidized pyrite in a carbonate medium. *Appl Surf Sci*. 2000;165:288-302.
61. Wu Y-T, Shanmugam C, Tseng W-B, Hiseh M-M, Tseng W-L. A gold nanocluster-based fluorescent probe for simultaneous pH and temperature sensing and its application to cellular imaging and logic gates. *Nanoscale*. 2016;8:11210-6.
62. Deng Y, Gruppen H, Wierenga PA. Comparison of protein hydrolysis catalyzed by bovine, porcine, and human trypsins. *J Agric Food Chem*. 2018;66:4219-32.
63. Wu Z. Anti-galvanic reduction of thiolate-protected gold and silver nanoparticles. *Angew Chem Int Ed*. 2012;51:2934-8.
64. Choi J-P, Fields-Zinna CA, Stiles RL, Balasubramanian R, Douglas AD, Crowe MC, et al. Reactivity of [Au₂₅(SCH₂CH₂Ph)₁₈]¹⁻ nanoparticles with metal ions. *J Phys Chem C*. 2010;114:15890-6.
65. Li H-W, Yue Y, Liu T-Y, Li D, Wu Y. Fluorescence-enhanced sensing mechanism of bsa-protected small gold-nanoclusters to silver(I) ions in aqueous solutions. *J Phys Chem C*. 2013;117:16159-65.

66. Coester CJ, Langer K, Von Briesen H, Kreuter J. Gelatin nanoparticles by two step desolvation a new preparation method, surface modifications and cell uptake J Microencapsulation. 2000;17:187-93.
67. Khan SA, Schneider M. Stabilization of gelatin nanoparticles without crosslinking. Macromol Biosci. 2014;14:1627-38.
68. Khandelia R, Bhandari S, Pan UN, Ghosh SS, Chattopadhyay A. gold nanocluster embedded albumin nanoparticles for two-photon imaging of cancer cells accompanying Drug Delivery. Small. 2015;11(33):4075-81.
69. Leo E, Angela Vandelli M, Cameroni R, Forni F. Doxorubicin-loaded gelatin nanoparticles stabilized by glutaraldehyde: Involvement of the drug in the cross-linking process. Int J Pharm. 1997;155:75-82.
70. Conde J, Dias JT, Grazú V, Moros M, Baptista PV, de la Fuente JM. Revisiting 30 years of biofunctionalization and surface chemistry of inorganic nanoparticles for nanomedicine. Front Chem. 2014;2.
71. Lanke SSS, Kolli CS, Strom JG, Banga AK. enhanced transdermal delivery of low molecular weight heparin by barrier perturbation. Int J Pharm. 2009;365:26-33.
72. Yang L, Wu L, Wu D, Shi D, Wang T, Zhu X. Mechanism of transdermal permeation promotion of lipophilic drugs by ethosomes. Int J Nanomedicine. 2017;2017:12 3357–64.
73. Hathout RM, Mansour S, Geneidi AS, Mortada ND. Visualization, dermatopharmacokinetic analysis and monitoring the conformational effects of a microemulsion formulation in the skin stratum corneum. J Colloid Interface Sci. 2011;354:124-30.
74. Tomoda K, Yabuki N, Terada H, Makino K. Application of polymeric nanoparticles prepared by an antisolvent diffusion with preferential solvation for iontophoretic transdermal drug delivery. Colloid Polym Sci. 2014;292:3195-203.
75. Gratieri T, Schaefer UF, Jing L, Gao M, Kostka KH, Lopez RF, et al. Penetration of quantum dot particles through human skin. J Biomed Nanotechnol. 2010;6:586-95.
76. Zou Y, Celli A, Zhu H, Elmahdy A, Cao Y, Hui X, et al. Confocal laser scanning microscopy to estimate nanoparticles' human skin penetration in vitro. Int J Nanomedicine. 2017;2017:12 8035–41.
77. Zimmermann T. Spectral imaging and linear unmixing in light microscopy. Adv Biochem Eng Biotechnol. 2005;95:245-65.
78. DeMuth PC, Garcia-Beltran WF, Ai-Ling ML, Hammond PT, Irvine DJ. Composite dissolving microneedles for coordinated control of antigen and adjuvant delivery kinetics in transcutaneous vaccination. Adv Funct Mater. 2013;23:161-72.

***Chapter 4. Customized Fast-Separable Microneedles
Prepared with the Aid of 3D Printing for Nanoparticle
Delivery***

Nesma El-Sayed, Lukas Vaut and Marc Schneider

****This chapter has been prepared for publication as a research article***

4. Customized Fast-Separable Microneedles Prepared with the Aid of 3D Printing for Nanoparticle Delivery

4.1. Abstract

3D printing of master molds for soft lithography-based fabrication of microneedles (MNs) is a cost effective, easy and fast method for producing MNs with variable designs. Deviating from the classical geometries of MNs, 'tanto blade'-inspired MNs showed effective skin penetration, acting as sharp structures with low insertion force of 10.6 N, which is sufficient for manual insertion. Additionally, hydrophilic, fluorescent noble metal nanocluster-modified gelatin nanocarriers were loaded in polyvinyl alcohol/sucrose MNs to act as a novel theranostic system emitting light in the near-infrared ($\lambda_{em} = \sim 700$ nm). Nanoparticles (NPs) distribution within the MNs and release have been monitored using confocal laser scanning microscopy by means of spectral analysis and linear unmixing. Furthermore, MNs patch was modified by carving a channel at each of the four corners of the patch. This facilitated the separation process of MNs from the patch base into skin, when a 15 μ L of phosphate buffer saline was applied through each channel post-skin insertion of the MNs. Then, the patch base can be removed easily leaving the implanted MNs inside the skin for further release of the NP cargo. This successfully reduced the application time to 1 min for enhanced patient compliance.

Keywords: microneedles, positive master mold, 3D printing, micro additive manufacturing, fast dissolution, nanoparticles delivery, spectral imaging

4.2. Introduction

Transdermal drug delivery is an attractive route to bypass the first pass effect that can hinder the effectiveness of many drugs (1). On the other hand, skin is an immune cell-rich organ, such as Langerhans and dermal dendritic cells, which renders it an attractive pathway for vaccination (2). However, stratum corneum (SC), as the outermost layer of skin, represents a barrier against effective drug delivery through skin (3, 4). Among the strategies that have been introduced recently to overcome the SC barrier for drug delivery, microneedles (MNs) seem to be a very promising approach. These micro-structures are minimally invasive and a pain-free method to allow drugs and macromolecules bypass the SC and diffuse toward viable skin (5).

Micromolding or soft lithography is the most common method for the fabrication of MNs. The process starts with the fabrication of a positive master mold that is utilized for the preparation of a negative replica. The latter is usually made out of polydimethylsiloxane (PDMS) and can be repeatedly used for the casting of MNs. This method is characterized by controlling the reproducibility of MNs' shape and size (6). Different techniques have been assigned for the preparation of the positive master as photolithography (7), two-photon polymerization (8) and bulk micromachining (9). However, these techniques are complicated as well as expensive and can ultimately hinder the easy manipulation of the MNs' designs. Controlling the shape and dimensions (aspect ratio and tip's radius and angle) of MNs is crucial to manage their effectiveness. These parameters together with the polymers' physical properties affect the mechanical strength and the insertion force and depth of the MNs (10, 11). Computer-aided additive manufacturing ('3D printing') can serve as a simple and cost-effective method for the fabrication of MNs masters with different designs. The ability to optimize the designs of the MNs, and thus obtain the best features in order to fulfill specific requirements, together with the ability to fabricate MNs from different polymers, is highly advantageous. Hence, more customized designs deviating from the traditional shapes (pyramidal, conical etc.) can be realized and tested.

Dissolving MNs are composed of water-soluble polymers that dissolve and release the bioactives, leaving less environmental waste behind. They can effectively penetrate

skin with relatively low insertion forces. Combining dissolving MNs with bioactives-loaded nanoparticles (NPs) offers the advantage of controlling the release rate rather than having one bolus dose (5). In this regard, while designing the MNs and selecting the polymers, several aspects should be considered sequentially; 1) the MNs need to be robust enough to be inserted into skin, and then 2) separate fast from the patch base and solubilize in the interstitial fluid of the skin to 3) release the NPs which carry the medical cargo and control its delivery into the skin.

Herein, we initiated a cost-effective fabrication sequence of MNs in the lab starting from building a master mold using 3D printing and ending with NPs-loaded dissolving MNs as the final product. Among various possible designs, we have selected a 'tanto blade'-inspired design to enhance the insertion-ability of the MNs into skin. Nanoparticles synthesized from noble metals nanoclusters-labelled gelatin serve as a fluorescent probe (12) for imaging the MNs dissolution *in vitro* and their behavior inside excised human skin. A mixture of poly (vinyl alcohol) (PVA) and sucrose was used for the preparation of the MNs matrix. The design of the MNs patch was further modified by forming 4 channels through the corners of the patch base. This allowed enhancing the separation of the MNs from the base after insertion in human skin, using a small buffer volume. The current research represents an orientation towards enhancing the feasibility of designing different customized MNs and modifying their properties according to request. We envisage this work would provide more flexibility for researchers to develop and screen new designs and biomaterials for MNs manufacturing. Our final aim is to increase the effectiveness of drug delivery by MNs and ultimately enhance the patients' compliance.

4.3. Materials and Methods

4.3.1. Materials

HTM 140M acrylate-based 3D printing material (EnvisionTEC GmbH, Gladbeck, Germany) was used for 3D printing. SYLGARD 184 polydimethylsiloxane (PDMS) silicone elastomer (Dow Corning, Midland, US) was used as a molding material. Hydrogen tetrachloroaurate (III) trihydrate ($\text{HAuCl}_4 \cdot 3\text{H}_2\text{O}$), gelatin type B (from bovine skin, gel strength ~75 g Bloom), silver nitrate, N-(3-dimethylaminopropyl)-N'

4. Customized fast-separable microneedles prepared with the aid of 3D printing for nanoparticle delivery

ethylcarbodiimide hydrochloride (EDC), N-Hydroxysuccinimide (NHS), poly(vinyl alcohol) (Mw 31,000), sucrose, agarose, methanol, Parafilm® 'M' were all purchased from Sigma Aldrich, Steinheim, Germany. All chemicals were utilized without further purification. Milli-Q ultrapure water has been used for all experiments.

4.3.2. Design and fabrication of microneedles molds

The general microneedles fabrication scheme followed a three-step indirect tooling approach using a positive MNs mold master to create a negative mold, which ultimately served to replicate the final MNs patch.

4.3.2.1. Design of positive microneedles mold master

Two different MNs mold masters were designed using OpenSCAD open-source computer-aided design software. The MNs were designed as polyhedrons consisting of 10 faces each and patterned in an alternating linear array in a 10 x 10 mm sized area.

4.3.2.2. 3D printing of positive microneedles mold master

The design of the MNs mold master was exported as STL file and 3D printed using a Perfactory Micro Plus High-Res Digital Light Processing (DLP) 3D printer (EnvisionTEC GmbH, Gladbeck, Germany) with a horizontal resolution of 30 μm (pixel size) and a layer height of 15 μm . The finished mold master print was removed from the printing platform using a spatula, subsequently immersed in 2-propanol and placed in an ultrasound bath. After 5 min of sonication, the mold master was retrieved and left to dry. Finally, the mold master was placed in a UV-oven (EnvisionTEC GmbH, Gladbeck, Germany) for 10 min of post-curing treatment.

Scanning electron microscopy was performed using a TM3030Plus tabletop scanning electron microscope (Hitachi High Technologies Europe GmbH, Krefeld, Germany) and a Zeiss Supra 40 VP scanning electron microscope (Carl Zeiss Microscopy GmbH, Jena, Germany). A 208HR high resolution sputter coater (Cressington Scientific Instruments, Watford, UK) equipped with a gold target was used to coat the specimens with a thin layer of gold (≈ 20 nm) prior to observation.

4.3.2.3. Molding of negative microneedles mold

A frame for the mold master was designed in Corel Draw X7 (Corel Corporation, Canada) and laser-cut from 5 mm acrylic using a Mini 18 CO₂ laser cutter (Epilog Corporation, US). The frame was then secured to the mold master with several screws. The mold master was filled with PDMS, placed into a vacuum chamber for 30 min and then placed in an oven at 80 °C for 60 min. Finally, the frame was detached from the mold master and the negative PDMS mold was extracted.

4.3.3. Preparation of nanoclusters loaded gelatin nanoparticles (NCs-GNPs)

Gold/silver alloy nanoclusters have been synthesized as described earlier (12) by adding HAuCl₄ to gelatin (40 mg/ml) and glutathione (0.7 mM) solution followed by adjusting the pH to 11 using 1N sodium hydroxide. The reaction has been carried out under vigorous mixing using a thermomixer (MHR, Hettich Benelux, Geldermalsen, The Netherlands) at 60 °C. After 6 h, a solution of silver nitrate was added in a molar ratio Ag/Au of 0.4, and the reaction was left to continue up to 24 h. For stopping the reaction, the pH of the mixture was adjusted to pH 7 using 1N HCl.

The NPs were prepared by a two-step desolvation method (12) using methanol as antisolvent and crosslinking using a mixture of EDC/NHS for 18 h. They were purified by centrifugation (Thermo Fisher Scientific, Osterode am Harz, Germany) at 20,000 g for 1 h at 20 °C, followed by 3 washing steps. Then, they were characterized for size and zeta potential using a Zetasizer (Nano ZS, Malvern Instruments Ltd, Malvern, UK), as well as morphology using a transmission electron microscope (TEM) (JEOL JEM 2100, JEOL GmbH, Freising, Germany) operating at a maximum accelerating voltage of 250 kV.

4.3.4. Molding of nanoparticles loaded-microneedles patches

The NPs dispersion was mixed well with a mixture of PVA/sucrose, resulting in a final NPs' concentration of 1.5 mg/mL in 40% w/v PVA and 40% w/v sucrose. The mixture was degassed and equilibrated for 24 h to eliminate any trapped air. Each MNs mold was filled with 40 µL of the mixture and centrifuged (Universal 32R, Hettich, Geldermalsen, The Netherlands) at 3640 g for 7 min at 23 °C. Then the extra solution was carefully removed from the mold and the process was repeated 3 times. The

molds were kept under vacuum for 15 min and then 200 μL of plain PVA/sucrose solution was added to form the patch base. The filled molds were kept in a desiccator for 2 days and then the MNs were removed from the molds to be further kept and dried for 5 more days in the desiccator at room temperature.

4.3.5. Characterization of NCs-GNPs-loaded MNs

4.3.5.1. Fracture force

The MNs fracture force was determined using a TA.XT plus texture analyzer instrument equipped with a 10 kg load cell (Stable Micro Systems Ltd, Godalming, UK). Microneedles patches were secured onto the probe holder with double-sided adhesive tape and lowered upside-down onto a solid plate of aluminum with a test speed of 0.01 mm/s until reaching a force of 40 N. The measured fracture force was recorded throughout the experiment.

4.3.5.2. Penetration force

Measurement of the force required to penetrate an artificial skin substitute with MNs was conducted with a TA.XT plus texture analyzer (Stable Micro Systems Ltd, Godalming, UK), similarly to how it is described for the fracture force determination. A disc of agarose gel (2% casted gel) of 6 mm thickness covered by a parafilm layer of 127 μm thickness has been used as skin substitute [26, 27]. In this case, a skin substitute, which was refrigerated to maintain the gel consistency, was placed below the probe holder and the MNs patch was lowered into it at a test speed of 0.01 mm/s.

4.3.5.3. Confocal laser scanning microscopy (CLSM)

Spectral imaging of the MNs was performed by recording the emission spectrum (569-724 nm) using an excitation laser of 405 nm wavelength using CLSM (LSM 710, Zeiss, Jena, Germany). Linear unmixing was applied to the crude signals using the previously recorded individual spectra of MNs components as references; NCs-GNPs and PVA. For 3D imaging of the MNs patch, z-stacks were recorded at 5 μm steps. In addition, the release of the NPs from the MNs was monitored. 50 μL PBS (pH 7.4) was added to MNs that were separated from the base patch on a microscopic cover slip and after 30 s their spectral images were recorded to further be analyzed by linear unmixing.

4.3.6. Microneedles patch modification and skin penetration studies

To enhance the separation of MNs from the patch base after being inserted into skin the patches have been modified by forming a channel through each of the 4 corners of the squared patch. Skin penetration studies were conducted on human skin in comparison to the unmodified MNs patches. Excised human skin was obtained from abdominal plastic surgeries after the approval of the Research Ethic Committee of Saarland, Germany (Ärzttekammer des Saarlandes, Dec. 2008) and permission of the volunteers. The subcutaneous fatty tissue was removed, and the skin surface was cleaned with water. The skin samples were stored at -20 °C to be used within less than 6 months (13). Skin punches of 25 mm diameter were punched out, thawed and the surfaces were cleaned with ultrapure water. For the unmodified patches, the skin punches were aligned in Franz diffusion cells filled with 12 mL PBS with the *stratum corneum* facing upside. The skin was left to hydrate for 1 h, removed from the Franz cells, fixed over a cork plane and the MNs were pressed against the skin surface by thumb for 30 s and then a weight of 10 g was applied over the MNs patch. Then skin samples were returned carefully to the Franz cells. The setup was kept at 37 °C while stirring the buffer in the receiver compartment for 3 h and then the MNs patch was removed (14). The modified MNs patches (with channels) were inserted into the skin fixed over a cork plane by thumb for 30 s. 15 µL PBS was dropped in each channel and then the MNs were lifted from the skin after 1 min. All the MNs patches were imaged by a digital camera before and after insertion into skin. The skin samples were mounted over a wet filter paper in a circular chamber fixed on a microscopic slide with the skin surface facing upwards that was covered by a cover slip (15) to be examined by CLSM after 30 min. Different skin areas were scanned for their spectral images that were further analyzed by linear unmixing using skin, PVA and NCs-GNPs recorded spectra as references.

4.4. Results and Discussion

4.4.1. Design and development of MNs molds

According to literature, different dissolving MNs common designs have been introduced: conical (16), pyramidal (10, 17, 18) and circular (19) or square obelisk (20). Researchers have manipulated the aspect ratio, angles and tip dimension to enhance

4. Customized fast-separable microneedles prepared with the aid of 3D printing for nanoparticle delivery

the mechanical properties and the penetration ability of the MNs (21). Herein, we are introducing new designs that are inspired by a 'Tanto blade'. Tanto is a traditional Japanese Samurai sword with a special design. It has 2 bevels; a short more vertical one (at the front) and a long straight one (extends to the hilt) (Figure 1), where the beveled tip allows for enhanced penetration. Figure 2A shows 2 designs for the MNs with the same aspect ratio; height (Z) of 800 μm and triangle base of X= 300 μm and Y= 200 μm . However, they differ in the ratio of the height of the 2 bevels that affects the final geometry and the tip angle as shown in Figure 2A.

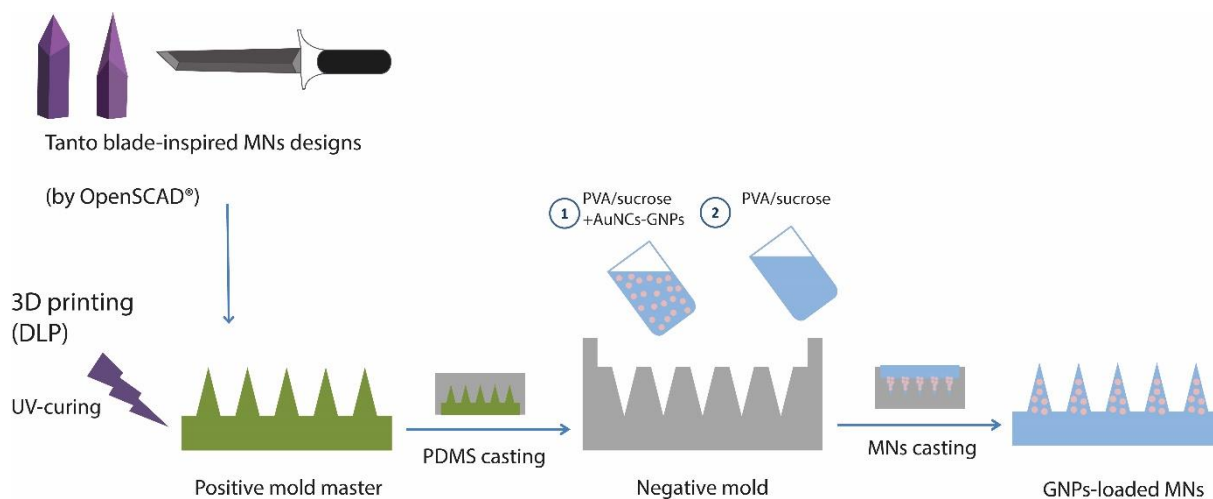


Figure 1. A scheme representing the steps of manufacturing tanto blade-inspired microneedles (MNs) loaded with NIR-emitting gold/silver nanoclusters-labelled gelatin nanoparticles (NCs-GNPs). This includes 1) 3D-design of 2 potential MNs using OpenSCAD software, 2) 3D printing of the positive mold master using DLP technology followed by UV-curing of the resin, 3) production of negative mold replica by PDMS casting, 4) MNs preparation using NCs-GNPs embedded in PVA/sucrose matrix by molding, centrifugation and vacuuming, followed by plain base casting using PVA/sucrose only, and finally 5) drying of the MNs in a desiccator and removal from the mold.

Positive master molds have been produced by digital light processing (DLP) 3D printing technology. The 3D printing offers flexibility in the MNs design that makes it easier for researchers to design and manufacture a wide range of customized MNs in the lab. However, it is worth mentioning that the technique has resolution limits which was as follows in our case: 30 μm horizontally with a layer height of 15 μm . The 3D-printed

4. Customized fast-separable microneedles prepared with the aid of 3D printing for nanoparticle delivery

MNs were imaged by SEM from different perspectives as shown in Figure 2B, C and D. The height of the MNs was 759 and 660 μm , tip diameter was 23 and 9 μm and tip angle 66 and 39° for design 1 (MN1) and design 2 (MN2), respectively. All were measured by image J software. The masters were included in a housing (Figure 2E) to be further used for negative mold casting using PDMS as indicated in Figure 1.

4.4.2. Manufacturing of MNs by molding and NPs loading

Loading of the MNs with NPs can provide a good opportunity for controlling the delivery rate of drugs or biomacromolecules into skin instead of bolus dosing (5). Gelatin NPs are potential candidates for the delivery of macromolecules as antigens due to their hydrophilicity and biocompatibility (22). Rendering gelatin NPs fluorescent, by labelling with noble metal NCs, to act as a bioimaging probe, adds more functionality and allows simultaneous imaging of the NPs within MNs and skin. In our previous research we have introduced NIR emitting gold/silver alloy NCs-labelled gelatin as a new bioimaging probe that can be imaged distinctly and simultaneously with skin autofluorescence to provide a detailed imaging without skin pre-treatment (12). Gold/silver nanoclusters are composed from several to tens of atoms of the metals forming small structures < 2 nm. At this very small size, they show unique properties such as emitting fluorescence when exposed to light of a certain wavelength (23, 24). NIR-emitting gold and silver alloy NCs have been synthesized by using gelatin as a reducing agent for Au^{3+} and Ag^+ ions and a capping agent for the formed clusters in the presence of glutathione (GSH) as a co-reducing agent (12). According to our previous research, they showed maximum emission at 700 nm when excited at 405 nm (12). The fluorescently labelled gelatin was successfully turned into NPs with an average diameter of 218 nm and imaged by TEM to show the NCs' distribution inside the particles (Figure 3A).

4. Customized fast-separable microneedles prepared with the aid of 3D printing for nanoparticle delivery

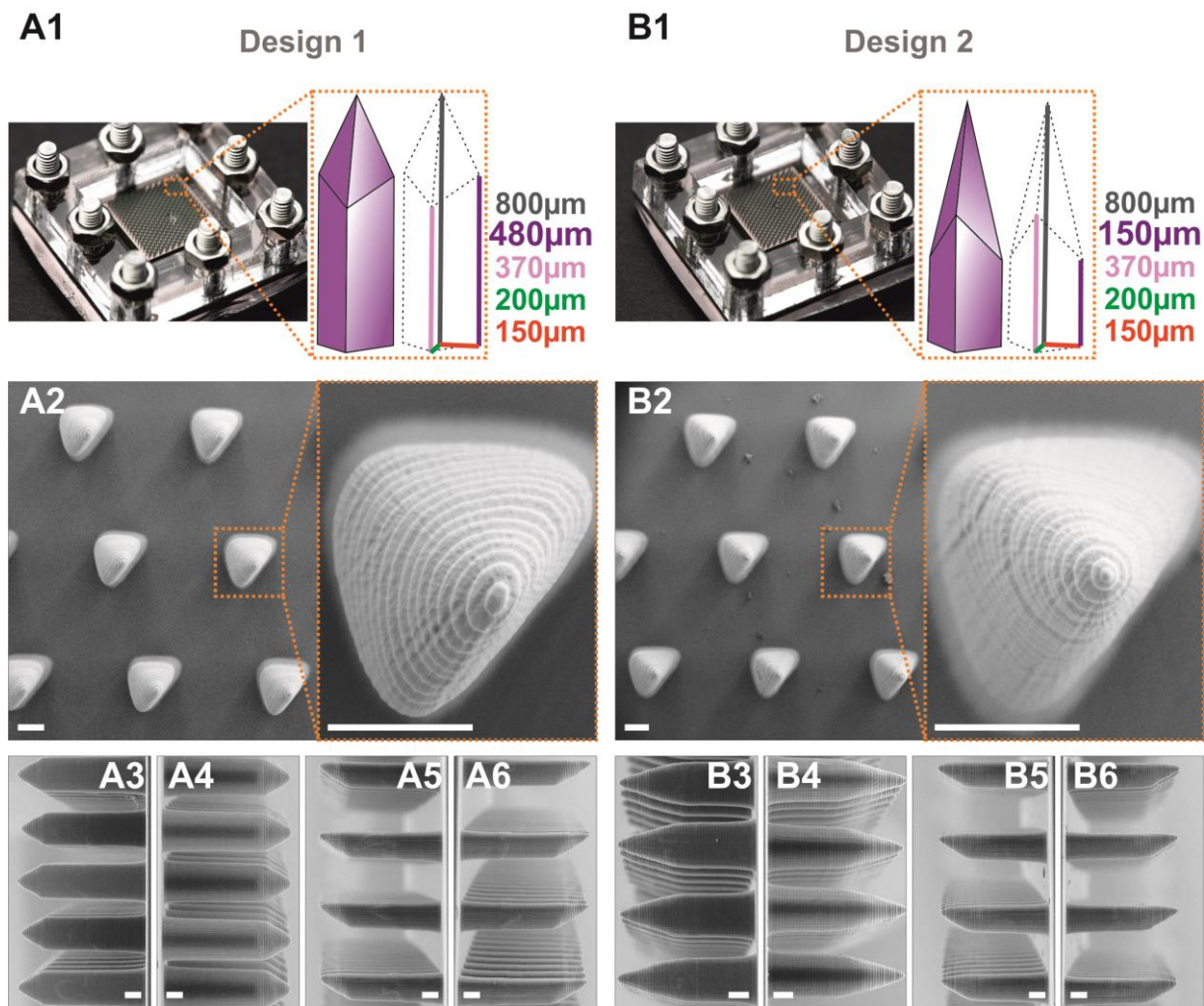


Figure 2. Manufacturing of positive mold masters of 2 potential tanto blade-inspired MNs designs: design 1 (A) and design 2 (B). 1) Photograph of the 3D-printed MNs positive mold master in the final housing to be further used for PDMS casting of the negative mold and illustration of the 3D design of the MNs. 2-6) SEM micrographs of the 3D printed MNs showing top (2), back (3), front (4) and sides (5, 6). All scale bars correspond to 100 μm .

The MNs were successfully prepared by molding PVA/sucrose (1:1) solution with the dispersed NPs of 1.5 mg/mL final concentration. The formed MNs showed a replicated morphology of the positive master with heights of 732 and 643 μm , tip diameters of 33 and 12 μm and tip angles of 63 and 33 $^\circ$ for MN1 and MN2, respectively (Figure 3B and C).

4. Customized fast-separable microneedles prepared with the aid of 3D printing for nanoparticle delivery

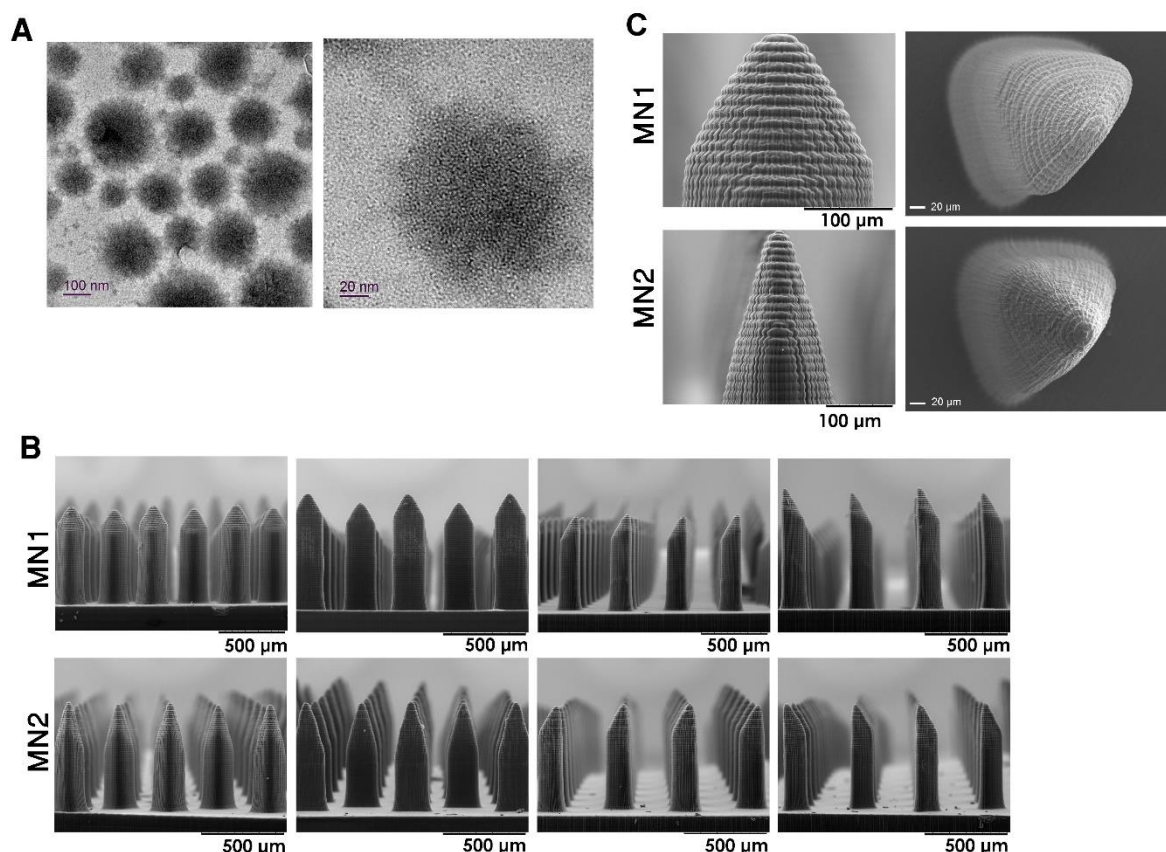


Figure 3. A) TEM micrograph of NCs-labelled GNPs showing the inner distribution of NCs. B) SEM micrograph of NCs-GNPs loaded PVA/sucrose dried MNs; design 1 (MN1) in the upper panel and design 2 (MN2) in the lower panel showing from left to right (front, back and both sides); C) magnified SEM micrographs of microneedles: MN1 in the upper panel and MN2 in the lower panel showing front and top view, at left and right, respectively.

4.4.3. Mechanical properties of MNs

Appropriate mechanical properties are crucial for MNs application. The MNs should be durable to withstand the applied insertion pressure. Although, the insertion is more reproducible by an applicator, the manual insertion by thumb is more simple and convenient for patients (25). Despite the variation in the insertion force between individuals, Larrañeta *et al.* have found that the average insertion force by thumb from 20 individuals for 30 s is 20 N (25). Herein, the insertion test has been conducted using a skin substitute designed to mimic the skin elasticity and the supportive tissue underneath using parafilm as top layer (25, 26) and a supportive agarose gel disc for the underlying tissue (27) (Figure 4A). The insertion forces for MN2 and MN1 were

4. Customized fast-separable microneedles prepared with the aid of 3D printing for nanoparticle delivery

10.6 N and 12.9 N, respectively (Figure 4B). The retrieved patches showed robust MNs for MN2, while MN1 showed some of the MNs broken at the base (Figure 4C). This indicates higher insertion capabilities that can be attributed to the sharper tip and the higher ratio of the front bevel to the MNs base of MN2 compared to MN1. On the other hand, the fracture force of the MNs should be higher than the insertion force to avoid premature breakage of the MNs. Both MNs showed breaking or compression of the tip (Figure 5C) when forced against a solid surface (Figure 5A), while the force of fracture was higher for MN2 (21.9 N) than MN1 (14.1 N) (Figure 5B). Explicitly, MN2 showed the optimum mechanical properties for application where the force of fracture (21.9 N) is about the double of the force of insertion (10.6 N).

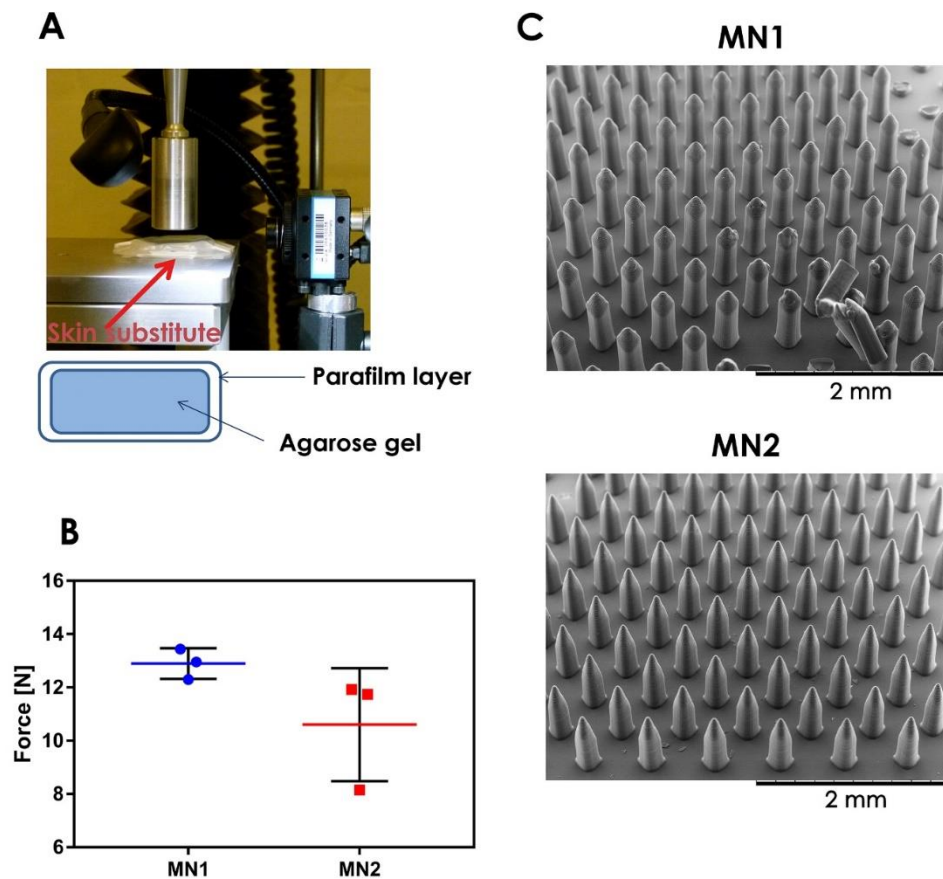


Figure 4. Insertion test of the MNs; design 1 (MN1) and design 2 (MN2) using skin substitute consisting of a 6 mm-thick agarose gel disc covered by a 127 μm-thick parafilm layer. A) Experimental setup using skin substitute and texture analyzer to test the insertion capability of MNs. B) A graph showing the minimum force (N) required for penetration of the parafilm layer and entering the agarose gel (mean ± SD, n=3). C) SEM micrographs of MNs retrieved after insertion in skin substitute.

4. Customized fast-separable microneedles prepared with the aid of 3D printing for nanoparticle delivery

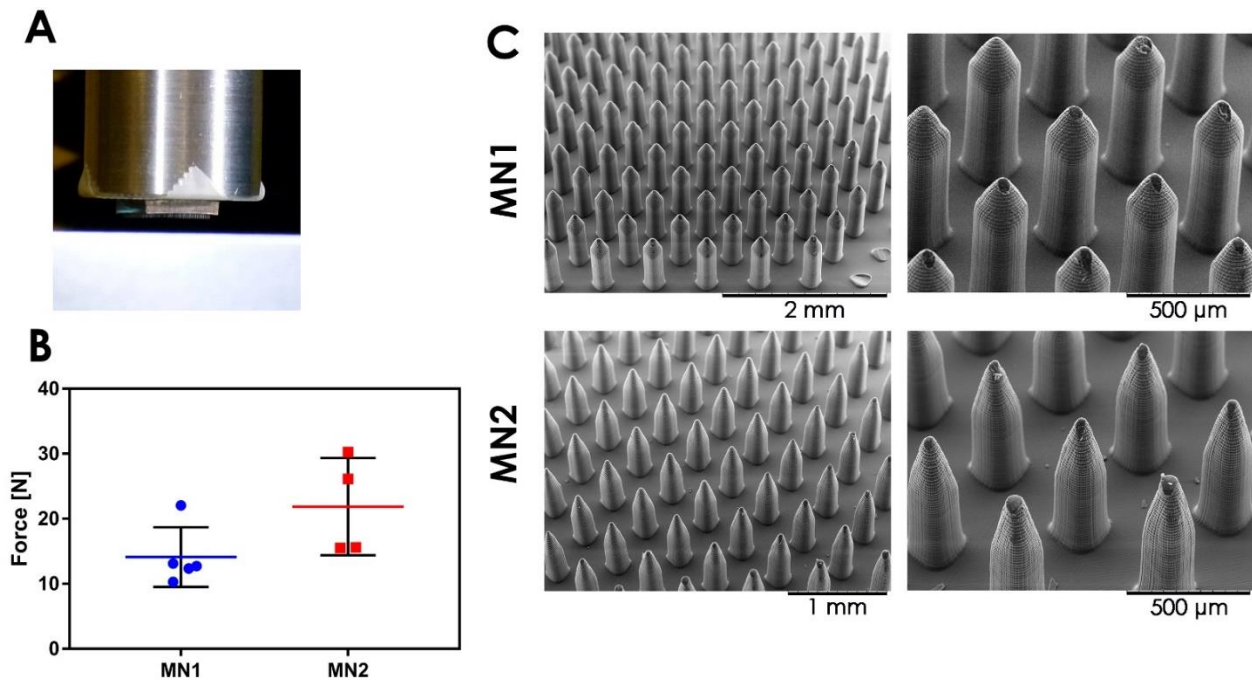


Figure 5. Fracture test of the MNs against metal surface using texture analyzer. A) Experimental setup, B) Graph showing the minimum force (N) required to fracture the MNs and C) SEM micrographs of MNs retrieved after fracture test showing dented tips of the MNs. (mean \pm SD, n=5, n=4)

4.4.4. Spectral imaging

Spectral analysis is a method of fluorescence imaging where the spectral information from the sample is recorded. This allows to separate overlapping signals into single chromophores by linear unmixing using an algorithm and the previously recorded individual reference spectra (28). We were interested in imaging NCs-GNPs, MNs matrix and skin separately as well as simultaneously to finally obtain detailed images showing the distribution of these biomaterials within the tissue. Additionally, *in vitro* examination for the NPs distribution and release from MNs were of interest. NCs-GNPs showed emission in the red part of the spectrum with maximum emission at 700 nm. On the other hand, PVA has shown a broad spectrum fluorescence when excited at 405 nm (Figure 6A1) that was already described in literature (29). However, the emission spectrum of PVA has shown high similarity to skin autofluorescence described in our previous investigation (12).

4. Customized fast-separable microneedles prepared with the aid of 3D printing for nanoparticle delivery

By recording the spectrum from the NPs-loaded MNs, one can define the distribution of the NPs within the MNs matrix (Figure 6A2). The figure shows the color of the fluorescence determined from the real spectrum; the pink and the yellow pixels are linked to the NPs and PVA matrix, respectively. Combining z-stacks (with 5 μm steps) and spectral analysis with linear unmixing, a 3D image of the MNs has been constructed showing the nanoparticles distributed within the MNs pillars, while the patch base is almost free of NPs, except from small agglomerates (Figure 6B). During the MNs patch manufacturing, the patch base was carefully assembled out of plain PVA/sucrose, in order to avoid wasting the NPs dosage. Additionally, spectral imaging has been used to monitor NPs release from the MNs. They were released fast from MNs (within 30 s) when exposed to PBS due to the fast dissolution of the MNs matrix as showed in Figure 6C.

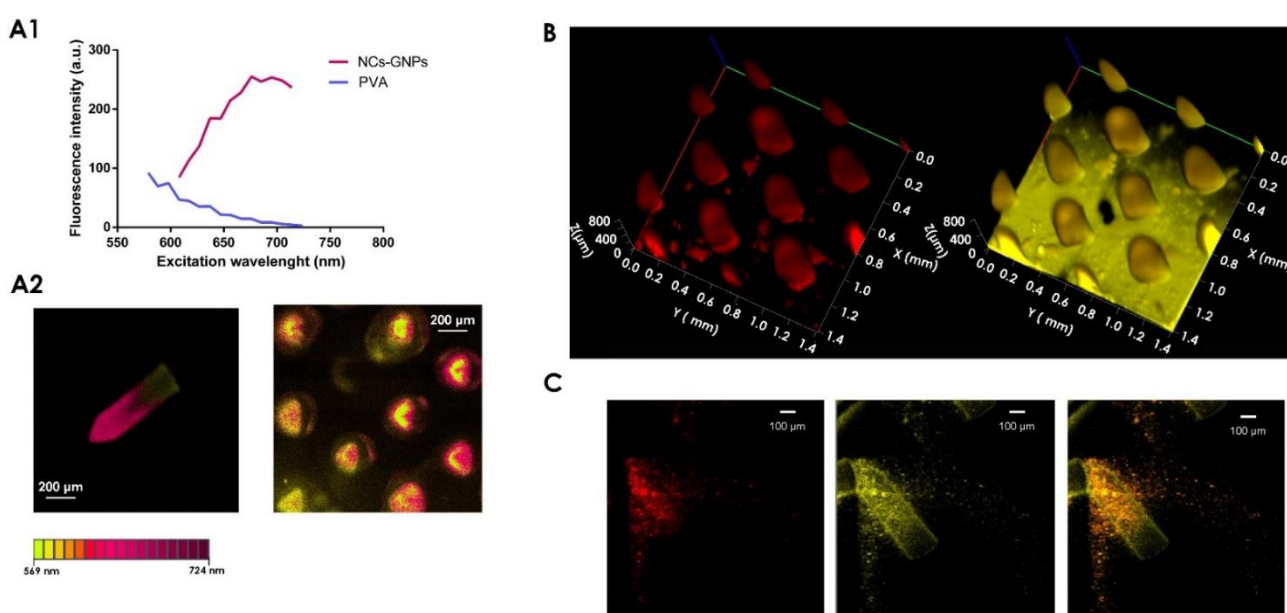


Figure 6. Characterization of MNs by confocal microscopy using 405 nm laser excitation. A1) Emission spectra (575 – 800 nm) recorded by CLSM for both NCs-GNPs and PVA. A2) Spectral images of a single microneedle (left) and top view of the MNs patch (right) colors displayed correspond to the weighed spectral information from the emission wavelength (Pink: NPs and yellow: PVA). B) Reconstructed 3D CLSM image showing NCs-GNPs signal (left) and co-localized NCs-GNPs and PVA signal (right). The signals were separated by linear unmixing using the individual emission spectra of the compounds. The colors in (B) are assigned arbitrarily (not based on wavelength data): red for NCs-GNPs and yellow for PVA. C) CLSM image of NCs-GNPs release from a single microneedle after 30 s in PBS (pH 7.4). NCs-GNPs (red), PVA (yellow) and co-localized signal (orange).

4.4.5. MNs modification and skin penetration studies

The material selection of MNs is crucial for the development of dissolving MNs. PVA is one of the commonly used polymers for the fabrication of dissolving MNs (30-36). To enhance the solubilization of PVA MNs, blending with other polymers such as polyvinylpyrrolidone (PVP) (32) or sugars as sucrose (31, 36) or trehalose (33) has been introduced. Although, the *in vitro* dissolution of the MNs in PBS was very fast in order to release the NPs, this was not the case when the MNs were inserted into human skin. The MNs were still intact (Figure 7A) when removed from hydrated skin 3 h after insertion and the skin showed hollow pores with no sign of NPs release and penetration (Figure 7A). This agrees with Lee *et al*/ who reported that PVP/PVA MNs showed partial dissolution and weakening of the mechanical properties, while keeping structure and shape after insertion in skin. They encapsulated a dye that was deposited in skin after insertion (32). However, in our case this partial dissolution was not sufficient to induce the release of the NPs. This raises the question if the interstitial fluid in the skin is enough to induce fast dissolution of the MNs and subsequent release of the NPs. Leaving the NP-loaded MNs inside the skin for longer times as biocompatible implants will allow for matrix dissolution and NPs release inside the tissue.

Consequently, we introduced an external source of fluid to induce fast dissolution and separation of the MNs from the patch base. This offers the advantages of a short insertion time for increased patient compliance, alongside with prolonging the residence time of MNs in the skin, so dissolution and release of the NPs will be facilitated. In this regard, we have modified the MNs patch by forming 4 channels in the corners of the square patch. These holes allowed the introduction of small volumes of PBS, post-MNs skin insertion, which diffused due to the capillary forces and resulted in fast separation of MNs from the base into the skin (Figure 7B). Both MN1 and MN2 were examined for skin penetration and deposition of NPs into human skin (Figure 7C). The retrieved MNs patch, after 1 min of skin insertion, showed efficient separation of the MNs from the base as shown in Figure 7C. The deposited MNs inside the skin were imaged by CLSM using spectral analysis. Linear unmixing was effective for separating the signal of the NPs from that of skin and PVA. However, the separation of both skin and PVA signal was not possible due to the high similarity in their fluorescence

4. Customized fast-separable microneedles prepared with the aid of 3D printing for nanoparticle delivery

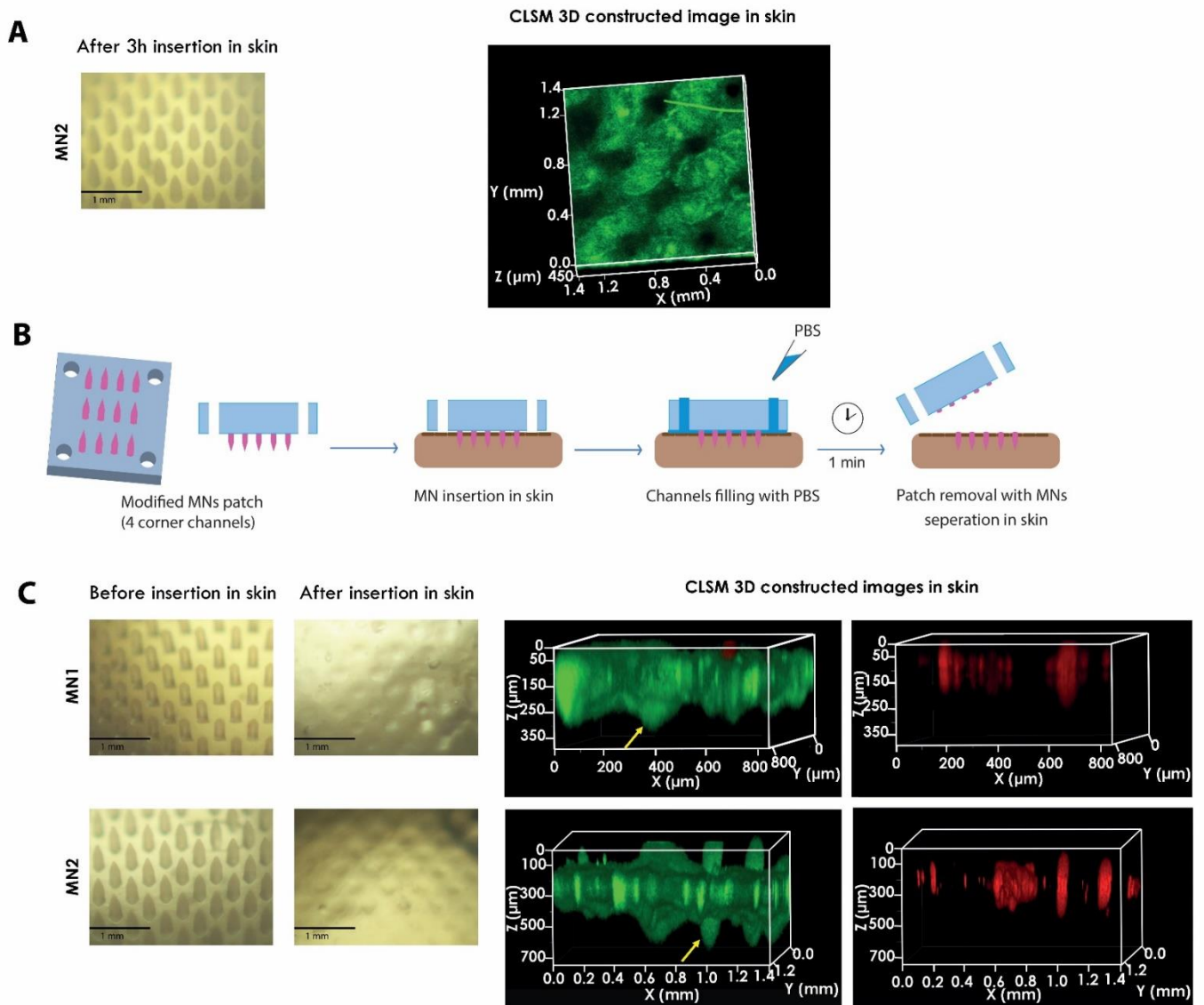


Figure 7. A) Digital images unmodified MN2 patch after 3 h of insertion into skin (left) and reconstructed 3D CLSM image of skin (right) after the removal of the MNs showing empty holes. Skin has been imaged by recording the autofluorescence of skin upon excitation with a 405 nm laser. B) A scheme shows the modification of the MNs patch by forming channels at the 4 corners, then application to human skin punch followed by adding PBS through the channels to induce fast solubilization of the MNs and detachment from the patch base. C) The effect of MNs morphology and modifying the MNs patches on skin penetration of MN1 and MN2, showing the separation of the MNs from the base (left panels) after insertion for 1 min in skin. The inserted MNs have been imaged in skin by CLSM (right panels) where the signal of NCs-GNPs (red), inside the MNs, have been separated from skin and PVA signals (green) by linear unmixing upon excitation at 405 nm. The signal of PVA cannot be separated from that

of skin, due to their similar fingerprint. The MNs can be distinguished from skin by their obvious morphology (referred to by yellow arrows). MN1 and MN2 penetrated the skin to about 300 and 550 μm from the skin surface, respectively.

fingerprint (12). The obtained information allowed us to detect the NPs penetration depth by linear unmixing. Additionally, the depth of the MNs insertion inside the skin could be identified as a result of the well-defined shape of the MNs, which reached 300 and 550 μm for MN1 and MN2, respectively (Figure 7C). The findings support the superior penetration capability of MN2 as tested earlier using texture analyzer. Finally, MNs patch modification with the corner channels proved to be a simple and convenient method to enhance the dissolution and separation of PVA-based MNs from the patch base. This modification can further open the door to test and approve the suitability of variable materials for dissolving MNs fabrication for NPs delivery with minimized administration time to enhance the patient compliance. Additionally, spectral analysis is an attractive method that offers more detailed imaging for MNs in skin depending only on skin autofluorescence with no need for skin pre-treatment.

4.5. Conclusion

As research is highly demanding the development of dissolving MNs to improve their performance for painless transdermal delivery of drug payloads, we, herein, introduce a complete guide for customization of MNs in the lab. Feasible and cost-effective customization of the design to increase skin penetration of MNs was successfully achieved by 3D-printing of master molds using a desktop DLP 3D printer. Deviating from the typical geometries of MNs, pyramidal or conical, researchers are enabled to produce various geometries and test their effectiveness as robust and sharp MNs. The tanto blade-inspired designs proved to be effective for skin penetration without premature fracture as the fracture force was higher than the insertion force. Modifying the aspect ratio of the penetrating front and the tip's dimension and angle rendered the MNs sharper and improved their skin penetration. Further, MNs patches were engineered to speed up the dissolution and separation of MNs from the base into skin. This was achieved by carving 4 channels at the corners of the patch to introduce small amounts of a buffer solution post-skin insertion of the MNs. This fostered fast

detachment of the MNs from the base plate. The connected shorter administration time should ultimately lead to an increased patient compliance. Additionally, loading of the MNs with NIR-emitting NCs-GNPs proved to be an effective imaging probe to visualize NPs distribution within the MNs, their release *in vitro* and their skin penetration. Spectral imaging with linear unmixing could be demonstrated as a new promising tool for simultaneous imaging of the delivery system and skin tissue. Finally, we have introduced new techniques to improve the performance of dissolving MNs and their imaging to serve as a platform to facilitate design customization of MNs by researchers in the lab.

4.6. References

1. Prausnitz MR, Langer R. Transdermal drug delivery. *Nat Biotechnol.* 2008;26(11):1261-8.
2. Levin C, Perrin H, Combadiere B. Tailored immunity by skin antigen-presenting cells. *Hum Vaccin Immunother.* 2015;11(1):27-36.
3. Labouta HI, Schneider M. Interaction of inorganic nanoparticles with the skin barrier: current status and critical review. *Nanomedicine: NBM.* 2013;9(1):39-54.
4. Schneider M, Stracke F, Hansen S, Schaefer UF. Nanoparticles and their interactions with the dermal barrier. *Dermatoendocrinol.* 2009;1(4):197-206.
5. DeMuth PC, Garcia-Beltran WF, Ai-Ling ML, Hammond PT, Irvine DJ. Composite dissolving microneedles for coordinated control of antigen and adjuvant delivery kinetics in transcutaneous vaccination. *Adv Funct Mater.* 2013;23(2):161-72.
6. Park J-H, Allen MG, Prausnitz MR. Biodegradable polymer microneedles: Fabrication, mechanics and transdermal drug delivery. *J Control Release.* 2005;104(1):51-66.
7. Sullivan SP, Murthy N, Prausnitz MR. Minimally invasive protein delivery with rapidly dissolving polymer microneedles. *Adv Mater.* 2008;20(5):933-8.
8. Gittard SD, Ovsianikov A, Monteiro-Riviere NA, Lusk J, Morel P, Minghetti P, et al. Fabrication of polymer microneedles using a two-photon polymerization and micromolding process. *J Diabetes Sci Technol.* 2009;3(2):304-11.
9. Parker ER, Rao MP, Turner KL, Meinhart CD, MacDonald NC. Bulk micromachined titanium microneedles. *J Microelectromech S.* 2007;16(2):289-95.
10. Lee JW, Park J-H, Prausnitz MR. Dissolving microneedles for transdermal drug delivery. *Biomaterials.* 2008;29(13):2113-24.
11. Kochhar JS, Quek TC, Soon WJ, Choi J, Zou S, Kang L. Effect of microneedle geometry and supporting substrate on microneedle array penetration into skin. *J Pharm Sci.* 2013;102(11):4100-8.
12. El-Sayed N, Trouillet V, Clasen A, Jung G, Hollemeyer K, Schneider M. NIR-emitting gold nanoclusters-modified gelatin nanoparticles as a bioimaging agent in tissue. *Adv Healthc Mater.* 2019;8(24):e1900993.

4. Customized fast-separable microneedles prepared with the aid of 3D printing for nanoparticle delivery

13. Labouta HI, Liu DC, Lin LL, Butler MK, Grice JE, Raphael AP, et al. Gold Nanoparticle Penetration and Reduced Metabolism in Human Skin by Toluene. *Pharm Res.* 2011;28(11):2931.
14. Gomaa YA, Garland MJ, McInnes F, El-Khordagui LK, Wilson C, Donnelly RF. Laser-engineered dissolving microneedles for active transdermal delivery of nadroparin calcium. *Eur J Pharm Biopharm.* 2012;82(2):299-307.
15. Stracke F, Weiss B, Lehr C-M, König K, Schaefer UF, Schneider M. Multiphoton Microscopy for the Investigation of Dermal Penetration of Nanoparticle-Borne Drugs. *J Investig Dermatol.* 2006;126(10):2224-33.
16. Thakur RRS, Tekko IA, Al-Shammari F, Ali AA, McCarthy H, Donnelly RF. Rapidly dissolving polymeric microneedles for minimally invasive intraocular drug delivery. *Drug Deliv Transl Res.* 2016;6(6):800-15.
17. Ling M-H, Chen M-C. Dissolving polymer microneedle patches for rapid and efficient transdermal delivery of insulin to diabetic rats. *Acta Biomater.* 2013;9(11):8952-61.
18. Lau S, Fei J, Liu H, Chen W, Liu R. Multilayered pyramidal dissolving microneedle patches with flexible pedestals for improving effective drug delivery. *J Control Release.* 2017;265:113-9.
19. Kim MJ, Park SC, Rizal B, Guanés G, Baek S-K, Park J-H, et al. Fabrication of circular obelisk-type multilayer microneedles using micro-milling and spray deposition. *Front bioeng biotechnol.* 2018;6(54).
20. Korkmaz E, Friedrich EE, Ramadan MH, Erdos G, Mathers AR, Ozdoganlar OB, et al. Tip-loaded dissolvable microneedle arrays effectively deliver polymer-conjugated antibody inhibitors of tumor-necrosis-factor-alpha into human skin. *J Pharm Sci.* 2016;105(11):3453-7.
21. Bediz B, Korkmaz E, Khilwani R, Donahue C, Erdos G, Falo LJ, et al. Dissolvable microneedle arrays for intradermal delivery of biologics: fabrication and application. *Pharm Res.* 2014 31(1):117-35.
22. Sahoo N, Sahoo RK, Biswas N, Guha A, Kuotsu K. Recent advancement of gelatin nanoparticles in drug and vaccine delivery. *Int J Biol Macromol.* 2015;81:317-31.
23. Zhang P. X-ray spectroscopy of gold-thiolate nanoclusters. *J Phys Chem C.* 2014;118(44):25291-9.
24. Li D, Chen Z, Mei X. Fluorescence enhancement for noble metal nanoclusters. *Adv Colloid Interface Sci.* 2017;250:25-39.
25. Larrañeta E, Moore J, Vicente-Pérez EM, González-Vázquez P, Lutton R, Woolfson AD, et al. A proposed model membrane and test method for microneedle insertion studies. *Int J Pharm.* 2014;472(1):65-73.
26. Lhernould MS, Deleers M, Delchambre A. Hollow polymer microneedles array resistance and insertion tests. *Int J Pharm.* 2015;480(1):152-7.
27. Dąbrowska AK, Rotaru GM, Derler S, Spano F, Camenzind M, Annaheim S, et al. Materials used to simulate physical properties of human skin. *Skin RES Technol.* 2016;22(1):3-14.
28. Zimmermann T. Spectral imaging and linear unmixing in light microscopy. *Adv Biochem Eng Biotechnol.* 2005;95:245-65.
29. Mieloszyk J, Drabent R, Siódmiak J. Phosphorescence and fluorescence of poly(vinyl alcohol) films. *J Appl Polym Sci.* 1987;34:1577-80.

4. Customized fast-separable microneedles prepared with the aid of 3D printing for nanoparticle delivery

30. Abdelghany S, Tekko AI, Vora L, Larrañeta E, Permana DA, Donnelly FR. Nanosuspension-based dissolving microneedle arrays for intradermal delivery of curcumin. *Pharmaceutics*. 2019;11(7).
31. Arya JM, Dewitt K, Scott-Garrard M, Chiang Y-W, Prausnitz MR. Rabies vaccination in dogs using a dissolving microneedle patch. *J Control Release*. 2016;239:19-26.
32. Lee IC, He J-S, Tsai M-T, Lin K-C. Fabrication of a novel partially dissolving polymer microneedle patch for transdermal drug delivery. *J Mater Chem B*. 2015;3(2):276-85.
33. Vrdoljak A, Allen EA, Ferrara F, Temperton NJ, Crean AM, Moore AC. Induction of broad immunity by thermostabilised vaccines incorporated in dissolvable microneedles using novel fabrication methods. *J Control Release*. 2016;225:192-204.
34. Nguyen HX, Bozorg BD, Kim Y, Wieber A, Birk G, Lubda D, et al. Poly (vinyl alcohol) microneedles: Fabrication, characterization, and application for transdermal drug delivery of doxorubicin. *Eur J Pharm Biopharm*. 2018;129:88-103.
35. Zhu D, Zhang X, Shen C, Cui Y, Guo X. The maximum possible amount of drug in rapidly separating microneedles. *Drug Deliv Transl Res*. 2019:1-10.
36. Chu LY, Prausnitz MR. Separable arrowhead microneedles. *J Control Release*. 2011;149(3):242-9.

***Chapter 5. Functionalized Theranostic
Nanovaccine for Targeting Dendritic Cells and
Modulation of Immune Response***

*Nesma El-Sayed, Evgeniia Korotchenko, Richard Weiss and Marc
Schneider*

****This chapter has been prepared for publication as a research article***

5. Functionalized Theranostic Nanovaccine for Targeting Dendritic Cells and Modulation of Immune Response

5.1. Abstract

Nanoparticle-based delivery systems have gained interest for enhancing the efficacy and modulating the processing pathways of antigens. In the current study, theranostic gelatin nanoparticles modified by NIR-emitting gold and silver alloy nanoclusters and loaded with ovalbumin (OVA) as a model antigen were developed. Two different designs of the nanoparticles were introduced; positively charged nanoparticles with OVA displayed over the surface (S-NPs) and in the other, OVA is encapsulated in the nanoparticles' matrix and the surface was functionalized by dextran for dendritic cells targeting (Dex-NPs). The nanoparticles showed a particle size of 210 and 305 nm and zeta potential of +25.6 and -23.9 mV, for S-NPs and Dex-NPs, respectively.. Both nanoparticles (Dex-NPs and S-NPs) succeeded to induce maturation of murine bone marrow-derived dendritic cells (BMDCs) evaluated by CD86, CD80, CD40 markers and MHC II. While, Dex-NPs showed no cytotoxicity to BMDC, S-NPs was cytotoxic at a concentration equivalent to 40 µg/ml loaded OVA. The interaction of nanoparticles with BMDCs was quantitatively evaluated by flow cytometry and the nanoparticles internalization by the cells were imaged by confocal laser scanning microscopy. Interestingly, Dex-NPs, rather than S-NPs, modulated the presentation pathway of OVA by dendritic cells to be presented by both MHC II and MHC I to enhance the proliferation of CD4+ and CD8+, respectively. This highlights the potential of the developed nanoparticles for different vaccination purposes; against allergy and viruses/ tumors.

Keywords. Dendritic cell targeting, tumor vaccine, antiviral vaccination, mannose receptors; gelatine nanoparticles; nanotechnology; gold nanoclusters (AuNC)

5.2. Introduction

Vaccines have been an effective tool for protection against diseases by activating and building the memory of the immune cells to fight against microbes and allergens. On the other hand, diseases caused by intracellular pathogens (*e.g.* viruses) and cancer which is caused by endogenous proteins require more focus for development of effective vaccines (1). Antigen-presenting cells (APCs), especially dendritic cells (DCs), can present exogenous and endogenous antigens on major histocompatibility complex (MHC) class II and class I proteins to interact with helper T-cells (T_H , CD4+) and cytotoxic T-cells (CTL, CD8+), respectively. In turn, CD4+ cells activate B-cells to produce antibodies against the antigen, while CD8+ cells attack and destroy the virus-infected or cancer cells (2). Despite being challenging, the development of tumor vaccines using exogenous antigens would be achieved by enhanced uptake of the antigen or cross-presentation, involving escape from lysosomal degradation. So, the antigens are degraded by cytosolic proteasomes as endogenous antigens to be presented on MHC class I molecules (3).

Nowadays, nanoparticles provide an attractive strategy for enhancing antigen delivery. They offer several advantages that overcome the demerits of soluble antigens application (4); 1) antigen encapsulation provides the protection of the antigen against premature undesired degradation, 2) antigen displaying over the nanoparticles' surface mimic the natural way of antigen presentation by the pathogen, 3) controlling and prolonging the release of the antigen to intensify the exposure of the immune system, 4) concomitant loading of the antigen and immune adjuvant is possible to enhance the limited immunogenic effect of most proteins (2, 5). Nanoparticles can contribute to modulating the immune response of antigens by modifying their properties such as size and surface properties. For instance, decorating the nanoparticles surface with targeting moieties for active targeting of APCs is an attractive approach for enhancing antigen receptor-mediated uptake (2). On the other hand, surface modification with poly ethylene imine (PEI), which act as a proton-sponge, can enhance the lysosomal escape of the antigen to the cytosol (6). Both strategies can help to induce antigen presentation to MHC class I and thus the activation of CTL.

Different nanocarriers have been introduced for loading and antigen delivery, among which polymeric nanoparticles have gained interest. Different categories of polymers have been tested including poly (esters), poly (α -hydroxy acids) (5, 7, 8), proteins (9, 10) and polysaccharides (4, 11, 12). Gelatin is a hydrophilic biodegradable polypeptide polymer which provides a good opportunity for encapsulating high payload of antigens under non-harsh conditions (13). This is important to preserve the proteins' conformation which, in turn, is important for their immunogenic activity. Additionally, gelatin is of low immunogenicity (14) which is an important characteristic for an optimal vaccine nanocarrier. Gelatin nanoparticles (GNPs) have been investigated for the delivery of antigens (models) such as tetanus toxoid (15) and ovalbumin (10, 16).

In the current work, we present a theranostic functionalized gelatin nanoparticles for modulating the immune response of OVA as a model antigen. The NIR-emitting gold silver nanoclusters-labelled gelatin nanoparticles were designed as a novel imaging probe. Two designs for OVA loading have been adapted, direct loading and cross linking and the other is surface loading by electrostatic interaction to poly-L-lysine coated GNPs. OVA-encapsulated nanoparticles were further decorated with dextran, which is known for its affinity to a group of receptors on DCs; the DC-SIGN (dendritic cell-specific intercellular adhesion molecule 3-grabbing nonintegrin) family receptors: DC-SIGN (CD209) and L-SIGN (the liver and lymphatic endothelium homologue of DC-SIGN), the mannose receptor (CD206), and langerin (17). The functionalization of the nanoparticles by dextran was tested for its capability to enhance the NP uptake and thus the antigen uptake, bone marrow-derived dendritic cells (BMDCs) activation and induction of both CD4+ and CD8+ proliferation.

5.3. Materials and Methods

5.3.1. Materials

Hydrogen tetrachloroaurate (III) trihydrate ($\text{HAuCl}_4 \cdot 3\text{H}_2\text{O}$), gelatin type B (from bovine skin, gel strength ~ 75 g Bloom), silver nitrate, albumin from chicken egg white, poly-L-lysine hydrobromide (M_w 30,000-70,000), N-(3-dimethylaminopropyl)-N'-ethylcarbodiimide hydrochloride (EDC), N-Hydroxysuccinimide (NHS), dextran

sulphate sodium salt (from *Leuconostoc* species, M_w 100,000), D-(+)- trehalose dihydrate, methanol were all purchased from Sigma Aldrich, Steinheim, Germany. Ovalbumin EndoFit™ (VacciGrade™) was purchased from InvivoGen, Toulouse, France. Fetal bovine serum (FBS), Hank's Balanced Salt Solution (HBSS), 4',6-diamidino-2-phenylindole (DAPI) and Alexa Fluor® 488 conjugate of Concanavalin A were purchased from ThermoFisher scientific, Paisley, United Kingdom. Fixable viability dye eFluor780 was purchased from eBioscience, Thermo Fisher, Paisley, United Kingdom. Antibodies: (CD4-eFluor450 (clone RM4-5), CD8-eFluor506 (clone 53-6.7), CD11c-eFluor450 (clone N418) and CD62L-APC-eFluor780 (clone MEL-14) were purchased from eBioscience, Thermo Fisher, Paisley, United Kingdom. CD11b-PerCp/Cy5.5 (clone M1/70), CD40-APC (clone 3/23), CD86-BV605 (clone GL-1) and MHC-II-Alexa700 (clone M5/114.15.2) were purchased from Biolegend, San Diego, CA, USA. CD80-PE (clone 16-10A1) was purchased ImmunoTools, Friesoythe; Germany). All other chemical used for cell studies, cell culture media, Dulbecco's phosphate-buffered saline (DPBS), 4-(2-hydroxyethyl)-1-piperazineethanesulfonic acid) buffer (HEPES), L-glutamine, penicillin and streptomycin were purchased from Sigma Aldrich, Steinheim, Germany, unless otherwise stated.

5.3.2. Preparation of fluorescent ovalbumin loaded-gelatin nanoparticles

5.3.2.1. Preparation of gold-silver nanoclusters-labelled gelatin

Gold and silver alloy nanoclusters have been synthesized as described earlier (18) by adding HAuCl_4 to gelatin (40 mg/ml) and glutathione (0.7 mM) solution followed by adjusting the pH to 11 using 1N sodium hydroxide. The reaction has been carried out under vigorous mixing at 1000 rpm in a thermomixer (MHR, Hettich Benelux, Geldermalsen, The Netherlands) at 60 °C. 6h after the start of the reaction, a solution of silver nitrate was added in a molar ratio Ag/Au of 0.4, and the reaction continued to 24h. For stopping the reaction, the pH of the mixture was adjusted to 7 using 1N HCl.

5.3.2.2. Preparation of gelatin nanoparticles

The nanoparticles were prepared by two step desolvation method using methanol as antisolvent and crosslinking using a mixture of EDC/NHS for 18h (18). They were

purified by centrifugation (Thermo Fisher Scientific, Osterode am Harz, Germany) at 20,000 g for 1h at 20 °C followed by washing that was repeated 3 times.

5.3.2.3. Ovalbumin surface loading

The pH of gelatin nanoparticles dispersion has been adjusted to 7.4, followed by addition of PLL (1mg/ml) solution and stirring for 1h (weight ratio NP: PLL, 25:1). The nanoparticles have been purified by centrifugation (20,000 g, 30 min, 20 °C) and washing twice with MilliQ® water (MerckMillipore, Darmstadt, Germany). Further interaction with ovalbumin (50 µg/mg of NPs) has been conducted for 1h, followed by purification.

5.3.2.4. Ovalbumin encapsulation and surface functionalization

Direct loading of OVA has been achieved by addition of OVA to gelatin solution after the first precipitation (50 µg OVA / mg of gelatin). The mixture has been cross-linked with EDC/NHS for 18h. The purified nanoparticles have been functionalized by layer-by-layer coating with PLL followed by dextran sulphate (weight ratio of NP : PLL: Dextran, 50: 2: 1.5). For storage and further use, all types of nanoparticles; plain (P-NPs), OVA-surface loaded (S-NPs) and OVA-encapsulated dextran-functionalized nanoparticles (Dex-NPs), have been freeze dried with trehalose with weight ratio of 1:10 (NP: trehalose).

5.3.3. Nanoparticles characterization

The nanoparticles were characterized for size and Zeta potential using Zetasizer (Nano ZS, Malvern Instruments Ltd, Malvern, UK) and morphology using transmission electron microscope (JEOL JEM 2100) operating at a maximum accelerating voltage of 250 kV, after staining of the nanoparticles dispersion with uranyl acetate. The fluorescence spectra of the S-NPs and Dex-NPs has been compared to P-NPs of the same concentration (5 mg/ml) when excited at 405 nm. The spectra have been recorded from 550-850 nm using microplate reader (Infinite M200, Tecan group Ltd, Männedorf, Switzerland).

5.3.4. Entrapment efficiency

For both types of loaded nanoparticles (S-NPs and Dex-NPs), unloaded OVA has been quantified in the supernatants after centrifugation and particles purification against blanks. 5 ml of the nanoparticles dispersion has been centrifuged at 24,000 g for 2h to sediment all the nanoparticles and get clear supernatant. OVA has been analysed for their intrinsic fluorescence at 340 nm when excited at 295 nm using Corning® black 96-well flat bottom plates (Sigma Aldrich, Steinheim, Germany) and microplate reader (Infinite M200, Tecan group Ltd, Männedorf, Switzerland). The sedimented nanoparticles have been further freeze-dried and weighed. The entrapment efficiency (EE %) and loading capacity (LC %) have been calculated as follows:

$$EE \% = \frac{\text{Total amount of OVA added to the preparation } (\mu\text{g}) - \text{Unloaded OVA amount } (\mu\text{g})}{\text{Total amount of OVA added } (\mu\text{g})} \times 100$$

$$LC\% = \frac{\text{Total amount of OVA added to the preparation } (\mu\text{g}) - \text{Unloaded OVA amount } (\mu\text{g})}{\text{Weight of the nanoparticles } (\mu\text{g})} \times 100$$

5.3.5. Release studies

Freeze-dried nanoparticles have been dispersed in 6 ml of phosphate buffer saline (PBS, pH 7.4) to give a final dispersion of 2 mg/ml in 15-ml falcon tubes. They were incubated at 37 °C and shaken at 500 rpm using a thermomixer (MHR, Hettich Benelux, Geldermalsen, The Netherlands). Samples of 400 µl have been withdrawn at different time intervals, centrifuged at 24000 g for 30 minutes and the supernatant was analysed for OVA concentration by measuring the intrinsic fluorescence ($\lambda_{\text{ex}} = 295 \text{ nm}$ and $\lambda_{\text{em}} = 340 \text{ nm}$).

5.3.6. Cellular interaction with bone marrow-derived dendritic cells (BMDCs)

5.3.6.1. Generation of BMDCs

Bone marrow-derived precursors were harvested from femurs/tibias of C57BL/6 mice and were cultured in RPMI 1640 complete medium (10% v/v FBS, 2 mM L-glutamine, 20 ng/mL Granulocyte-macrophage colony-stimulating factor (GM-CSF), 100 U/mL penicillin, 0.1 mg/mL streptomycin). 2×10^6 cells were cultured in 10 mL medium in 10

cm petri dishes (non-treated). At day 3, 10 mL of fresh medium was added and at day 5, 50% of medium was replaced. At day 8, bone marrow-derived DCs (BMDCs) were harvested.

5.3.6.2. Cell viability, nanoparticles uptake and cell activation

3×10^5 (for uptake) or 1×10^5 (for activation) BMDCs were cultured overnight (16h) in 96-well V-bottom plates (non-treated) in 150 μ L of complete medium containing different concentrations of Endofit™ Ovalbumin, or the different gelatine nanoparticle preparations. The next day, cells were washed with DPBS and resuspended in 20 μ L of an anti-CD16/32 hybridoma supernatant (blocking) and incubated on ice. After 5 min, 20 μ L of staining mix consisting of fixable viability dye eFluor 780 (1:1500) (for viability assessment), anti-CD11c-eFluor450 (1:50), anti-CD11b-PerCp-Cy5.5 (1:100), anti-CD40-APC (1:100), anti-CD80-PE (1:100), anti-CD86-BV605 (1:100), and antiMHC II-Alexa700 (1:100) were added. Cells were incubated on ice for 15 min, washed with PBS, 1% BSA, 2mM EDTA, and analysed on a Cytoflex S cytometer (Beckman Coulter Life Science Austria, Vienna, Austria). Gating strategies for cell viability Np uptake and cell activation are described in Figure S18 and S19 (Annex section).

5.3.6.3. Confocal laser scanning microscopy (CLSM)

BMDCs in RPMI 1640 supplemented with 10% FBS, 100 U/ml Pencillin/Streptomycin, 50 μ M β -mercaptoethanol and 20 ng/ml of GM-CSF (1.2×10^6 cells, 200 μ l) were seeded in 8-well imaging chamber and incubated at 37 °C and 5% CO₂ for 24h to attach to the bottom of the well. The medium with unattached cells were removed and replaced with NPs (P-NPs, S-NPs and Dex-NPs) equivalent to 40 μ g/ml OVA. After 6h of incubation, the nanoparticles were removed and the cells were washed 3 times with HBSS buffer. The cells were fixed by incubation with ice cold methanol for 20 min. Then, they were washed and incubated with 3 nM DAPI for 20 min for nucleus staining, followed by washing and incubation with 10 μ g/ml Alexa Fluor® 488 conjugate of Concanavalin A for 20 min for staining the cell membrane. The cells were washed again to remove the excess dye and stored in HBSS at 4 °C to be further examined

with confocal laser scanning microscopy. The cells were excited at 405 nm and emission was recorded from 600-740 nm, followed by signal separation of gold/silver nanoclusters-modified gelatin nanoparticles by linear unmixing using pre-recorded spectral reference to avoid any possible interference from DAPI that is excited at the same wavelength. Then the cells were excited at 405 and 488 nm and the emission was recorded at 410 – 495 nm and 495 -630 nm for detection of DAPI and of Alexa Fluor® 488, respectively. Finally, the recorded images were merged.

5.3.7. Co-culture with naïve T cells

Spleens from OT-I and OT-II mice were aseptically removed and transferred to 40 mm Petri dishes containing 500 μ L DPBS and homogenized using the back of a sterile plunger from a 2 mL syringe. The suspensions were transferred into 1.5 mL Eppendorf tubes. After 3-5 min incubation at room temperature (until debris had settled), the monodisperse cell suspension was transferred into a 15 mL tube, pre-filled with 7 mL of ammonium chloride potassium red blood cell lysis buffer (0.15M NH₄Cl, 10 mM KHCO₃, 0.1 mM Na₂EDTA, pH 7.2-7.4) and incubated for 7 min at room temperature. Tubes were filled up with 6 mL of DPBS, centrifuged for 5 min at 260 g at room temperature, and the pellets were resuspended in 10 mL warm DPBS containing 1 μ M carboxyfluorescein diacetate succinimidyl ester (CFSE). After 10 min incubation at 37 °C, 1 mL of FBS followed by 2 washing steps with T cell medium (RPMI, 10% FBS, 25 mM HEPES, 2 mM L-glutamine, 100 μ g/mL streptomycin, 100 U/mL penicillin). Pellets were resuspended in 0.5 mL T cell medium containing anti-CD62L-eFluor780 (1:150) and anti-CD4-eFluor450 (1:200) or anti-CD8-eFluor506 (1:100) and incubated on ice for 30 min. After washing with DPBS, cells were resuspended in T cell medium and naïve CD4⁺ (OT-II) and CD8⁺ (OT-I) T cells were sorted on a flow cytometry Aria III cell sorter (BD Biosciences, Heidelberg, Germany) based on high expression of CD62L.

15,000 sorted naïve T cells were co-cultured with 5,000 BMDCs in a 50:50 mixture of complete BMDCs and T cell medium in 96-well round bottom plates in the presence or absence of different concentrations of OVA or gelatin nanoparticles. After 4 days of co-culture, cells were harvested, washed with DPBS and resuspended in 30 μ L of staining

mix consisting of fixable viability dye eFluor 660 (1:3000), anti-CD4-eFluor450 (1:200) or anti-CD8-eFluor506. Cells were incubated on ice for 10 min, washed with PBS, 1% BSA, 2 mM EDTA, and analysed on a Cytoflex S cytometer. Gating strategies used for CD4⁺ (OT-II) is shown in Figure S20 (Annex section) and CD8⁺ (OT-I) in Figure S21 (Annex section).

5.3.8. Deposition studies in skin using P.L.E.A.S.E (Precise Lasers Epidermal System) device

Excised human skin was obtained from abdominal plastic surgeries after the approval of the Research Ethic Committee of Saarland, Germany (Ärzttekammer des Saarlandes, Dec. 2008) and permission of the volunteers. The subcutaneous fatty tissue was removed and the skin surface has been cleaned by water. The skin samples were kept in aluminum foils and stored in -20 °C to be used within less than 6 months. Skin punches of 12 mm diameter have been cut and thawed and the surface was cleaned with water. For skin microporation, the punches have been treated with P.L.E.A.S.E.[®] (Precise Lasers Epidermal System) device (Pantec Biosolutions AG, Ruggell, Liechtenstein) using the following parameters: Fluence 56.8 J/cm², 5 pulses/pore, microporation density 10 % and array size of 10 mm. 50 µl of 2 mg/ml fluorescent gold/silver nanoclusters-modified gelatin nanoparticles has been added to the perforated skin surface. The skin punch was carefully transferred to a petri dish and 0.5 ml of PBS was added around the tissue, to keep it hydrated, to be incubated for 1h at 37 °C. After that, the skin surface has been cleaned and the skin has been cut longitudinally into three pieces, embedded in Tissue Tech[©] and instantly frozen using liquid nitrogen. The skin has been longitudinally sectioned by a cryotome and examined by CLSM. Spectral analysis and linear unmixing has been applied to separate NPs from skin signal as described before (18).

5.4. Results and Discussion

5.4.1. Design, preparation and characterization of ovalbumin-loaded nanoparticles

In the current study we have designed nanoparticulate systems with different

properties for the delivery of OVA as a model antigen. We have selected gelatin as biopolymer for the nanoparticle preparation. Gelatin is the product of collagen hydrolysis and is generally regarded as safe (GRAS) by the FDA. It is biodegradable and biocompatible with low or negligible antigenicity (19). It offers high capacity for delivery of biomacromolecules such as antigens (13). Due to its peptide nature, it is rich in functional groups that allow for cross linking and chemical modification of the produced nanoparticles (20).

Gelatin has been modified to be fluorescent by using it as a reducing and stabilizing agent for the synthesis of gold-silver alloy nanoclusters (NCs). The formed nanoclusters are ultra-small structures of size less than 1 nm and emit light in the near infra-red region ($\lambda_{em}= 700$ nm) (18). The nanoclusters-modified gelatin was further utilized for nanoparticle preparation by two-step desolvation method. The first desolvation step was to precipitate the high molecular weight polymer, while getting rid of the low molecular weight chains that can cause irreversible aggregation of the nanoparticles (21). Then, the high molecular weight polymer was used to prepare nanoparticles of uniform particle size. They showed a particle size of 205.7 nm with a polydispersity index (PDI) of 0.14. The particles showed a zeta potential of -6.2 mV (Figure 1B and C).

For loading OVA, two designs have been considered (Figure 1A): surface loading and encapsulation. The surface loading allows for multiple antigen display which mimics the natural display of the antigen by pathogens. Gelatin nanoparticles were cationized by electrostatic interaction with poly L-lysine (PLL) by pH adjustment to 7 where gelatin B is negatively charged (pI 4-5) and PLL is positively charged (pI 9). OVA was loaded by electrostatic interaction with the cationic surface of the nanoparticles. The nanoparticles showed a z-avg for particle size of 210.5 nm, a PDI of 0.102 and the zeta potential of the nanoparticles was +25.6 mV (Figure 1B and C). Even though the OVA is displayed on the surface, the surface charge was positive due to the fact that OVA is only a weak polyanion; not compensating the existing positive surface charge. OVA concentration and interaction time were optimized to 50 $\mu\text{g/ml}$ and 1h respectively to

5. Functionalized Theranostic Nanovaccine for Targeting Dendritic Cells and Modulation of Immune Response

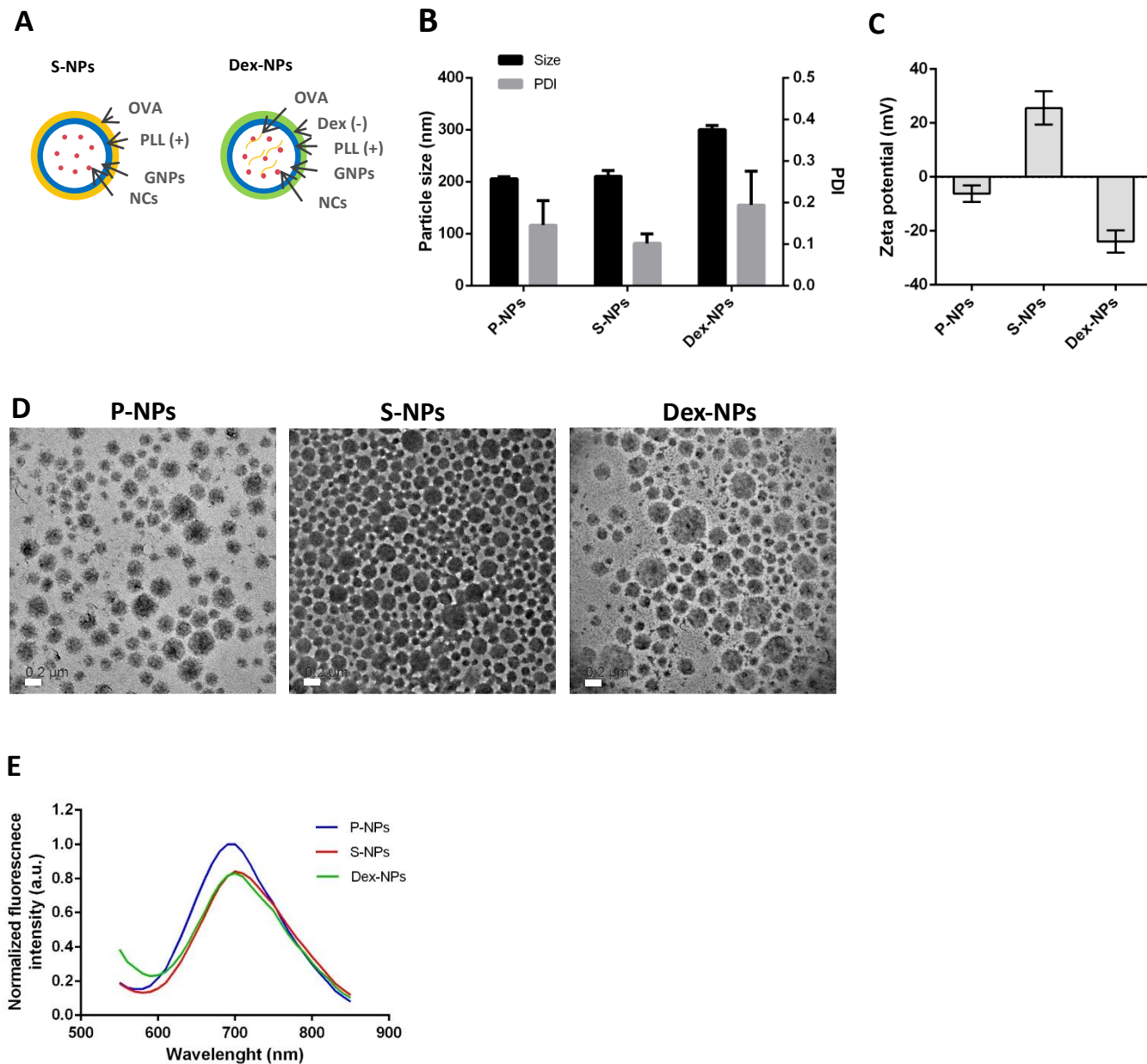


Figure 1. A) Design of ovalbumin (OVA) loaded gelatin nanoparticles (GNPs). The nanoparticles are modified with gold and silver alloy nanoclusters (NCs). S-NPs: OVA is loaded on the surface by electrostatic interaction with the positively charged GNPs (modified by poly-L-lysine (PLL)) and Dex-NPs: OVA is encapsulated within the matrix of GNPs and the NPs surface was functionalized by dextran sulphate, B) particles size (mean \pm SD, n=3) and C) zeta potential measurements (mean \pm SD, n=3) of different NPs (plain GNPs (P-NPs), S-NPs and Dex-NPs), D) Transmission electron microscopy images of the nanoparticles. Scale bar is 0.2 μ m and E) Fluorescence spectra of Dex-NPs and S-NPs in comparison to P-NPs while excitation at 405 nm.

5. Functionalized Theranostic Nanovaccine for Targeting Dendritic Cells and Modulation of Immune Response

obtain nanoparticles with the highest possible loading and colloidal stability at the same time. Lower PLL concentrations with higher loading concentration of OVA and higher interaction times resulted in reduced colloidal stability that can be attributed to reduced surface positive charge or the high density of OVA on the surface that can cause possible protein-protein inter-particle interaction by hydrophobic interactions or Van der Waals forces.

For detection of OVA EE%, the unreacted OVA was analysed by intrinsic fluorescence measurement of the protein. The measured fluorescence ($\lambda_{ex} = 295$ nm and $\lambda_{em} = 340$ nm) is characteristic for the tryptophan residues in OVA (22, 23). This method was selective for OVA with no interference of gelatin (at the tested concentrations), as gelatin lacks tryptophan in its structure (24). Other analysis methods have been used for quantitation of the protein loading in gelatin nanoparticles; for example OVA loading in gelatin nanoparticles was evaluated semi-quantitatively by SDS-PAGE electrophoresis and Coomassie-Blue staining (25), and bovine serum albumin (BSA) loading in gelatin nanoparticles has been detected using HPLC method (26). However, the current developed method represents a simple and selective method for detection of tryptophan-containing proteins (such as OVA and BSA) in presence of gelatin. The analysis revealed that the EE% of OVA in S-NPs was $83.58 \pm 8.14\%$. And the LC% was $3.86 \pm 0.66\%$.

On the other hand, encapsulation can protect the antigen from degradation. For OVA encapsulation in gelatin nanoparticles, OVA was added to gelatin before the second precipitation step. The nanoparticles were cross-linked by EDC/NHS mixture which is a zero-length cross-linker that conjugates the amino and carboxylic groups of the amino acids (27). The surface of the nanoparticles was functionalized by dextran for targeting DCs. Dextran is a biocompatible, linear polysaccharides of glucose with a prevalence of 1,6-linked units. Dextran is taken up by APCs such as DCs and macrophages due to interaction with specific receptors: the family of C-type lectins, namely mannose receptors (MRs), dendritic adhesion cell (DCs)-specific molecule-3 intercellular (ICAM-3)-grabbing nonintegrin (DC-SIGN), the liver and lymphatic

endothelium homologue of DC-SIGN (L-SIGN), and langerin (17). The surface functionalization was achieved by electrostatic interaction of dextran sulphate to PLL-modified gelatin nanoparticles. This was proven by measuring zeta potential that was -23.9 mV (Figure 1C). Encapsulation of OVA in GNPs resulted in larger particle size (Z-avg 300.5 nm, PDI 0.194) compared to the surface loading (Figure 1B). This size of nanoparticles is suitable for targeting resident DCs in skin for transcutaneous vaccination. Nanoparticles size can manipulate the immune response, where nanoparticles of size 20-200 nm can drain passively to lymph nodes to be taken up by DCs there and larger particles are preferentially taken up by DCs at site of application (28). Freeze drying of both formulations in presence of trehalose (1:10 by weight NP: trehalose) preserved the size and zeta potential after reconstitution. The EE% of OVA was $72.9 \pm 14.9\%$ and the LC% was $5.34 \pm 1.84\%$, which were detected indirectly by measuring the concentration of the unloaded OVA in supernatants after nanoparticles centrifugation by fluorimetric analysis.

TEM imaging of the nanoparticles (Figure 1D): plain (P-NPs), surface-loaded (S-NPs), and OVA-encapsulated with surface functionalization by dextran (Dex-NPs) showed spherical morphology for all formulations. Dex-NPs showed larger nanoparticles compared to P-NPs and S-NPs which supports the results obtained by photon-correlation spectroscopy. Furthermore, the images showed the presence of NCs in all nanoparticles. The fluorescence properties were evaluated for all formulations upon excitation at 405 nm by recording the fluorescence spectra. It was found, that the loading OVA is negligibly affecting the fluorescence of GNPs (Figure 1E).

5.4.2. Ovalbumin release

OVA release from both S-NPs and Dex-NPs was performed in PBS, pH 7.4 over specified time intervals for a period of 3 and 60 days for S-NPs and Dex-NPs, respectively. S-NPs showed a burst release (31 %) after 1h followed by a slower release over 3 days to reach 71 % at the end of the release study (Figure 2A). This can be attributed to the surface loading of OVA post-preparation of the nanoparticles

5. Functionalized Theranostic Nanovaccine for Targeting Dendritic Cells and Modulation of Immune Response

and the electrostatic forces that binds OVA to NPs. On the other hand, Dex-NPs showed a slow release profile, with no burst effect, that reached just 8.4 % after 60 days (Figure 2B). This proves the cross-linking of OVA and gelatin during NP formation. This can provide a protection for the antigen from environmental conditions till the uptake of the NPs by APCs. Then the NPs can be processed within the cells to release the OVA epitope.

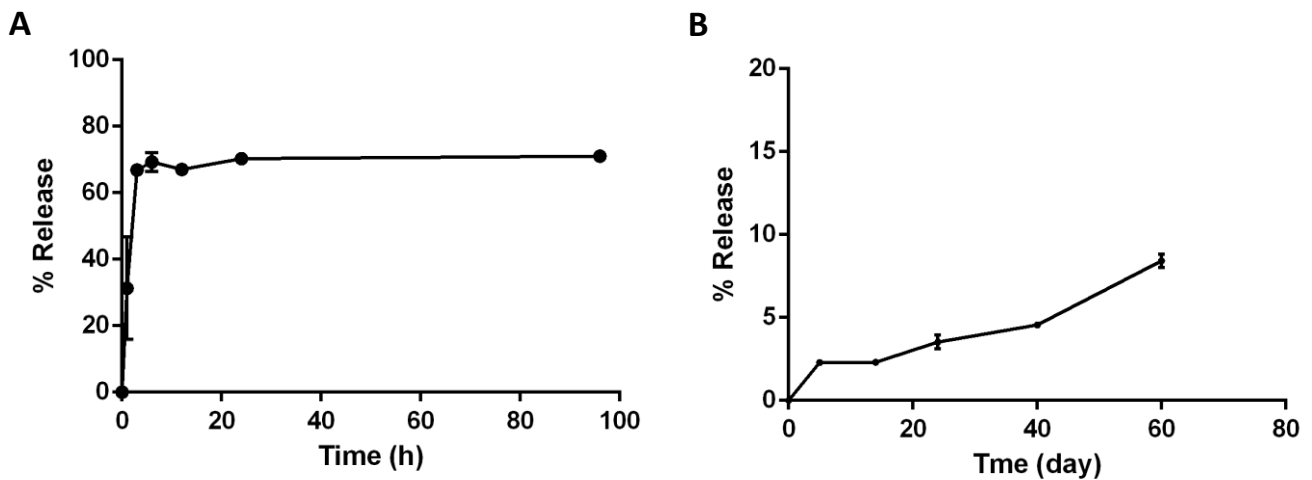


Figure 2. OVA release from nanoparticles at phosphate buffer saline (PBS) of pH 7.4 at 37° C at different time intervals: A) from S-NPs and B) Dex-NPs. (mean \pm SD, n=3)

5.4.3. Interaction of nanoparticles with BMDCs

Cytotoxicity of the different NPs have been evaluated using BMDCs (Figure 3A). Both Dex-NPs and P-NPs caused no cytotoxicity at all tested concentrations of the NPs equivalent to 10-40 μ g/ml of OVA. Whereas, S-NPs showed cytotoxicity (a reduction in cell viability by 38%) when the cells exposed to NPs concentration equivalent to 40 μ g/ml of OVA. This can be attributed to the positive charge of the NPs that have been previously reported for their potential cytotoxic effect (29).

Maturation of BMDC have been assessed by flow cytometry by detecting the upregulation of CD40, CD80 and CD86 maturation markers (Figure 3B, C and D)(30, 31), and MHC class II for antigen presentation to CD4+ (Figure 3E) (31, 32). Dex-NPs

5. Functionalized Theranostic Nanovaccine for Targeting Dendritic Cells and Modulation of Immune Response

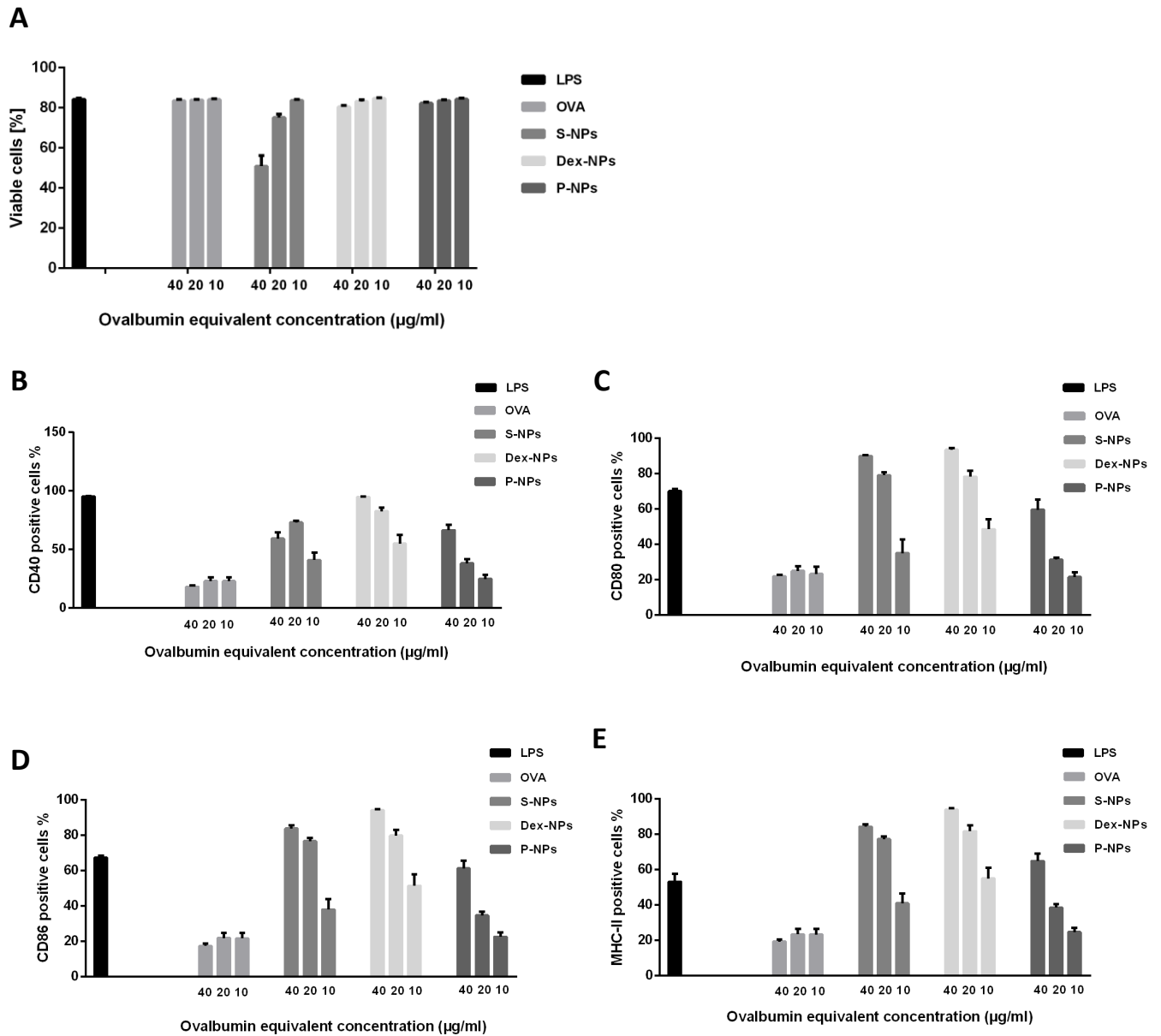


Figure 3. A) Cytotoxicity of the nanoparticles at different concentrations compared to OVA and lipopolysaccharides (LPS) represented as the % of viable bone marrow dendritic cells (BMDCs). Maturation and activation of BMDCs evaluated by measuring B) CD40, C) CD80, D) CD86 and E) MHC-II. (mean \pm SD, n=3)

5. Functionalized Theranostic Nanovaccine for Targeting Dendritic Cells and Modulation of Immune Response

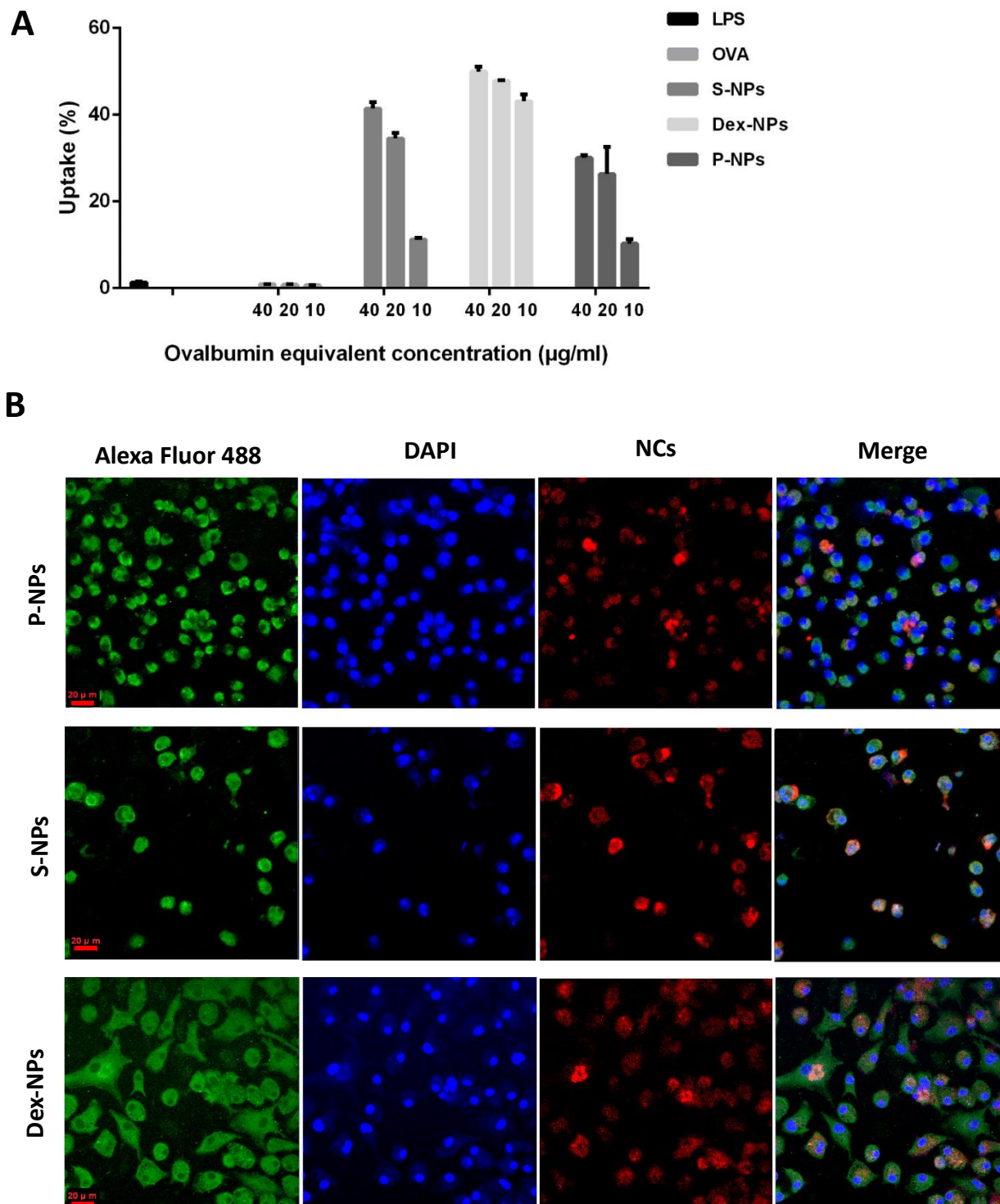


Figure 4. A) uptake/interaction of NPs with BMDCs analyzed by flow cytometry (mean \pm SD, n=3) and B) confocal laser scanning microscopy images of NPs internalization by BMDCs, blue: DAPI staining the nucleus (ex at 405 nm, em 410 – 495 nm), green: Concanavalin A - Alexa Flour 488 staining the cell membrane and cytoplasm (ex at 488 nm, em 495 - 630 nm) and red: NCs-modified GNPs (ex at 405, em 600-740 nm). Scale bar is 20 μ m.

showed superiority in the ability to induce DCs maturation compared to S-NPs and P-NPs, where P-NPs showed the lowest influence. All formulations showed concentration-dependent response in term of DCs maturation, and at the same time a more pronounced effect than the soluble antigen.

Cellular interaction/uptake with NPs was examined quantitatively using flow cytometry (Figure 4A), which provides information about the total number of cells interacting with NPs by measuring the fluorescence of NPs. Dex-NPs showed superiority in uptake by BMDCs over S-NPs and P-NPs for all the tested concentration NPs concentrations equivalent to 10-40 $\mu\text{g/ml}$ OVA. Higher % uptake of Dex-NPs of 43.5% was noticed (compared to S-NPs (10.8 %) and P-NPs (11%)) when the cells were treated with NPs concentration equivalent to 10 $\mu\text{g/ml}$ OVA. This indicates the significance of nanoparticles decoration with dextran, as a potential polyscharride that can target receptors expressed on dendritic cells such as mannose receptors, for enhancing the uptake of the nanoparticles.

BMDCs incubated with NPs equivalent to 40 $\mu\text{g/ml}$ OVA were visualized by CLSM to detect the uptake and localization of NPs (Figure 4B), which cannot be predicted from the flow cytometry measurements. It has been found that Dex-NPs are internalized within the cells proofing the uptake of NPs. S-NPs showed in some cells concentration of the NPs on the cellular membrane due to the electrostatic interaction between the positively charged NPs and the negatively charged cell membrane. For P-NPs, some NP agglomeration have been shown to be outside the cells, being connected to a lower uptake.

5.4.4. Effect of nanoparticles on naïve T cells proliferation

To investigate the processing pathway of the OVA and evaluate the cross-presentation efficiency after delivery using S-NPs and Dex-NPs, the NPs were incubated with BMDCs and CD8⁺ T cells (OT-I cells) or CD4⁺ T cells (OT-II cells), and the proliferation of naïve T cells was evaluated (Figure 5A and B). Serial dilutions of NPs were tested to provide OVA concentrations of 0.08-10 $\mu\text{g/ml}$. Soluble antigen and P-NPs were

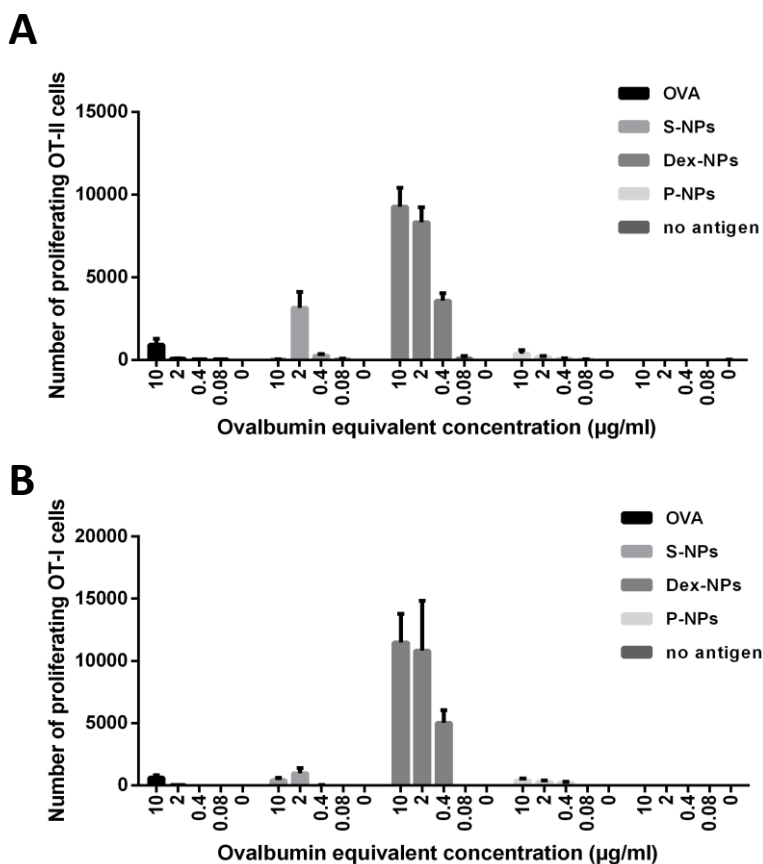


Figure 5. Effect of NPs on the antigen presentation pathway investigated as the proliferation of naïve T cells co-cultured with BMDCs and NPs (mean \pm SD, $n=3$). A) Effect on proliferation of OT II (CD4+, helper T cells, Th) and B) OT I (CD8+, cytotoxic T cells, CTL).

ineffective to stimulate the proliferation of neither CD8+ nor CD4+ cells. S-NPs with 2 $\mu\text{g/ml}$ OVA resulted in enhancement of CD4+ proliferation compared to soluble OVA. However, higher concentration of S-NPs failed to induce the proliferation of CD4+, this can be attributed to the possible cytotoxic effect of the positively charged nanoparticles on T cells, while no proliferation of CD8+ cells was observed. However, PEI-functionalized nanoparticles were reported to induce cross presentation of antigen (6), PLL-functionalized nanoparticles were not efficient in antigen cross presentation as they failed to activate CD8+ cells. Interestingly, Dex-NPs efficiently enhanced the proliferation of both CD8+ and CD4+. This means that OVA was successfully

presented along both MHC class I and II pathways, respectively. This can be attributed to the potential protection of OVA in the endosome that turned into efficient cross-presentation of OVA (30). Consequently, Dex-NPs present a promising nanovaccine for allergy vaccination as well as anti-viral and tumor vaccination.

5.4.5. Transcutaneous delivery of nanoparticles using P.L.E.A.S.E technology

Due to the richness of skin in APCs, it is an attractive route for vaccine administration (33). However, skin is a firm tissue and impermeable barrier that resists the permeation of molecules larger than 500 Da (34). Stratum corneum is the keratinized outermost layer of the skin that represents the real physical barrier (35) and also efficiently prevents nanoparticles' penetration (36, 37). Laser skin microporation is a promising, reliable and painless technique for overcoming the stratum corneum barrier and delivering macromolecules and nanoparticles into viable skin. Pulsed-red laser light is applied to skin, where the water in the tissue absorbs the light energy and evaporates fast disrupting the tissue, forming pores at the site of application. P.L.E.A.S.E.® (Precise Laser Epidermal System) device is developed by Pantec Biosolutions for controlled skin microporation. The device employs a diode-pumped Erbium:yttrium-aluminium-garnet (ER: YAG) laser at wavelength 2.94 μm which is the absorption peak of water molecules. The device allows for controlling the number of pores per unit area as well as the depth of the micropores by controlling the laser fluence (energy per unit area) and the number of pulses (33). The device was applied to human skin with fluence 56.8 J/cm^2 that was efficient to create micropores as shown in Figure 6A. Examination of skin longitudinal sections by CLSM after nanoparticles application revealed the following: the formation of the micropores through the epidermis leaving the dermis beneath intact and the applied nanoparticles appeared to be deposited and lining the pores (Figure 6B). Consequently, the technology is a potential promising method for delivering nanoparticles loaded with antigens to dendritic cells in epidermis and dermis for effective vaccination.

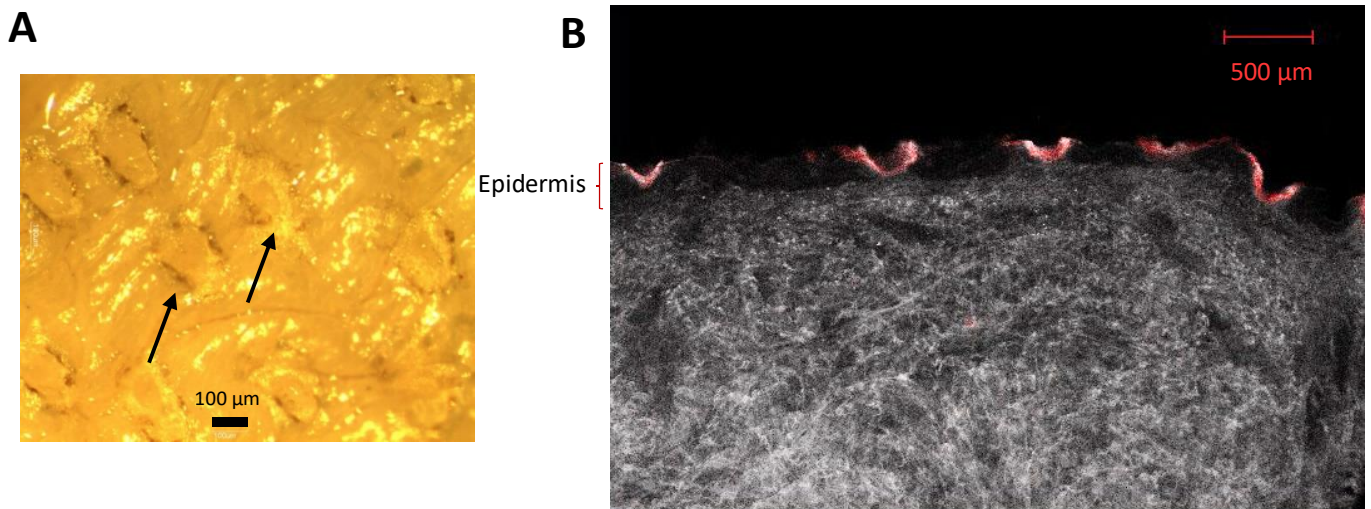


Figure 6. Laser skin microporation of full thickness human skin using P.L.E.A.S.E.[®] (Precise Laser Epidermal System) device. Skin area of 10 mm size was treated with infra-red laser at fluence 56.8 J/cm² with microporation density 10 % A) magnified images of skin surface after microporation and the micropores are indicated by arrows. B) CLSM image of longitudinal skin section showing the micropores in the epidermis layer with NPs depositions in the pores indicated by red fluorescence.

5.5. Conclusion

Theranostic gelatin nanoparticles for delivery of OVA as model antigen were developed. The imaging agent was a novel NIR-emitting gold and silver alloy nanoclusters that were synthesized in presence of gelatin and thus attached to gelatin backbone. Different designs of the nanoparticles were introduced to serve different functions and their effect on the antigen processing pathway by dendritic cells have been investigated. Positively charged nanoparticles displaying the antigen over the surface resulted in fast release of the antigen, efficient uptake by BMDCs and antigen presentation to MHC II that enhance the proliferation of CD4⁺. However, the cytotoxicity of the nanoparticles limited their working and efficient concentration range. On the other hand, encapsulation of OVA within gelatin nanoparticles and cross-linking resulted in slow release of the antigen. This can help to avoid pre-mature release of the antigen before being taken up by dendritic cells with potential protection of OVA against degradation. Functionalization of the nanoparticles by dextran to target

mannose receptors in dendritic cells, resulted in high uptake of the particles, which was evaluated by flow cytometry analysis and confirmed by CLSM imaging. Successfully, the nanoparticles modulated the pathway of antigen presentation to be displayed by both MHC II and MHC I to result in enhanced proliferation of both CD4+ and CD8+, respectively. The developed formulation represents a promising approach for vaccine development against allergy as well as viruses/tumors.

5.6. References

1. Salem AK. Nanoparticles in vaccine delivery. *AAPS J.* 2015;17(2):289–91.
2. Paulis LE, Mandal S, Kreutz M, Figdor CG. Dendritic cell-based nanovaccines for cancer immunotherapy. *Curr Opin Immunol.* 2013;25(3):389-95.
3. Embgenbroich M, Burgdorf S. Current concepts of antigen cross-presentation. *Front Immunol.* 2018;9(1643).
4. Gregory A, Williamson D, Titball R. Vaccine delivery using nanoparticles. *Front Cell Infect Mi.* 2013;3(13).
5. Mönkäre J, Pontier M, van Kampen EEM, Du G, Leone M, Romeijn S, et al. Development of PLGA nanoparticle loaded dissolving microneedles and comparison with hollow microneedles in intradermal vaccine delivery. *Eur J Pharm Biopharm.* 2018;129:111-21.
6. Chen J, Li Z, Huang H, Yang Y, Ding Q, Mai J, et al. Improved antigen cross-presentation by polyethyleneimine-based nanoparticles. *Int J Nanomedicine.* 2011;6:77–84.
7. Rietscher R, Schröder M, Janke J, Czaplowska J, Gottschaldt M, Scherließ R, et al. Antigen delivery via hydrophilic PEG-b-PAGE-b-PLGA nanoparticles boosts vaccination induced T cell immunity. *Eur J Pharm Biopharm.* 2016;102:20-31.
8. Rietscher R, Czaplowska JA, Majdanski TC, Gottschaldt M, Schubert US, Schneider M, et al. Impact of PEG and PEG-b-PAGE modified PLGA on nanoparticle formation, protein loading and release. *Int J Pharm.* 2016;500(1):187-95.
9. da Silva NIO, Salvador EA, Rodrigues Franco I, de Souza GAP, de Souza Morais SM, Prado Rocha R, et al. Bovine serum albumin nanoparticles induce histopathological changes and inflammatory cell recruitment in the skin of treated mice. *Biomed Pharmacother.* 2018;107:1311-7.
10. Lin S-F, Jiang P-L, Tsai J-S, Huang Y-Y, Lin S-Y, Lin J-H, et al. Surface assembly of poly(I:C) on polyethyleneimine-modified gelatin nanoparticles as immunostimulatory carriers for mucosal antigen delivery. *J Biomed Mater Res B.* 2019;107(4):1228-37.
11. Gao P, Xia G, Bao Z, Feng C, Cheng X, Kong M, et al. Chitosan based nanoparticles as protein carriers for efficient oral antigen delivery. *Int J Biol Macromol.* 2016;91:716-23.
12. Zhang C, Shi G, Zhang J, Song H, Niu J, Shi S, et al. Targeted antigen delivery to dendritic cell via functionalized alginate nanoparticles for cancer immunotherapy. *J Control Release.* 2017;256:170-81.
13. Sahoo N, Sahoo RK, Biswas N, Guha A, Kuotsu K. Recent advancement of gelatin nanoparticles in drug and vaccine delivery. *Int J Biol Macromol.* 2015;81:317-31.

14. Tondera C, Hauser S, Krüger-Genge A, Jung F, Neffe AT, Lendlein A, et al. Gelatin-based hydrogel degradation and tissue interaction in vivo: insights from multimodal preclinical imaging in immunocompetent nude mice. *Theranostics*. 2016;6(12):2114–28.
15. Sudheesh MS, Vyas SP, Kohli DV. Nanoparticle-based immunopotential via tetanus toxoid-loaded gelatin and aminated gelatin nanoparticles. *Drug Deliv* 2011;18(5):320-30.
16. Du G, Hathout RM, Nasr M, Nejadnik MR, Tu J, Koning RI, et al. Intradermal vaccination with hollow microneedles: A comparative study of various protein antigen and adjuvant encapsulated nanoparticles. *J Control Release*. 2017;266:109-18.
17. Pustynnikov S, Sagar D, Jain P, Khan ZK. Targeting the C-type lectins-mediated host-pathogen interactions with dextran. *J Pharm Pharm Sci* 2014;17(3):371 - 92.
18. El-Sayed N, Trouillet V, Clasen A, Jung G, Hollemeyer K, Schneider M. Nir-emitting gold nanoclusters–modified gelatin nanoparticles as a bioimaging agent in tissue. *Adv Healthc Mater*. 2019;8(24):1900993.
19. Smith AM, Moxon S, Morris GA. Biopolymers as wound healing materials. In: Ågren MS, editor. *Wound Healing Biomaterials*: Woodhead Publishing; 2016. p. 261-87.
20. Krishnamachari Y, Geary SM, Lemke CD, Salem AK. Nanoparticle delivery systems in cancer vaccines. *Pharm Res*. 2011;28(2):215-36.
21. C. J. Coester KLHVBJK. Gelatin nanoparticles by two step desolvation a new preparation method, surface modifications and cell uptake. *J Microencapsul*. 2000;17(2):187-93.
22. Lakowicz JR. Protein Fluorescence. *Principles of Fluorescence Spectroscopy* Springer, Boston, MA; 1999. p. 445-86.
23. Onda M, Hirose M. Refolding mechanism of ovalbumin: investigation by using a starting urea-denatured disulfide isomer with mispaired CYS367-CYS382. *J Biol Chem*. 2003;278(26):23600-9.
24. Moskowitz RW. Role of collagen hydrolysate in bone and joint disease. *Semin Arthritis Rheu*. 2000;30(2):87-99.
25. Zwioerek K. *Gelatin nanoparticles as delivery system for nucleotide-based drugs*: Ludwig Maximilians University of Munich; 2006.
26. Baseer A, Koenneke A, Zapp J, Khan SA, Schneider M. Design and characterization of surface-crosslinked gelatin nanoparticles for the delivery of hydrophilic macromolecular drugs. *Macromol Chem Phys*. 2019;220(18):1900260.
27. Conde J, Dias JT, Grazú V, Moros M, Baptista PV, de la Fuente JM. Revisiting 30 years of biofunctionalization and surface chemistry of inorganic nanoparticles for nanomedicine. *Front Chem*. 2014;2(48).
28. Manolova V, Flace A, Bauer M, Schwarz K, Saudan P, Bachmann MF. Nanoparticles target distinct dendritic cell populations according to their size. *Eur J Immunol*. 2008;38(5):1404-13.
29. Fröhlich E. The role of surface charge in cellular uptake and cytotoxicity of medical nanoparticles. *Int J Nanomedicine*. 2012;7:5577-91.
30. Chang TZ, Stadmler SS, Staskevicius E, Champion JA. Effects of ovalbumin protein nanoparticle vaccine size and coating on dendritic cell processing. *Biomater Sci*. 2017;5(2):223-33.

31. Yong M, Mitchell D, Caudron A, Toth I, Olive C. Expression of maturation markers on murine dendritic cells in response to group A streptococcal lipopeptide vaccines. *Vaccine*. 2009;27(25):3313-8.
32. Weenink SM, Gautam AM. Antigen presentation by MHC class II molecules. *Immunol Cell Biol*. 1997;75(1):69-81.
33. Weiss R, Hessenberger M, Kitzmüller S, Bach D, Weinberger EE, Krautgartner WD, et al. Transcutaneous vaccination via laser microporation. *J Control Release*. 2012;162(2):391-9.
34. Bos JD, Meinardi MM. The 500 Dalton rule for the skin penetration of chemical compounds and drugs. *Exp Dermatol*. 2000;9(3):165-9.
35. Banerjee R. Overcoming the stratum corneum barrier: a nano approach. *Drug Deliv Transl Res*. 2013;3(3):205-8.
36. Labouta HI, Schneider M. Interaction of inorganic nanoparticles with the skin barrier: current status and critical review. *Nanomed-Nanotechnol*. 2013;9(1):39-54.
37. Schneider M, Stracke F, Hansen S, Schaefer UF. Nanoparticles and their interactions with the dermal barrier. *Dermatoendocrinol*. 2009;1(4):197-206.

Chapter 6. Summary, Conclusion and Outlook

6. Summary, Conclusion and Outlook

In the current research, we have developed theranostic nanoparticles for antigen delivery and modulation of immune response. Delivering nanoparticles transcutaneously is a promising route of administration, due to the richness of skin in immune cells. Accordingly, through the thesis we have been working on the following:

- Development of the imaging agent that provides the ability to be incorporated into gelatin drug carriers for cell and tissue imaging.
- Development of dissolving microneedles for the nanoparticles delivery into skin
- Design of nanoparticle formulations for antigen delivery and modulation of immune response

Gold nanoclusters as a novel imaging agent have been synthesized using gelatin, a well-established pharmaceutical compound, as a reducing and templating agent. The reaction conditions were optimized in terms of gold and gelatin concentration and pH. Further, the reaction was assisted by the addition of glutathione to be a source of the reducing thiol groups. This resulted in 50-nm red shift of the nanoclusters' fluorescence to be 700 nm, giving the advantage of imaging in the near infra-red region, within the optical window of tissues. Additionally, the stability of the nanoclusters fluorescence against pH and enzymatic degradation have been fortified. For enhancement of the fluorescence intensity, silver ions have been used to modify the nanoclusters either by doping during or post-synthesis of the clusters. This resulted in 3-fold enhancement of the fluorescence quantum yield. The structure of the nanoclusters have been studied using X-Ray Photoelectron Spectroscopy (XPS) and correlated to their properties. The selected formulation of gold and silver alloy nanoclusters allowed to preserve the integrity of gelatin as examined by Fourier transform infrared spectrometry (FT-IR) and matrix-assisted laser desorption/ionization time of flight mass spectrometry (MALDI-TOF MS). Further, the fluorescent gelatin was used to synthesize gelatin nanoparticles using two-step desolvation method and N-(3-Dimethylaminopropyl)-N'-ethylcarbodiimide hydrochloride (EDC) as a zero-length cross linker in presence of N-Hydroxysuccinimide (NHS). The nanoparticles were introduced in skin by dissolving

microneedles and imaged simultaneously with skin autofluorescence by confocal laser scanning microscopy (CLSM) using spectral analysis and linear unmixing. Introduction of the nanoparticles into skin was achieved using dissolving microneedles.

Dissolving microneedles with new design have been developed for the delivery of the nanoparticles into skin. 3D-printing has been used as a cost-effective method to build a positive master for the preparation of microneedle patches. Microneedle designs inspired from the Japanese sword 'tanto-blade' have been produced successfully using a desktop DLP 3D printer. The positive molds were used to prepare a negative replica by polydimethylsiloxane (PDMS) casting. The latter was used for molding microneedles made of polyvinyl alcohol (PVA)/sucrose and loaded with the gold and silver alloy nanoclusters-modified gelatin nanoparticles. The force required for microneedles insertion in a skin surrogate was as low as 10.6 N. They were robust enough for insertion as the fracture force required to break or compress the microneedles' tips was twice that of the insertion force. The fluorescent particles were imaged by CLSM *in vitro* to investigate the distribution of the nanoparticles in the microneedles' matrix and their release in phosphate buffer saline. Further the microneedles patch was modified by carving a channel in each of the four corners of the square patch. Small volume of buffer was added post-insertion in skin, and resulted in fast separation of the microneedles from the base into skin. This resulted in decreasing the application time to 1 min. Imaging of the microneedles in human skin revealed that they can reach a depth of 550 μm . After being succeeded in setting up a system to deliver the fluorescent drug carriers across the stratum corneum, the loading of the carriers with relevant macromolecular drug was further investigated.

The fluorescent gold and silver nanoclusters-modified gelatin nanoparticles were loaded with ovalbumin as a model antigen. Two different designs of the nanoparticles have been introduced:

- 1) S-NPs: Ovalbumin was surface loaded post-synthesis of the nanoparticles. This was achieved by electrostatic interaction of ovalbumin to positively charged poly-L-lysine modified gelatin nanoparticles. The nanoparticles showed particle sizes with a z-avg of 210.5 nm, poly dispersity index (PDI) of 0.102 and zeta potential of +25.6 mV.

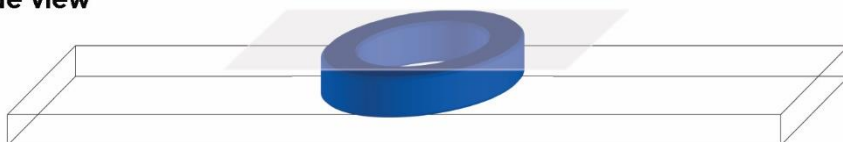
- 2) Dex-NPs: Ovalbumin was encapsulated within the gelatin nanoparticles' matrix and cross linked using EDC/NHS. The surface of the nanoparticles was functionalized by dextran to potentially target the mannose-receptors on dendritic cells. This was achieved by the electrostatic interaction between dextran sulphate and poly-L-lysine modified gelatin nanoparticles. The nanoparticles showed particle sizes with a z-avg of 300.5 nm, PDI of 0.194 and zeta potential of -23.9 mV.

The release of ovalbumin was tested from both of the nanoparticles in PBS, where S-NPs showed a burst release followed by slower release phase, while Dex-NPs showed no burst effect but slow extended release. Dex-NPs showed no cytotoxicity toward bone marrow-derived dendritic cells (BMDCs), while S-NPs were cytotoxic at higher concentration equivalent to 40 µg/ml ovalbumin. The nanoparticles uptake was quantitatively evaluated by flow cytometry to show superior uptake of Dex-NPs by BMDCs compared to S-NPs and plain gelatin nanoparticles (P-NP). CLSM imaging confirmed the internalization of Dex-NPs by BMDCs. Both Dex-NPs and S-NPs had the ability to induce the activation of BMDCs as evaluated by CD40, CD80 and CD86 activation markers and MHC class II molecules. The effect of the nanoparticles on the proliferation of naïve T cells co-cultured with BMDCs have been studied. Dex-NPs have showed the ability to enhance the proliferation of both CD4+ and CD8+. This can be attributed to the high uptake of the nanoparticles and/or the ability of the nanoparticles to induce cross-presentation of the antigen by protecting the antigen from the lysosomal degradation, so it can escape to the cytosol. Thus, these nanoparticles have great potential to be used as effective vaccine against allergy, viruses and tumors.

For transcutaneous delivery of gelatin nanoparticles, microneedles were investigated and also preliminary studies have been done during the thesis research work using the P.L.E.A.S.E technology on human skin. The device induced micropores formation, where the applied gelatin nanoparticles deposited in, as examined by CLSM. Finally, Dex-NPs are promising theranostic nanovaccines that can be further applied for *in vivo* pre-clinical studies. The nanoparticles can be introduced transcutaneously by microneedles or skin laser microporation using P.L.E.A.S.E (Precise Lasers Epidermal System) device.

Annex

Side view



Top view

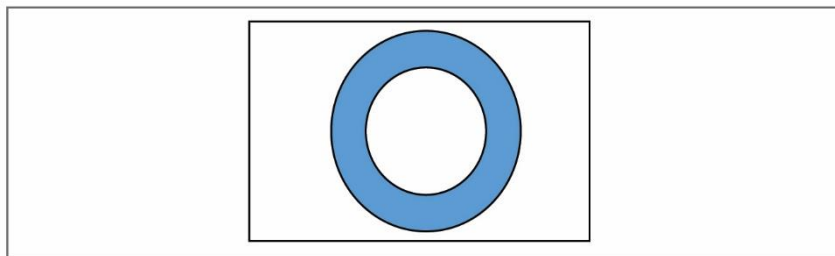


Figure S1. A scheme representing the microscopic chamber setup for skin examination using confocal microscopy, where the skin is replaced inside a ring over a PBS buffer-soaked filter paper and covered by a coverslip.

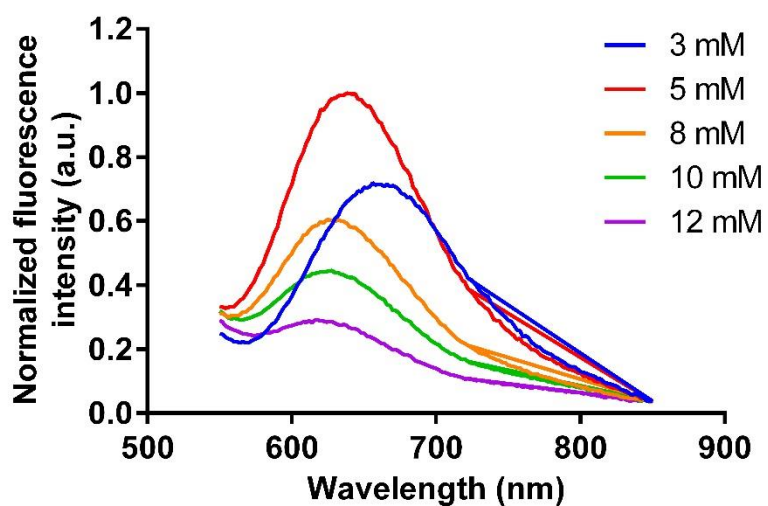


Figure S2. Emission spectra resulted from the interaction of different gold chloride concentrations with gelatin type B (2% w/v).

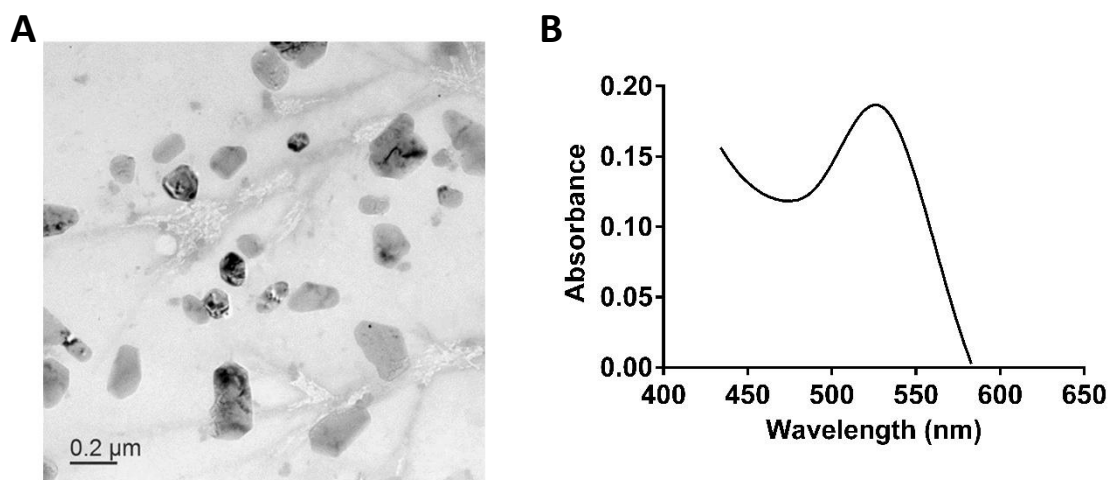


Figure S3. A) TEM image of gold nanoparticles formed upon the interaction of 30 mM Au with gelatin 2 % w/v, B) Plasmon resonance of the formed gold nanoparticles.

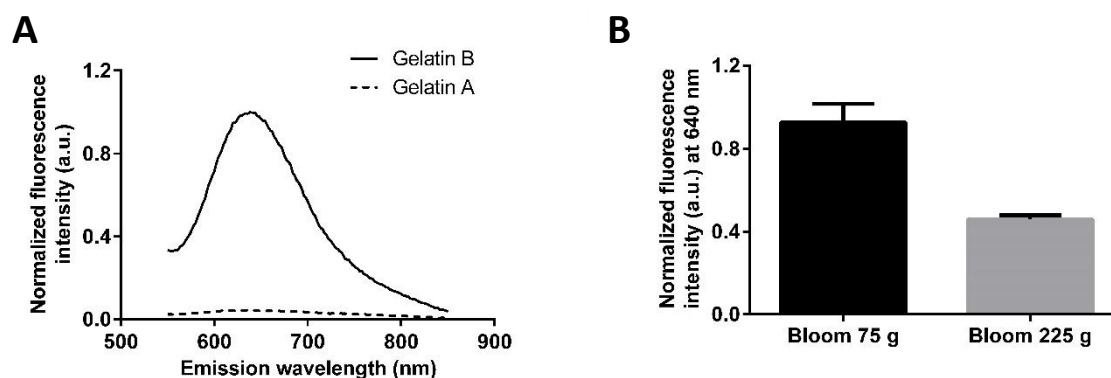


Figure S4. A) Emission spectra comparing the efficiency of gelatin A and B for the formation of AuNCs using 5 mM gold chloride, B) Fluorescence intensity at 640 nm resulted after interaction with gold using gelatin B of different bloom values (75 and 225 g).

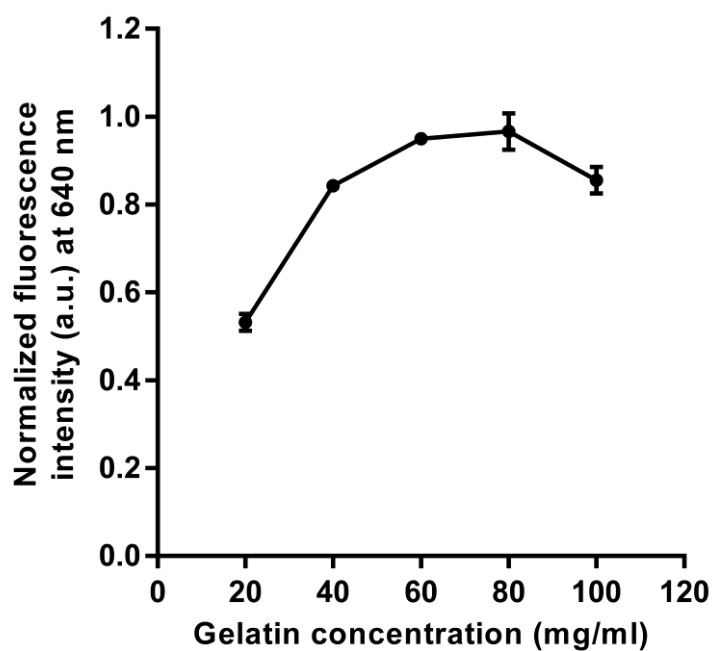


Figure S5. Effect of multiplication of gelatin concentration on the fluorescence intensity of AuNCs while keeping the Au: gelatin ratio constant.

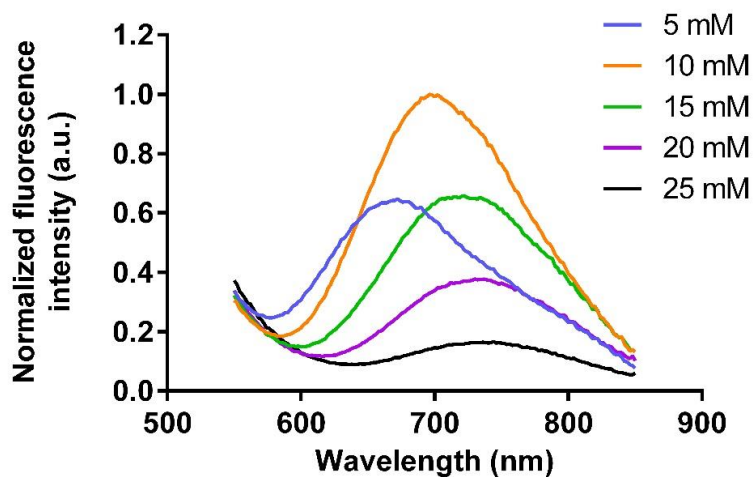


Figure S6. Effect of GSH concentration on the fluorescence spectra of gelatin-stabilized AuNCs.

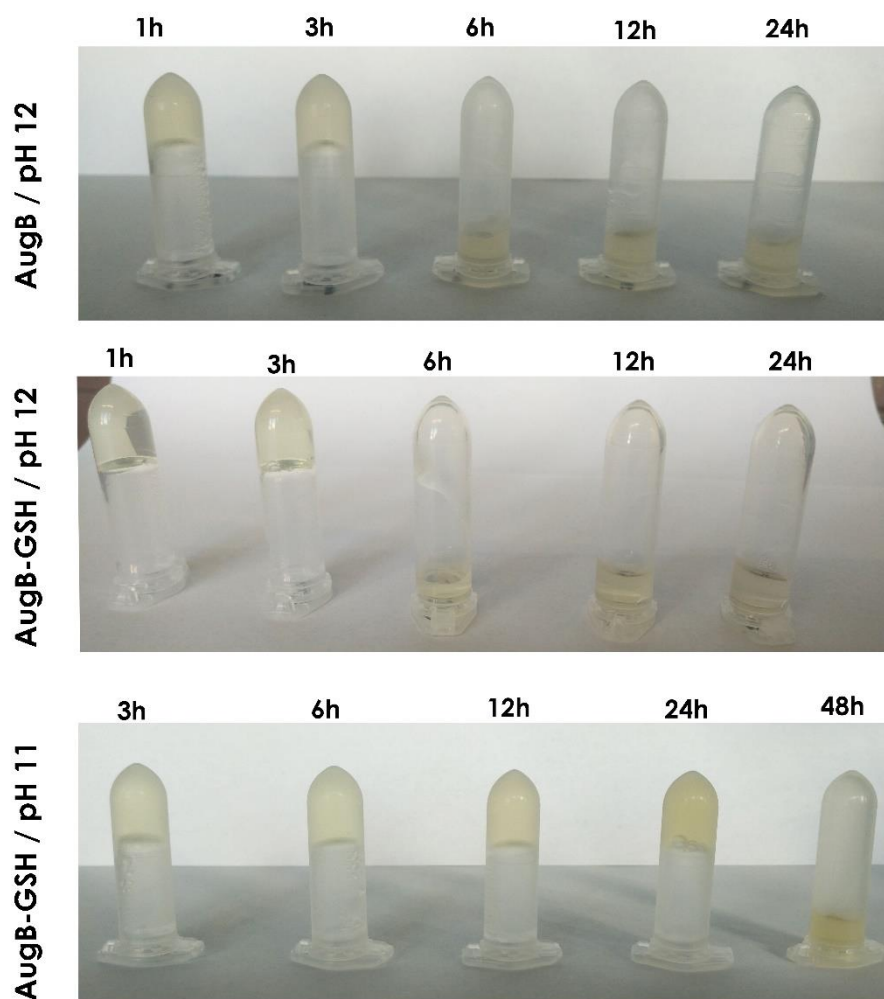


Figure S7. Effect of reaction pH and time on the gelling properties of AuNCs-modified gelatin upon cooling to 4°C.

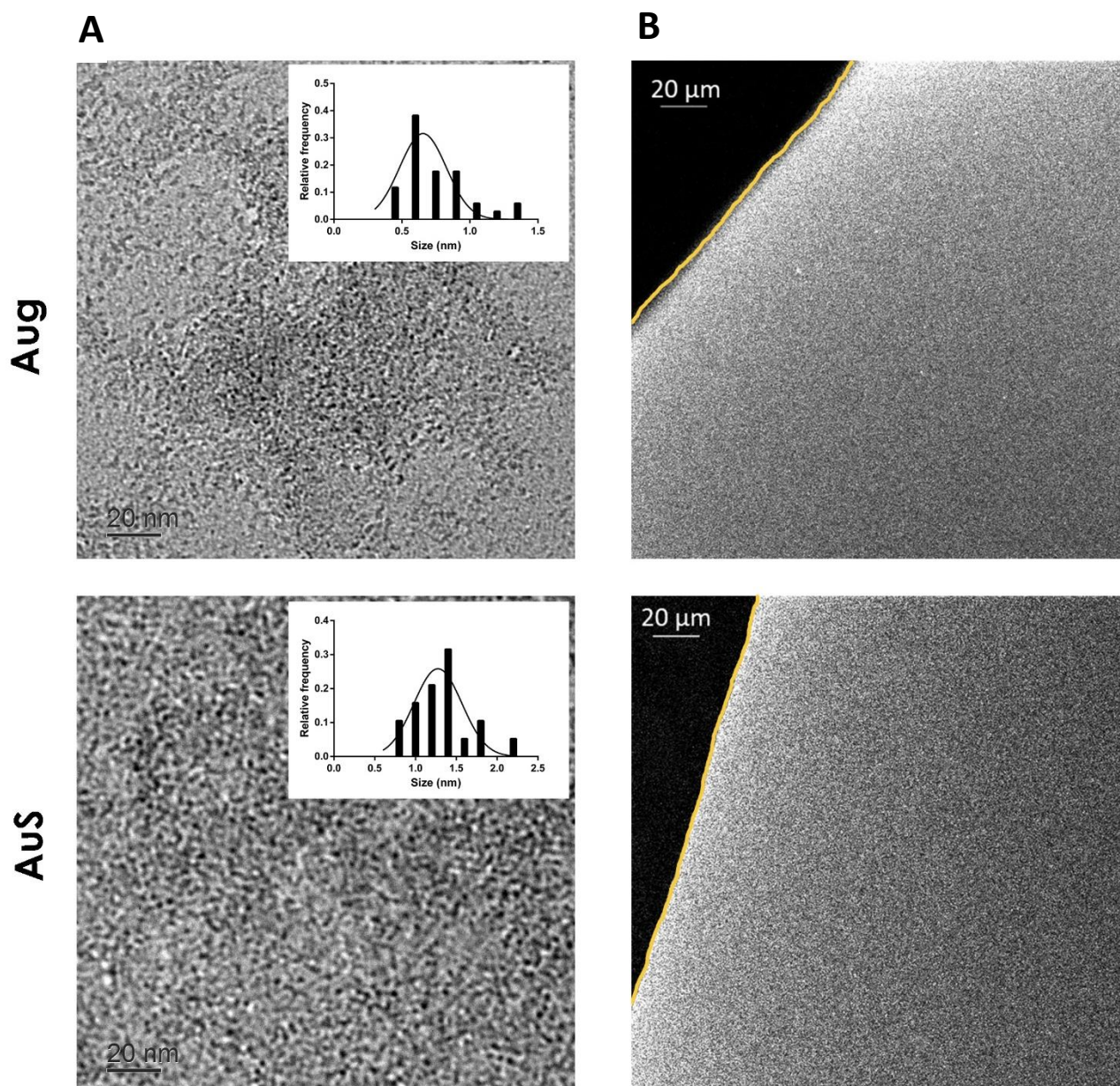


Figure S8. A) TEM images of Aug and AuS (10,000x magnification) with inserts showing the measured size distribution ($n=30$). Calculated average size is 0.74 ± 0.24 nm and 1.31 ± 0.35 nm for Aug and AuS, respectively and B) CLSM images upon excitation at 405 nm. The yellow line is drawn to show the droplet edge where the fluorescence can be detected to the right.

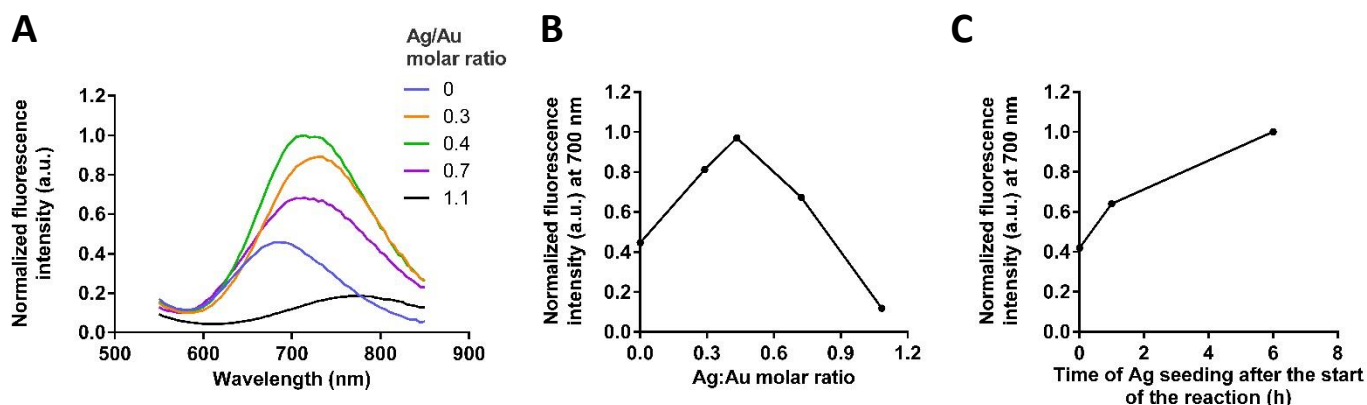


Figure S9. Formation of alloy AuAgNCs; A) Effect of Ag : Au ratio on the emission spectra while excitation at 368 nm, B) Effect of Ag : Au ratio on the fluorescence intensity at 700 nm, c) Effect of the lag time between the start of the reaction and doping Ag ions on the fluorescence intensity at 700 nm.

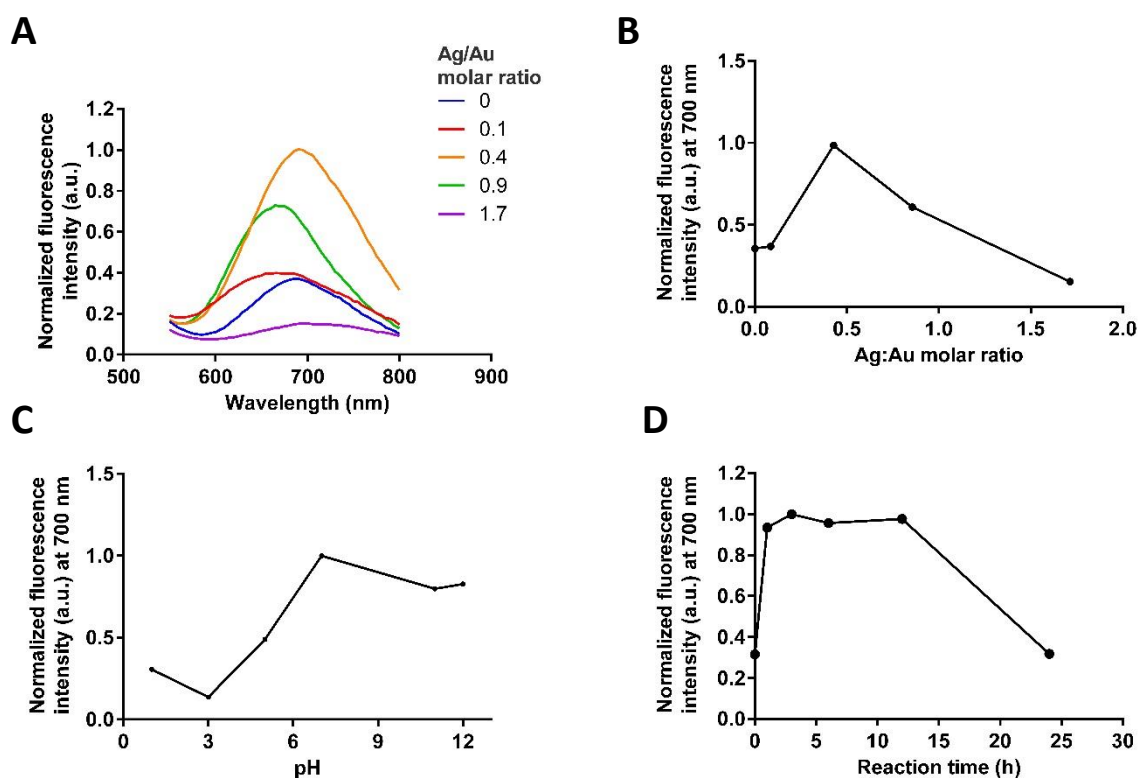


Figure S10. Effect of interactions with Ag ions after AuS formation; A) Effect of Ag: Au molar ratio on the emission spectra. B), C) and D) Effect of Ag: Au molar ratio, pH and reaction time on the fluorescence intensity at 700 nm, respectively.

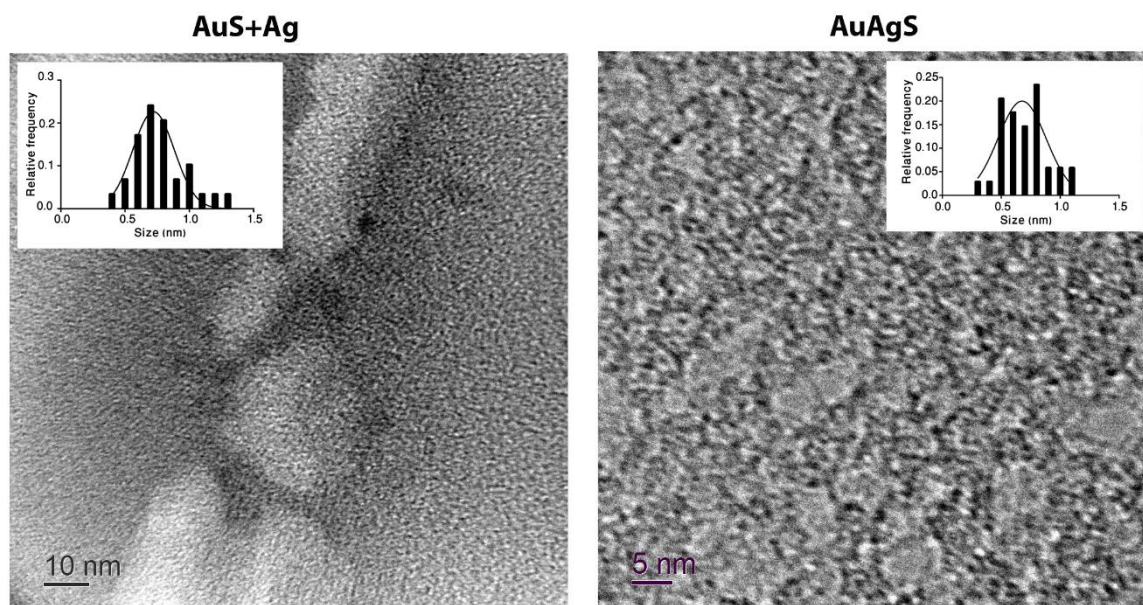


Figure S11. TEM images of AuS+Ag and AuAgS. The inserts show the measured size distribution ($n=30$). Calculated average size is 0.77 ± 0.21 nm and 0.69 ± 0.19 nm for AuS+Ag and AuAgS, respectively.

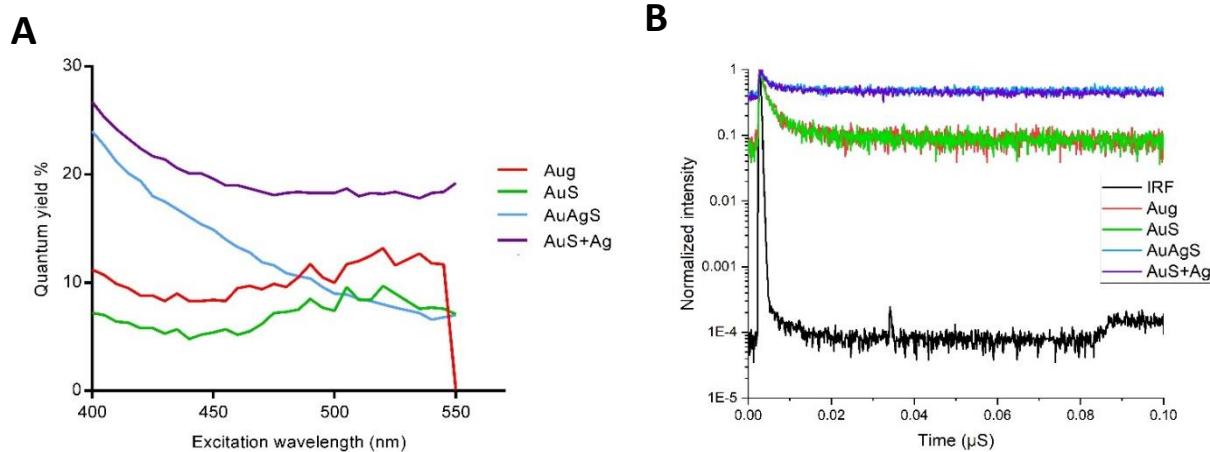


Figure S12. A) Absolute quantum yield of different AuNCs measured at emission range from 196 nm to 958 nm upon excitation with different wavelengths (400-550 nm), B) Normalized lifetime TCSPC measurements performed with a pulsed laser diode ($\lambda = 470$ nm) and a band pass filter (685/70).

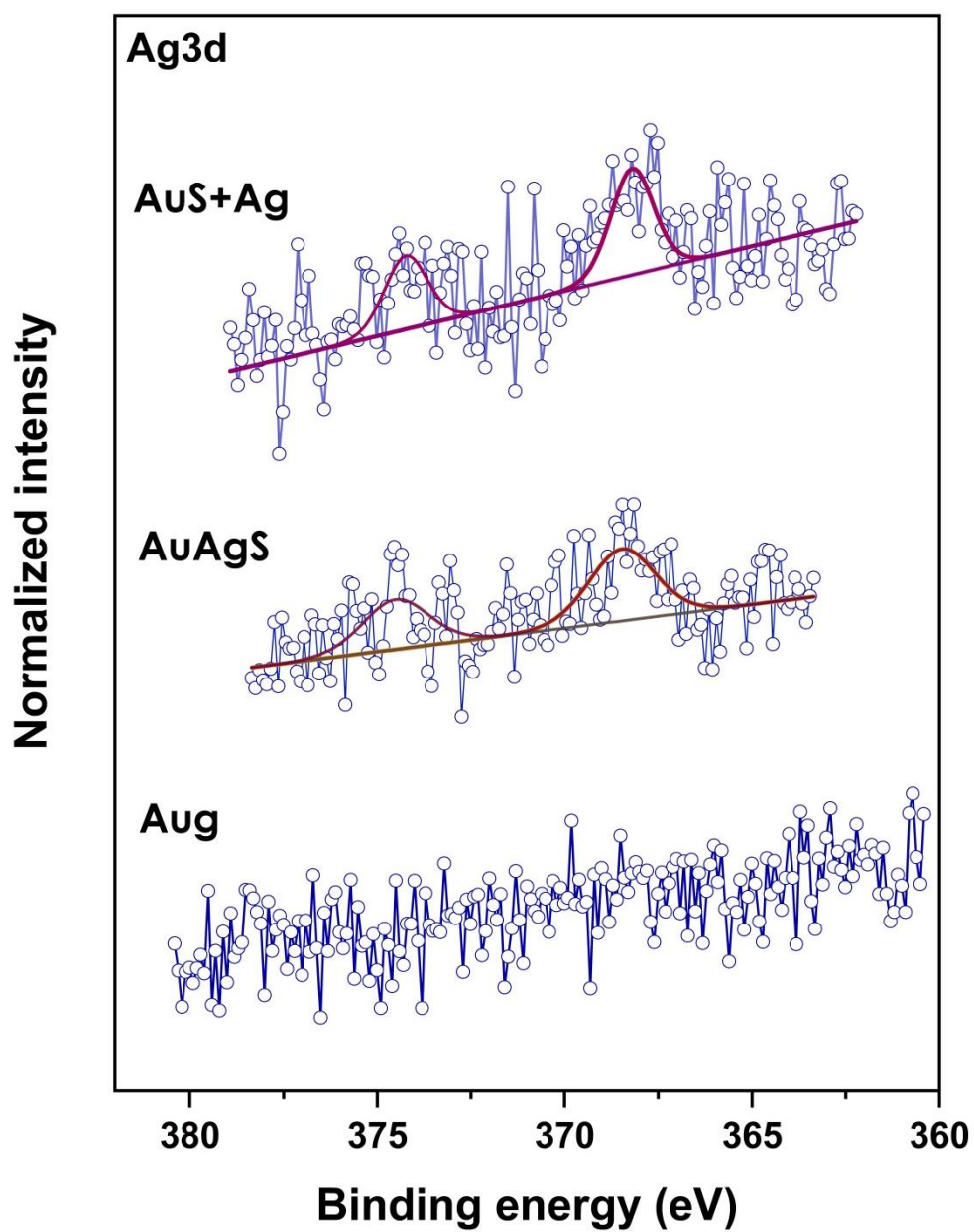


Figure S13. Ag3d_{5/2} of AuS+Ag, AuAgS and Aug (upper, middle and lower curve, respectively) indicating the detection of Ag in both of the Ag-modified AuNCs in comparison to Aug.

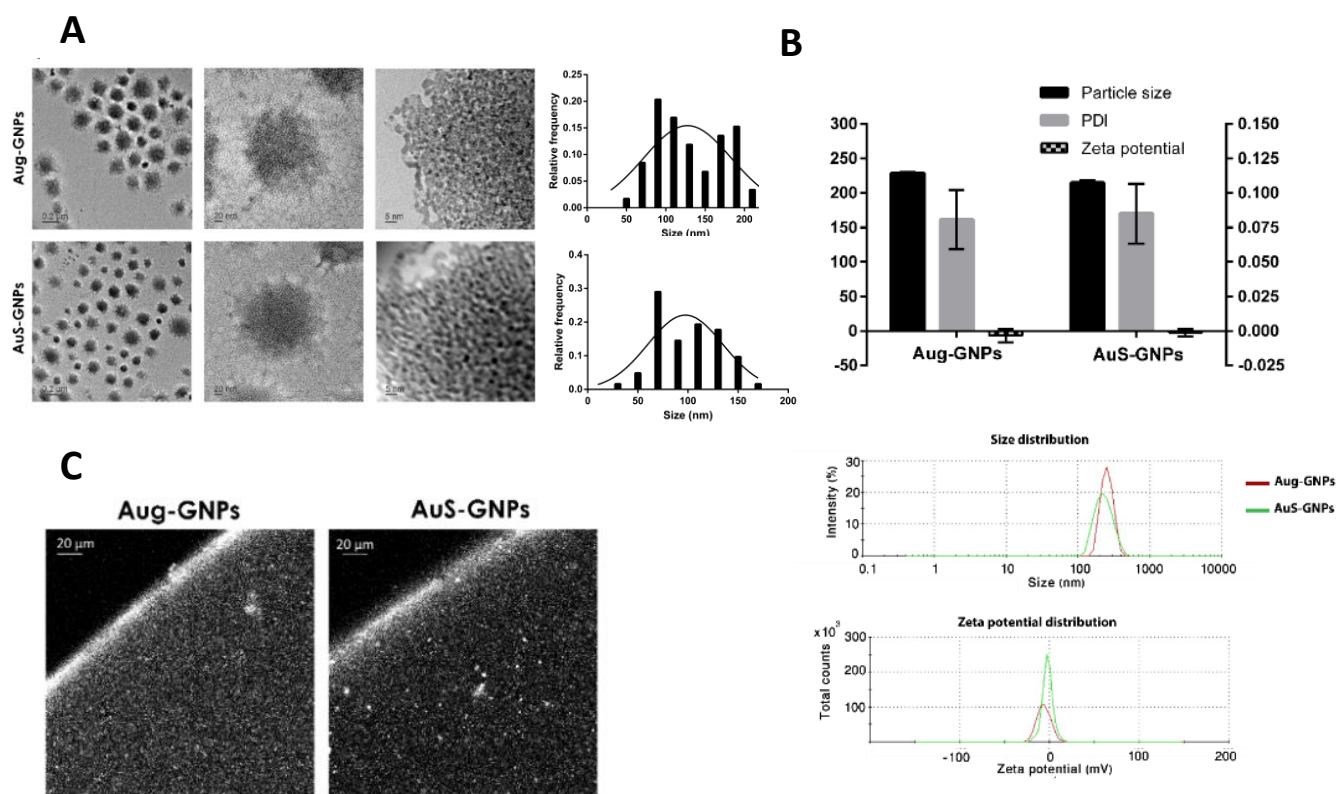


Figure S14. A) TEM images of Aug-GNPs and AuS-GNPs with different magnifications showing the inner distribution of AuNCs in addition to the size distribution as determined by the TEM images ($n=50$). Average size is 132.3 ± 43.6 and 99.4 ± 33.5 nm for Aug-GNPs and AuS-GNPs, respectively, B) Size (nm), zeta potential (mV) plotted on the left Y-axis and PDI plotted on the right Y-axis, accompanied with the size and zeta potential distribution as measured by DLS, C) CLSM images of Aug-GNPs and AuS-GNPs upon excitation at 405 nm.

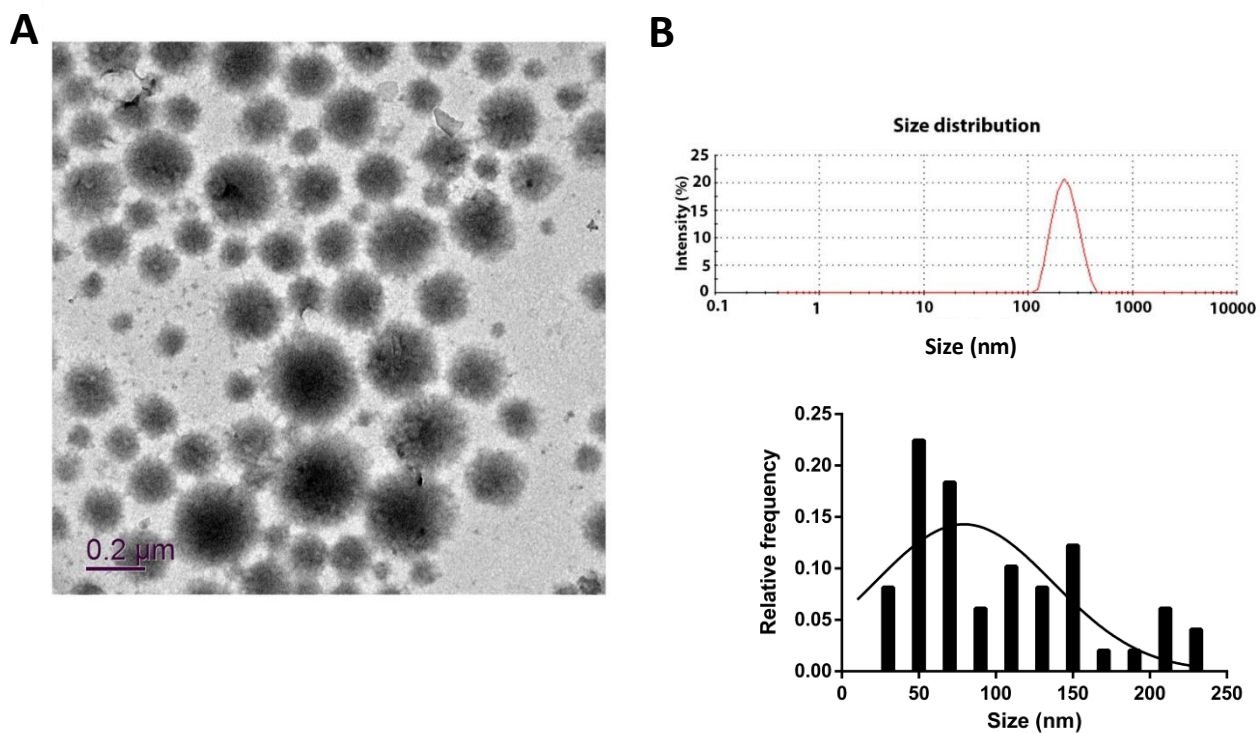


Figure S15. TEM images of AuAgS-GNPs, b) Size distribution as measured by DLS (upper panel, Z-average size of 218.8 ± 1.7 nm) and by TEM (lower panel, $n=50$, average size = 103.2 ± 62.2 nm).

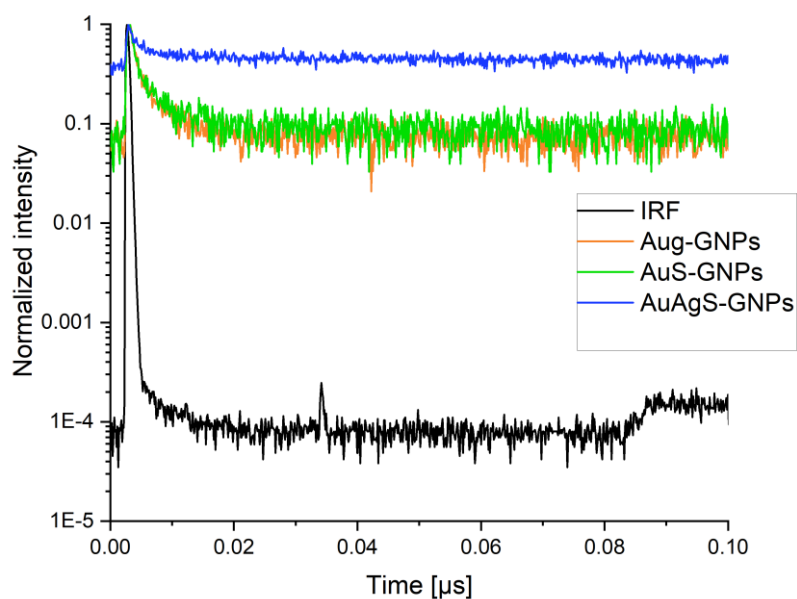


Figure S16. Normalized lifetime TCSPC measurements, at $\lambda_{\text{ex}} = 470$ nm using an emission band pass filter 685/70, of AuAgS-GNPs in comparison to AuS-GNPs and Aug-GNPs.

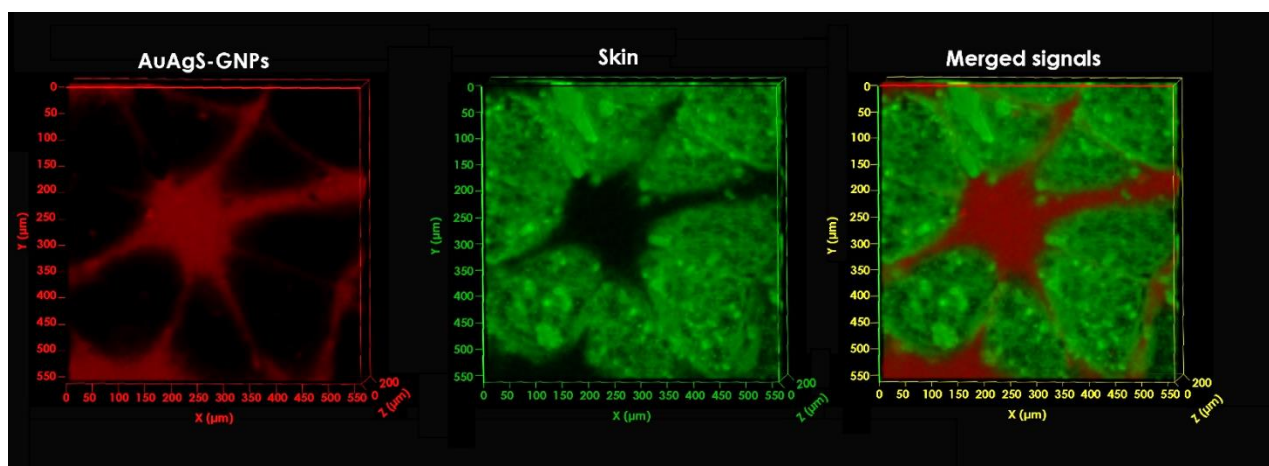


Figure S17. Confocal images of AuAgS-GNPs with skin upon excitation at 405 nm. The panels show the separated channels of NPs (red) and skin (green) in addition to the merged signals. Crude fluorescence was recorded and the signals of skin and NPs were separated using linear unmixing with references to their individual spectra recorded prior to the experiment.

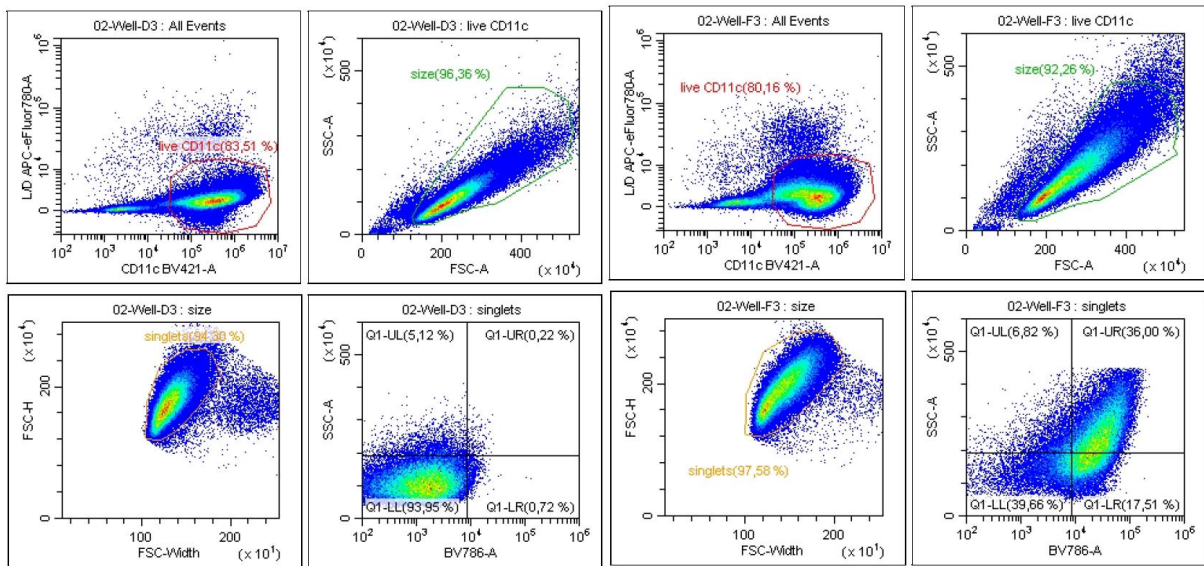


Figure S18. Gating strategy to determine uptake. After gating live CD11c⁺ cells, cells were further gated by size, and doublet were excluded on a FSC-W/FSC-H plot. Nanoparticle uptake was quantitated based on the increase in fluorescence intensity in the BV786 channel and an increase in SSC. The four plots on the left side show cells incubated with 40 μg/mL soluble OVA and the four plots on the right side cells that were incubated with 40 μg/mL dextran modified OVA nanoparticles.

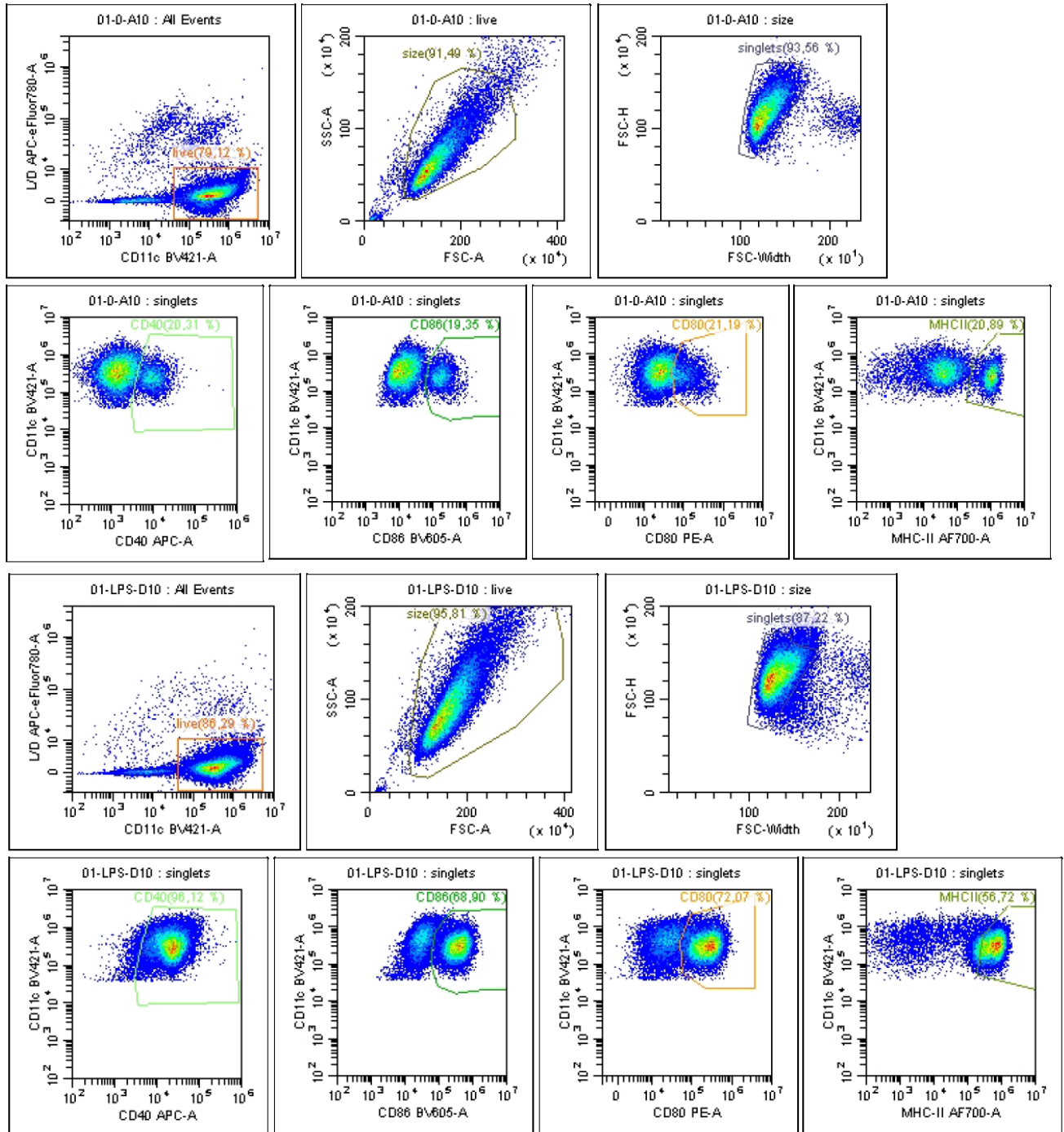


Figure S19. Gating strategy to determine BMDC activation. After gating live CD11c+ cells, cells were further gated by size, and doublet were excluded on a FSC-W/FSC-H plot. The gates for CD40, CD86, CD80, and MHC II positive cells were determined based on instimulated (two top rows) and LPS stimulated (two bottom rows) cells.

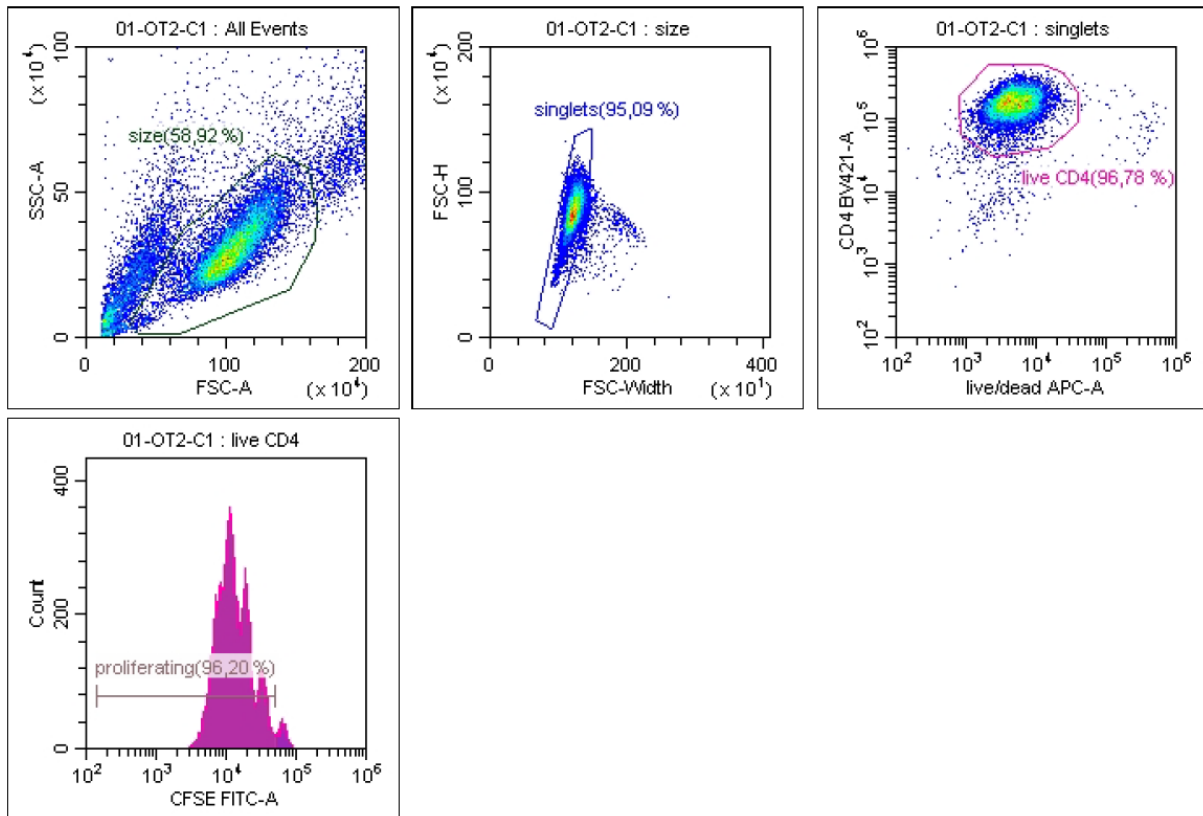


Figure S20. Gating strategy of OT-II cells. OT-II cells were first gated based on size/granularity, followed by exclusion of doubles on a FSH-H/FSC-W plot. Next live CD4+ cells were gated and proliferating cells were quantitated as CFSE^{low} cells.

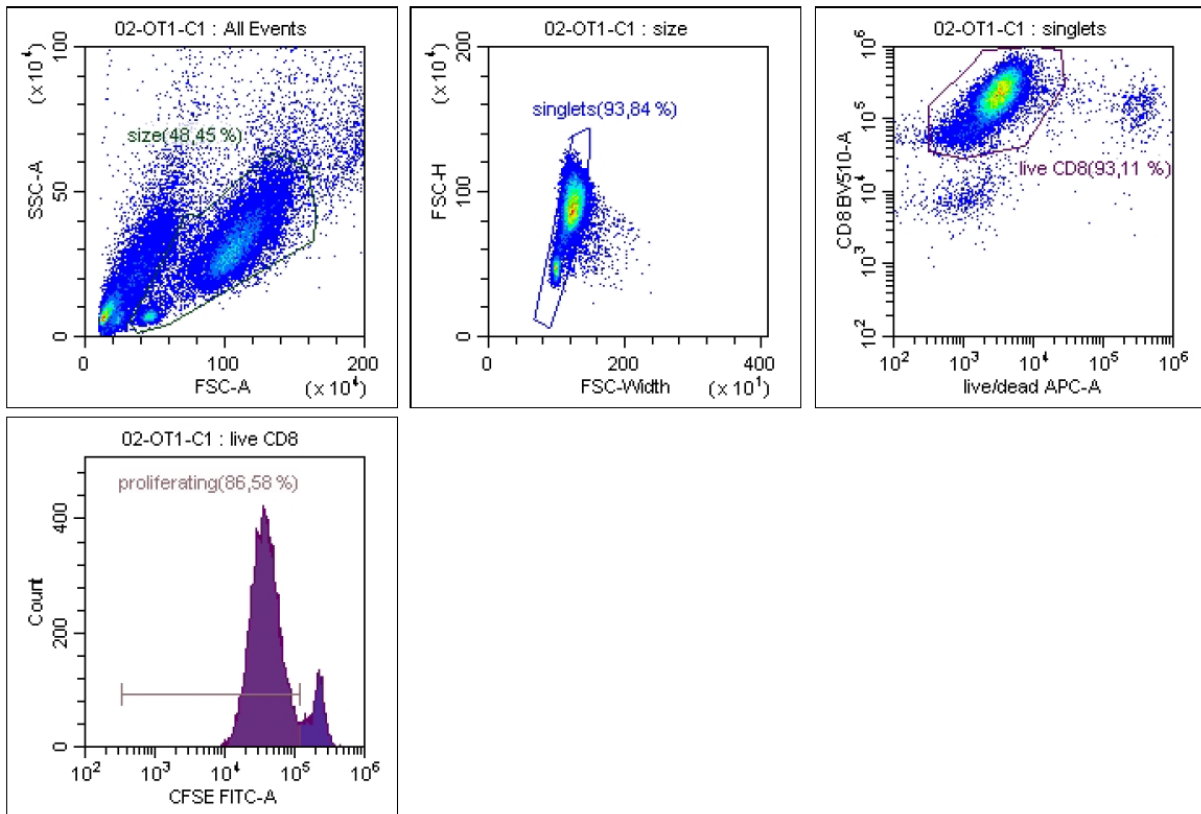


Figure S21. Gating strategy For OT-I cells. OT-I cells were first gated based on size/granularity, followed by exclusion of doubles on a FSH-H/FSC-W plot. Next live CD8+ cells were gated and proliferating cells were quantitated as CFSE^{low} cells.

Table S1. Different selected formulations of AuNCs synthesized using gelatin B (4% w/v) and gold chloride trihydrate (10 mM) at 60°C.

Gold nanoclusters	GSH concentration (mM)	Ag: Au molar ratio	pH	Reaction time
Au ₈	-	-	12	3h
AuS	10	-	11	24h
AuS+Ag	10	0.4	11 (to form AuNCs), then 7 (while adding Ag ⁺)	24h (before Ag ⁺ addition), then 3h (with added Ag ⁺)
AuAgS	10	0.4	11	6h (with no Ag ⁺), then 18h (with Ag ⁺ doping)

Abbreviations

APCs	Antigen presenting cells
AuNCs	Gold nanoclusters
BMDCs	Bone marrow-derived dendritic cells
CLSM	Confocal laser scanning microscopy
CTL	Cytotoxic T lymphocytes
DAPI	4',6-diamidino-2-phenylindole
Dex-NPs	Dextran-functionalized gelatin nanoparticles loaded with ovalbumin
DLP	Digital Light Processing
DMEM	Dulbecco's Modified Eagle's Medium
DPBS	Dulbecco's phosphate-buffered saline
EDC	N-(3-dimethylaminopropyl)-N'-ethylcarbodiimide hydrochloride
EE	Entrapment efficiency
FT-IR	Fourier transform infrared spectrometry
GNPs	Gelatin nanoparticles
HaCat	Human keratinocytes cell line
HBSS	Hank's Balanced Salt Solution buffer
LC	Loading capacity
MALDI-TOF MS	Matrix-assisted laser desorption/ionization time of flight mass spectroscopy
MHC	Major histocompatibility molecules
MNs	Microneedles
MTT	3-(4,5-Dimethyl-2-thiazolyl)-2,5-diphenyl-2H-tetrazolium bromide
NCs	Nanoclusters
NHS	N-Hydroxysuccinimide
NPs	Nanoparticles
OD	Optical density
OVA	Ovalbumin
PDMS	polydimethylsiloxane
P-NPs	Plain gelatin nanoparticles
PVA	Poly (vinyl alcohol)
QY	Quantum yield
S-NPs	Gelatin nanoparticles lo
TEM	Transmission electron microscopy
XPS	X-Ray Photoelectron Spectroscopy

Curriculum Vitae

Name: Nesma Elsayed Ahmed Ahmed Ibrahim

Birth date and place: 19.03.1985, Alexandria, Egypt

Nationality: Egyptian

Email: nesma.ibrahim@uni-saarland.de, nesma.ahmed@alex.edu.eg,
nes.elsayed@gmail.com

Education

- **April 2015 – present:** PhD student, Department of Biopharmaceutics and Pharmaceutical Technology, Saarland University, Germany.
- **March 2013 – April 2015:** PhD student, Department of Pharmaceutics, Faculty of Pharmacy, Alexandria University, Egypt.
- **January 2013:** M.Sc. in Pharmaceutical Sciences "Pharmaceutics", Department of Pharmaceutics, Faculty of Pharmacy, Alexandria University, Egypt.
- **June 2007:** B.Sc. in Pharmaceutical Sciences, Faculty of Pharmacy, Alexandria University, Egypt. (Distinction honour – ranked the 4th among class).

Academic career

- **October 2015 – present:** Teaching assistant, Department of Biopharmaceutics and Pharmaceutical Technology, Saarland University, Germany.
- **February 2013 – April 2015:** Assistant Lecturer, Department of Pharmaceutics, Faculty of Pharmacy, Alexandria University, Egypt.
- **December 2007 – February 2013:** Demonstrator, Department of Pharmaceutics, Faculty of Pharmacy, Alexandria University, Egypt.

Publications

Book chapter

1. **N. El-Sayed**, L. El-Khourdagui and M. Schneider, "Insights into interactions of gold nanoparticles with the skin and potential dermatological applications",

Nanoscience in Dermatology, 1st Edition, August 2016.

Research articles

2. **N. El-Sayed**, V. Trouillet, A. Clasen, G. Jung, K. Hollemeyer and M. Schneider, "NIR-emitting gold nanoclusters-modified gelatin nanoparticles as a bioimaging agent in tissue", *Advanced Healthcare Materials*, 8(24), 2019,1900993.
3. T. Angelo, **N. El-Sayed**, M. Jurisic, A. Koenneke, G. Gelfuso, M. Cunha-Filho, S. Taveira, R. Lemor, M. Schneider, and T. Gratieri " Effect of physical stimuli on hair follicle deposition of clobetasol-loaded Lipid Nanocarriers ", *Scientific Reports*,10(1), 2020,176.
4. L. El-Khordagui, **N. El-Sayed**, S. Galal, H. El-Gowell, H. Omar and M. Mohamed "Photosensitizer-eluting nanofibers for enhanced photodynamic therapy of wounds: A preclinical study in immunocompromized rats", *International Journal of Pharmaceutics*, 520 (1–2), 2017, 139–148.
5. **N. El-Sayed**, S. Galal, H. El-Gowell and L. El-Khordagui, "Inhibition of postsurgical adhesions by methylene blue-loaded nanofibers versus cast film matrices", *Journal of Biomaterials Science, Polymer Edition* , 27 (10), 2016, 1029-1044.

Articles in progress

6. **N. El-Sayed**, L. Vaut and M. Schneider "Customized fast-dissolving microneedles prepared with the aid of 3D printing for nanoparticles delivery", in due publication
7. **N. El-Sayed**, E. Korotchenko, R. Weiss and M. Schneider "Functionalized theranostic nanovaccine for dendritic cells targeting and modulation of immune response", in due publication

Conferences contributions

Oral presentations

1. **N. El-Sayed** and M. Schneider, "Gold nanoclusters-modified gelatin nanoparticles as novel theranostics for combined vaccination and bioimaging ", The 6th Galenus Workshop 2018 (Development & Translation of Bioresponsive Drug Delivery Systems and Medical Devices), Wuerzburg, Germany, November 2018.

2. V. Chiaula, **N. El-Sayed**, A. Melero, "Bioinspired mucoadhesion technology", pitch presentation, PhD summer school: Drug Delivery - using nano and micro technologies in Technical University of Denmark (DTU), Lyngby, Denmark, August 2017.
3. **N. El-Sayed**, S. Galal, H. El-Gowell and L. El-Khordagui, "Methylene blue-loaded polyhydroxybutyrate membranes for reduction of post-surgery peritoneal adhesions", DUPHAT. Dubai, United Arab Emirates, March 2013.

Poster presentations

4. **N. El-Sayed** and M. Schneider "Functionalized theranostic gelatin nanoparticles for antigen delivery", Controlled Release Society Annual Meeting & Exposition, Valencia, Spain, July 2019.
5. **N. El-Sayed** and M. Schneider, "Protein-based nanoparticles as a potential system for antigen delivery", PhD day of Faculty of Science and Technology, Saarland University, Saarbruecken, Germany, November 2018.
6. **N. El-Sayed** and M. Schneider, "Development of theranostic gelatin nanoparticles for the delivery of ovalbumin as a model antigen". The 12th International Conference and Workshop on Biological Barriers (BioBarriers 2018), Saarbruecken, Germany, August 2018.
7. **N. El-Sayed**, V. Trouillet and M. Schneider, "Gold nanoclusters-labelled gelatin nanoparticles as a novel bioimaging approach in tissue", Controlled release society, German Chapter, 22nd annual meeting (Local Controlled Delivery...and more!), Halle, Germany, March 2018.
8. **N. El-Sayed**, L. El-Khourdagui and M. Schneider, " Development and optimization of novel NIR- emitting gold nanoclusters-loaded gelatin nanoparticles ", Annual Meeting of the German Pharmaceutical Society (Novel Therapies for Future Challenges), Saarbruecken, Germany, September 2017.
9. V. Chiaula, **N. El-Sayed**, A. Melero, "Fabrication and characterization of bioadhesive structures for oral drug delivery", PhD summer school: Drug Delivery - using nano and micro technologies in Technical University of Denmark (DTU), Lyngby, Denmark, August 2017.
10. **N. El-Sayed** and M. Schneider, "Development of a novel nanoparticulate system

for imaging in tissues and drug delivery ", PhD summer school: Drug Delivery - using nano and micro technologies in Technical University of Denmark (DTU), Lyngby, Denmark, August 2017.

11. **N. El-Sayed**, S. Galal, H. El-Gowell, H. Omar and L. El-Khordagui, "Methylene blue-nanofibers for photodynamic therapy of infected wounds in immunocompromized rats", BioVision, Alexandria, Egypt, April 2014.
12. **N. El-Sayed**, S. Galal, H. Omar, M. Mohamed and L. El-Khordagui, "Methylene blue-eluting nanofibers as a potential biomaterial for antimicrobial photodynamic therapy (APDT)", The 14th Arab International Conference of Materials Science "Materials for Biomedical Applications". Alexandria, Egypt, December 2013.
13. **N. El-Sayed**, S. Galal, H. El-Gowell, H. Omar and L. El-Khordagui, "Wound healing properties of methylene blue-eluting nanofibers in an immunocompromized rat model", The 14th Arab International Conference of Materials Science "Materials for Biomedical Applications". Alexandria, Egypt, December 2013.
14. **N. El-Sayed**, S. Galal, H. El-Gowell and L. El-Khordagui, "Methylene blue-loaded polyhydroxybutyrate membranes for reduction of post- surgery peritoneal adhesions", Proceedings of DUPHAT. Dubai, United Arab Emirates March 2013.
15. **N. El-Sayed**, S. Galal, H. Omar and L. El-Khordagui, "Novel photoactive antimicrobial nanofibers for biomedical applications", the FIP Centennial Congress. Amsterdam, the Netherlands, October 2012.

Thesis supervision

April – October 2018 : "Development of composite nanoparticles for dermatitis treatment", Master thesis by Madona Doos, Department of Biopharmaceutics and Pharmaceutical Technology, Saarland University, Germany.

Teaching experience

- **October 2015 – present**: Undergraduate laboratory teaching at the Department of Biopharmaceutics and Pharmaceutical Technology, Saarland University, Germany.
 - Nanocarriers, Semisolids, Quality assurance seminars and Pharmacokinetics

- **September 2007 – January 2015:** Undergraduate laboratory teaching at the Department of Pharmaceutics, Faculty of Pharmacy, Alexandria University, Egypt.
 - Semisolid and solid dosage forms, micromeritics, physical pharmacy, complexation, incompatibilities, solubilization techniques, drug release, pharmaceutical compounding.
 - Community pharmacy practice and OTC drugs.

Awards and honors

- **April 2015:** PhD scholarship provided for two years by the Cultural Affairs and Missions Sector, Egyptian Ministry of High Education and Research (MOHE-CASM).
- **March 2013:** Travel grant to attend the Dubai International Pharmaceuticals and Technologies Conference and Exhibition (DUPHAT) in Dubai, United Arab Emirates.
- **November 2007:**
 - Egyptian Pharmacist Syndicate Award for Academic Distinction, Cairo, Egypt.
 - Alexandria Syndicate of Pharmacists Award for Academic Distinction, Alexandria, Egypt.
- **October 2007:** Alexandria University Award for Academic Distinction, Egypt.

Acknowledgments

First and Foremost praise is to ALLAH, the Almighty, for the infinite blessings and for giving me the strength throughout the journey.

This work has been achieved by the support of many different people, to whom I would like to express my gratitude.

I would like to thank **Prof. Dr. Marc Schneider** 'mein Doktoter' and express my gratitude to him for giving me the opportunity to join his group and for his support through all these years. Thanks for the fruitful discussions that I have learnt a lot from. I really appreciate your valuable scientific guidance, while giving me the freedom to build my scientific character. I am really thankful for the good times and the friendly atmosphere you have created around.

I would like to thank **Prof. Dr. Thorsten Lehr** for his contribution in the thesis supervision process.

I would like to thank **Prof. Dr. Labiba El-Khoradgui** (Alexandria University, Egypt) for her contribution in supervising the thesis for the first two years. Thank you for your support to start my research work here in Germany.

I would like to thank the Cultural Affairs and Missions Sector, Egyptian Ministry of High Education and Research (**MOHE-CASM**) for their financial support for the first two years of the research and their guidance through the cultural office in Berlin that facilitated my stay in Germany.

I would like to thank all my collaborators from different institutes for their sincere work to make this research successful. I would like to thanks to **Vanessa Trouillet** for sharing

her valuable experience with X-ray photoelectron spectroscopy analysis. I would like to thank **Prof. Dr. Gregor Jung** and his PhD student **Anne Clasen** for their scientific input to the 3D fluorescence and lifetime measurements and **Dr. Klaus Hollemeyer** for his help with MALDI-TOF MS analysis. I would like to thank **Lukas Vaut** for his creative work on the design and 3D printing of the microneedles master molds. I would like to thank **Prof. Dr. Richard Weiss** and his PhD student **Evgeniia Korotchenko** for their valuable scientific contribution for the immunological evaluation of the developed systems.

I would like to thank my colleagues in Schneider group for all the support and the friendly atmosphere you provided through all these years: **Agnes, Afra, Alexandra, Aljoscha, Baseer, Carolin, Enkeleda, Johannes, Karola, Marcel, Nashi, Tamara, Thorben** and **Tom**. I would like to thank **Marijas** for his continuous support in the lab, his patient training in cell culture and for always being friendly. Thanks to **Isabelle** and **Peter** for always facilitating the work.

Thanks to my friend **Salma**, whom I shared with happy times and found supportive in hard times. Thank you and **Shery** for being my small family here.

All my sincere love goes to my family, my **Mom** and my **Dad** who supported and encouraged me to be the person I am today. Your love is always my strength. Making you proud is my real motivation. Thanks for having faith in me. May Allah bless you always and reward you for being good to us. **Mohamed**, my beloved brother, thank you for always being beside me. Listening and understanding is the best gift you always give to me. Thank you for all the good times in Egypt, Germany and Austria. Thanks to **Nour**, you are not a friend you are a family. You have been always my support. Thank you for always being there for me.

Thanks! .. Nesma